COMPUTATIONAL AND EXPERIMENTAL STUDIES OF ATOMIC FORCE MICROSCOPY ON VISCOELASTIC POLYMERS WITH SURFACE FORCES

by

Bahram Rajabifar

A Dissertation

Submitted to the Faculty of Purdue University

In Partial Fulfillment of the Requirements for the degree of

Doctor of Philosophy

School of Mechanical Engineering

West Lafayette, Indiana

May 2021

THE PURDUE UNIVERSITY GRADUATE SCHOOL
STATEMENT OF COMMITTEE APPROVAL

Dr. Arvind Raman, Chair
School of Mechanical Engineering

Dr. Anil Bajaj
School of Mechanical Engineering

Dr. Chelsea Davis
Material Engineering Department

Dr. Ron Reifenberger
Department of Physics

Approved by:
Dr. Nicole L. Key

To my dear parents, lovely wife, and adorable kids

ACKNOWLEDGMENTS

First, I would like to acknowledge the valuable support of my advisor, Arvind Raman, who introduced and taught me the broadness and depth of science behind using atomic force microscopy. I do appreciate his enthusiasm, efficient discussions, and trust and I know without his priceless support; this study could not be carried out and completed. Also, I would like to deeply thank the committee members (Ron Reifenberger, Anil Bajaj, and Chelsea Davis), collaborators: (Greg Meyers, Daniel Kirakofe, and Roger Proksch), and lab mates: (Ryan Wagner, Yuri Efremov, Maria J. Cadena, Randi Potekin, Devin Kalafut, and Dan Feng) for their supports, comments, and helps. Last but not the least, I am grateful to my lovely wife and adorable kids who patiently accepted my busyness and lack of time during my Ph.D. and their continual support, encouragement, and understanding during my study. The author is grateful for financial support for this research provided by the National Science Foundation through Grant CMMI-1726274 GOALI.

TABLE OF CONTENTS

LIST OF TABLES 7
LIST OF FIGURES 9
ABSTRACT 15
1. INTRODUCTION 17
1.1 Atomic force microscopy 17
1.2 Mathematical models of tip-sample interaction forces 22
1.3 Overview of the work 27
2. TAPPING MODE ON VISCOELASTIC POLYMER SAMPLES WITH SURFACE FORCES 30
2.1 Introduction 30
2.2 Theory of the proposed approach 31
2.3 Verification 38
2.4 Computational results 40
2.5 Experiments 46
2.6 Conclusions 52
3. DISCRIMINATION OF ADHESION AND VISCOELASTICITY FROM NANOSCALE MAPS OF POLYMER SURFACES USING BIMODAL ATOMIC FORCE MICROSCOPY .. 54
3.1 Introduction 54
3.2 Theory 58
3.3 Verification of the amplitude reduction algorithm 65
3.4 Computational results 67
3.5 Material viscoelasticity and adhesive properties estimation 71
3.6 Experiments 72
3.7 Conclusions 75
4. A FAST FIRST-PRINCIPLES APPROACH TO MODEL ATOMIC FORCE MICROSCOPY ON ADHESIVE VISCOELASTIC SURFACES 77
4.1 Introduction 77
4.2 Methods 78
4.3 Attard's original computational model: 81

4.4 Improved computational framework: 82
4.5 Computational Stability 84
4.6 EAM Verification 86
4.7 EAM performance 87
4.8 AFM Simulations using EAM 92
4.9 Conclusion 97
5. MECHANICAL PROPERTIES CHARACTERIZATION OF SOFT POLYMERS WITH SURFACE FORCES USING PEAKFORCE TAPPING AFM – A MACHINE-LEARNING APPROACH 98
5.1 Introduction 98
5.2 Theory 101
5.3 Validation of the proposed algorithm 105
5.4 Computational results 106
5.5 Regression-based machine-learned predictive models 112
5.6 Conclusions 117
6. CONCLUSIONS AND FUTURE WORK 118
6.1 Contributions of This Thesis 118
6.2 Future Research Directions 119
REFERENCES 121

LIST OF TABLES

Table 1. A comparison between well-known continuum mechanics contact models in terms of their ability to include surface forces, viscoelasticity, and surface dynamics. These are important parameters which are needed to be accounted for when working with soft, adhesive, and viscoelastic polymers. 23

Table 2. The parameter values used for the simulations in verification and computational results sections. 40

Table 3. The material property estimations/extracted from the set of experiments with $A^{free} = 35.9\,nm$ and used for subsequent validation with another set of experiments with $A^{free} = 18\,nm$ on the three blend polymer sample. 52

Table 4. Three observables of the most common modalities of bimodal AFM Observable. 56

Table 5. The surface properties used to predict the dependence of bimodal observables on local adhesive and viscoelastic polymer properties using the proposed algorithm. 67

Table 6. The coefficients of the conversion matrix and vector as described in Eqn. (46) determined through linear regression on simulation results. The tip radius estimate is 8.7 nm. 74

Table 7. Predicted mean viscoelastic properties for the polymer domains based on the acquired bimodal AFM data. The predictions agree with the ones in the literature *[114, 121, 132]*..... 74

Table 8. The employed values for LJ pressure and surface viscoelasticity properties for LDPE in the conducted simulations. H, z_0, ν, E_0, E_∞, and τ are Hamaker constant, equilibrium distance, Poisson's ratio, short-term modulus, Long-term modulus, and creep time, respectively. The tip radius in these simulations is set to be 10 nm. 86

Table 9. The convergence rate of these EAM implementation setups is evaluated to realize the optimized configuration. 88

Table 10. The employed values for LJ pressure and surface viscoelasticity properties for polystyrene (PS) in the conducted simulations. The tip radius in these simulations is set to be 50 nm. 94

Table 11. Operational and material characterization used in simulations for visualizing the cantilever-sample interaction in PFT mode of operation and parametric study. The colored cells are the parameters whose effect on the predicted F-d curves are studied and the employed range for each is mentioned in the legends of each of the sub-figures in Figure 43 with the same label. 107

Table 12. The ranges for Z and other material/ microcantilever parameters for the training set simulations. These ranges are defined based on the expected properties for elastomer samples and Bruker RTESPA-150-30 probes. The input parameters for the training set simulation are randomly selected over these defined ranges using the Latin hypercube sampling (LHS) method [120].. 115

Table 13. the evaluation results for the ML models' predictive accuracy. The employed test percentage used in these evaluations is 20%. 115

LIST OF FIGURES

Figure 1. Schematic of AFM microcantilever and associated distance parameters with the surface. Z(t) is the distance between the undeflected tip and the undeformed surface, q(t) is the deflection of the cantilever, and d(t) is the separation between the deflected tip and undeformed surface. as obvious: $d(t) = Z(t) + q(t)$ 19

Figure 2. Force-time and force-separation curves for a typical PFT experiment. The relevant parameters are noted in the pictures..... 21

Figure 3. $F - d$ history during a single taping cycle predicted by the AMAC tool in VEDA [77] using the Hertz model including Kelvin-Voigt viscoelasticity in an *ad hoc* manner. The computational input parameters are as follows: free amplitude: 60 nm; natural and driving frequency: 75 kHz; Q = 150; approach velocity: 200 nm/s; tip radius: 10 nm. The viscoelastic surface is characterized by E = 1 GPa and η = 500 Pa·s. Note that the retraction phase features a region of attractive forces shaded in brown which is an artifact of underlying model assumptions. 25

Figure 4. A schematic of an oscillating tip with tip-sample dissipative and conservative forces. $d\,(\mathrm{nm})$ is the tip-sample gap and $Z\,(\mathrm{nm})$ is the distance between the unperturbed microcantilever tip and the sample. The average of interaction force history during approach and retraction is the conservative part of interaction since it depends on the instantaneous tip-sample gap d and contributes to the Virial, while the difference of the approach and retraction force history during a cycle is the non-conservative part of the interaction and contributes to the energy dissipation... 33

Figure 5. The proposed algorithm for predicting instrument observables by embedding Attard's model into the AM- AFM amplitude reduction formula. 35

Figure 6. Attard's viscoelastic model assumes an axisymmetric rigid tip interacting with a flat polymer surface. In order to model the viscoelasticity of the sample, creep compliance of a standard three-element viscoelastic model is utilized (Eq. (10)) [92] in conjunction with arbitrary surface force models. (a) and (b) show the un-deformed and deformed sample, respectively..... 37

Figure 7. Attard's viscoelastic model results [78], Ting's analytical viscoelastic model [77], and the code developed in the present work are compared with a prescribed triangular motion time profile of a rigid spherical tip. The triangular drive velocities are (a): $\pm 5\ \mu\mathrm{m/s}$, (b): $\pm 2\ \mu\mathrm{m/s}$, and (c): $\pm 1\ \mu\mathrm{m/s}$. Tip radius is $10\ \mu\mathrm{m}$ and the other material parameters used are identical to the ones used by Attard to facilitate comparison [78]. 39

Figure 8. A comparison between the dynamic approach curves results predicted by using the present algorithm (Figure 5) and the ones from the AMAC tool which includes explicit microcantilever dynamics for elastomer (upper row), and polycarbonate (lower row). The blue circles are from the proposed algorithm and the red solid lines are the VEDA-AMAC tool's outputs. The used material property data for these simulations are listed in Table 2. The equivalent microcantilever properties are: $K = 28\ \mathrm{N/m}$ and $Q = 542$, and the oscillation period is $3\times10^{-6}\ \mathrm{s}$. 40

Figure 9. The interaction between a rigid axisymmetric tip and the elastomer sample surface is computed using the approach of the present work. The viscoelasticity of the elastomer is modeled by using a standard linear solid (SLS) model with the data provided in Table 2. The tip travels through a sinusoidal wave with $100\ \text{kHz}$ frequency and $Z = 45\ \text{nm}$. The oscillation amplitude is $50\ \text{nm}$ and tip radius $= 100\ \text{nm}$. In (a) the $F-d$ and the $F-\dot{d}$ history (inset) are graphed. In (b), the deformation history during a sequence of time instants labeled 1-12 is graphed. 42

Figure 10. (a) Energy dissipation (E_{ts}) and (b) Virial (V_{ts}) vs. setpoint ratio (A^{ratio}) for a set of relaxation time (τ) values: 1: $2.9\ \mu\text{s}$, 2: $1.1\ \mu\text{s}$, 3: $0.40\ \mu\text{s}$, 4: $0.15\ \mu\text{s}$, 5: $54.7\ \text{ns}$, 6: $20.3\ \text{ns}$, 7: $7.6\ \text{ns}$, and 8: $2.8\ \text{ns}$. The Lennard-Jones parameters for all simulations are: $H = 8\times10^{-20}\ \text{J}$, and $Z_0 = 0.6\ \text{nm}$, and additional material properties are provided in Table 2 for the elastomer. The oscillation period is $3\times10^{-6}\ \text{s}$, the equivalent microcantilever properties are: $K = 28\ \text{N/m}$ and $Q = 542$, and the tip radius is $15\ \text{nm}$. The vertical lines marked by Roman numerals are discussed in Figure 12. 43

Figure 11. $F-d$ histories and indentation depth predictions at $A^{ratio} = 0.5$ for a range of relaxation times (τ) are demonstrated. The τ values and other simulation parameters are identical to the ones in Figure 10 (b). The indentation depth, E_{ts}, and V_{ts} corresponding to the F-d histories in (a) are graphed as a function of τ non-dimensionalized by the tip-sample interaction time. Note that each of the cycles 1-8 in (a) has a different interaction time. 44

Figure 12. (a) Energy dissipation (E_{ts}) vs. relaxation time (τ) and (b) Virial (V_{ts}) vs. τ for a series of $A^{ratio} = 0.3, 0.5, 0.7$, and 0.9 that are specified in Figure 10 by vertical dashed lines labeled I, II, III, IV, respectively. All of the simulation parameters are identical to the ones in Figure 10. 45

Figure 13. The Energy dissipation (E_{ts}) vs setpoint ratio (A^{ratio}) for (a) different Hamaker (H) constant values, (b) different values of the equilibrium position (z_0). For (a), $z_0 = 0.6\ \text{nm}$ and for (b), $H = 8\times10^{-20}\ \text{J}$. The material properties are the ones recorded in Table 2 for the elastomer. 46

Figure 14. (a) Topography image, (b) Phase lag image, (c) Extracted energy dissipation on a three-phase blend polymer sample with $A^{ratio} = 0.7$ and $A^{free} = 35.9\ \text{nm}$. (d) and (e) show histograms of the extracted energy dissipation and phase lag values acquired over the selected rectangular areas of the PC, PP, and elastomer marked in (b) with corresponding colors. The vertical bold lines shown for each histogram in (d) and (e) represent the mean value for each polymer. The scale bar is shown in (a) represents $1\ \mu\text{m}$ 47

Figure 15. Maximum E_{ts} and A^{ratio} at which the maximum E_{ts} occurs plotted as a function of the relaxation time (τ) and E_0/E_∞ ratio for PP. The employed material properties are listed in Table 3, $A^{free} = 18\ \text{nm}$, $K = 28\ \text{N/m}$, and other parameters are identical to the ones described in the experiments section. 48

Figure 16. Comparison between theory and experiment for the three phases following calibration of τ and E_0 to best match the amount E_{ts} and the A^{ratio} at which it occurs in the experimental data acquired with $A^{free} = 35.9\,\text{nm}$. A cubic polynomial is fitted to theory and experimental data to facilitate the identification of the maximum E_{ts} location and magnitude. To help to clarify the regime of the oscillation, the 90-degree phase lag is marked by a green horizontal dashed line. 49

Figure 17. Comparison of computational predictions and experimental results for $A^{free} = 18\,\text{nm}$ on the three polymer phases. The material property data used for the computation (Table 2) are based on quasi-static force curves, theoretical estimates, and with τ and E_0 calibrated from similar data acquired for $A^{free} = 35.9\,\text{nm}$ (Figure 16). The observed discrepancy between simulation and experimental results are less than 11%, 11%, and 22% for Elastomer, PP, and PC, respectively. 51

Figure 18. (a) Bimodal AFM simultaneously excites the first and a higher eigenmode of the microcantilever. (b) The resulting tip trajectory is assumed to be the sum of two harmonics whose steady-state amplitudes and phases change due to the tip-sample interaction and the microcantilever properties. In this figure ω_i is the excitation frequency and A_i and ϕ_i are the amplitude and phase lag relative to the excitation force of the i^{th} mode. Z and $d(t)$ are the distance of the microcantilever base and tip with respect to the undeformed surface level, respectively. $q(t)$ is the microcantilever tip deflection. 55

Figure 19. The algorithm proposed in this work for predicting instrument observables in bimodal AFM through simultaneous compliance of the amplitude reduction formulas for both driven modes. 64

Figure 20. Validation of Eqn.'s (39) and (40) against previously published bimodal AFM experimental data *[42]* and simulation results extracted using the AMAC tool of VEDA *[74]* on a Silicon sample illustrates excellent agreement. The A_1^{ratio} range used for these simulations is between 0.1 and 0.9. The employed parameters in these simulations are as follows: $A_{01} = 10\,\text{nm}$, $A_{02} = 1\,\text{nm}$, $H = 9.03\times10^{-20}\,\text{J}$, $k_1 = 0.9\,\text{N/m}$, $k_2 = 35.2\,\text{N/m}$, $f_1 = 48.913\,\text{kHz}$, $f_2 = 306.194\,\text{kHz}$, $Q_1 = 255$, and $Q_2 = 1000$ *[42]*. 66

Figure 21. Validation against bimodal AFM simulation results extracted using the AMAC tool of VEDA [74] on an elastic sample illustrates perfect agreement with the proposed algorithm. The used values for material properties, microcantilever, and DMT model parameters are: $A_{01} = 50\,\text{nm}$, $A_{02} = 1\,\text{nm}$, $f_2/f_1 = 6.26$, $E = 1\,\text{GPa}$, and $H = 7.55\times10^{-20}\,\text{J}$. The Ar_1 range used for these simulations is between 0.1 and 0.9. 66

Figure 22. Study of the bimodal observables' sensitivity to the effective creep time of the polymer (τ). Selected τ values are stated in the legends and the range is between $3.2\times10^{-5}\,\text{s}$ to $3.2\times10^{-10}\,\text{s}$. 68

Figure 23. Study of the bimodal observables' dependence on the surface adhesion (quantified as $HR/6z_0^2$) and viscoelasticity level. The first row (a-c) and second row (d-f) simulations have

smaller and larger adhesions associated with $H = 1\times10^{-20}$ J and $H = 7\times10^{-20}$ J, respectively. The selection of E_0 and E_∞ in the performed simulations are done based on the "Latin hypercube sampling" method. The used material and interaction parameters are stated in the text. In these conducted simulations $R = 3$ nm, $A_1^{ratio} = 0.5$, $\nu = 0.49$, and $\tau = 0.1$ μs 70

Figure 24. Bimodal images of the PS-LDPE sample illustrate phase lag of the first and second mode, and amplitude of the 2nd mode from left to right, respectively. The associated histograms are shown in the second row. The size of the images is 4×4 μm 73

Figure 25. The estimates for adhesion force, E_∞ and E_0 values for the scanned polymer domains are predicted using the proposed algorithm. The static adhesion is calculated based on $HR/6z_0^2$. 75

Figure 26. The tip-sample interaction schematic illustrating the parameters used in the model. Dashed lines on the surface represent the surface rest level before the deformation. 79

Figure 27. Computational stability improvements by employing generalized Euler's method (Eqn. (72)) with (a): $n_E = 1$ in comparison with (b): forward Euler's method. The rigid tip oscillates through a sinusoidal wave and interacts with the LDPE surface as characterized in Table 8. All the employed simulation parameters for (a) and (b) are identical to enable robustness comparison. The surface adhesion level is regulated by employing various z_0 which are mentioned in the figures. 85

Figure 28. The interaction between a rigid axisymmetric paraboloid tip oscillating through a prescribed triangular wave and a viscoelastic surface is simulated using EAM. The triangular excitation velocities are (a) ±5 μm/s, (b) ±2 μm/s, and (c) ±1 μm/s. The employed material and interaction parameters are identical with the ones used by Attard[2] to facilitate comparison. ... 87

Figure 29. Comparison of the convergence performance of different configurations of EAM implementation as listed in Table 9. The graphs are color-coded according to legends of graph 'a' and the labels defined in Table 9. The insets of the second-row graphs are intended to envision 1% error criteria of the energy parameters with respect to exact solutions. 89

Figure 30. Visualization of F-d history convergence to the exact solution by increasing the number of employed basis functions (n_b). The surface and LJ interaction parameters are listed in Table 8. 90

Figure 31. Elapsed time to compute a tip-surface interaction cycle using different EAM configurations as listed in Table 9. The labels in the legend are defined in the first column of Table 9. The surface and interaction parameters are listed in Table 8. It shows the computational rate of EAM is about three orders of magnitude faster than the original iterative approach proposed by Attard[2, 79]. All simulations are carried out on a typical desktop computer. 91

Figure 32. AFM force spectroscopy schematics and used parameters. In this mode, the input signal to Z-piezo prescribes the defined Z motion. The microcantilever moves toward the surface, indents, and then retracts as it reaches the defined force setpoint. Tip and surface parameters are shown in Figure 26. 92

Figure 33. Study the surface-microcantilever ensemble dynamics in AFM force spectroscopy. (a) shows the predicted microcantilever deflection during one oscillation cycle. (b) and (c) illustrate the predicted F-Z and F-d curves, respectively. The blue and red solid lines represent the approach and retraction branches of the force curve computed using EAM with $n_b = 25$, respectively. The dashed black line is computed using the explicit approach. 93

Figure 34. Computed (a): Phase lag (ϕ), (b): Energy dissipation (E_{ts}), and (c): virial (V_{ts}) od AM-AFM dynamic approach/retract curves on an LDPE sample. In these simulations $u(r,t)$ is approximated according to Eqn. (61) with $n_b = 25$. The employed A_0, f, Q, and k are 15 nm, 278 kHz, 429.5, and 28.1 N/m, respectively. The results are in excellent agreement with exact solutions. 95

Figure 35. The tip-surface interaction in a single cycle of AM-AFM on the LDPE surface in the time domain as predicted by EAM (blue area) and exact (dashed black line) approaches. The surface characteristic parameters are listed in Table 8. The instant associated with each of the images is noted at the left-down of each picture. a-f and g-l image series illustrate the approach and retraction parts of the cycle, respectively. The arrows are to assist in realizing the tip velocity direction. The frame dimensions are in nm. 96

Figure 36. (a) Schematics of an interacting AFM microcantilever tip and a surface. The relevant parameters characterizing the tip-surface distance, tip deflection, and surface deformation are labeled and shown in the image. (b) The equivalent point-mass model representation for the uniform and rectangular microcantilever excited at a sub-resonant frequency. 99

Figure 37. Schematic of PFT AFM on a soft sample. The dashed red-blue curve shows the trajectory of the microcantilever base during a cycle (Eqn. (77)). The black solid curve represents the tip deflection (q) during a cycle. The transient ringing signal of the retracting microcantilever occurs when the tip becomes fully detached from the surface. This part of the force curve is usually filtered out in PFT mode. 100

Figure 38. The flowchart illustrates the two-step method used to estimate the material viscoelastic and adhesive properties based on an experimentally acquired PFT F-t curve. The procedure employs a machine learning algorithm that is trained by a dataset of forward simulation results. 101

Figure 39. The algorithm proposed in this work for predicting the F-d curve in PFT AFM. the axisymmetric tip profile is defined by $f_{tip}(r)$. 102

Figure 40. (a) Developed FE model includes a spherical rigid indenter which on one side interacts with a surface and from the other side is connected to an oscillating plate by a linear spring. This ensemble represents the sub-resonant excited cantilever in PFT AFM. (b) The agreement between the F-Z curves predicted by the proposed model and the FE model is presented in this graph. The surface adhesive forces are not included in the FE model. The inset shows the effective von Mises stress distribution during the interaction time. 105

Figure 41. F-Z predictions by the proposed model and the ones provided in Attard's original Work for two different tip velocities. The identical employed surface properties in both models are: $E_0 = 10$ GPa, $E_0 = 1$ GPa, $\tau = 1$ ms, $H = 1\times10^{-19}$ J, and $z_0 = 0.5$ nm. Tip radius is $R = 10\,\mu m$.

The velocities of Z triangular waveforms are different between graphs: (a) $\pm 5\ \mu m/s$, (b) $\pm 2\ \mu m/s$, (c) $\pm 1\ \mu m/s$. 106

Figure 42. Simulation results for a single cycle of PFT AFM on an elastomer sample. The labels for each sub-figure are specified at its bottom left. The operational parameters and cantilever and surface properties are listed in Table 11 under column "*". Graph (a) illustrates the tip deflection and surface deformation at r=0 (dashed line) during interaction time and graph (b) depicts the predicted F-d curve. The red and blue segments of these graphs represent the approach and retraction phases of the cycle. 4 instances during the interaction time including snap-in and snap-off phenomena are marked with vertical dotted lines and labeled as I, II, III, and IV in the graph (a). The predicted surface deformation as well as the tip position at these instances are shown in (c), (d), (e), and (f) graphs, respectively. The associated pressure distribution over the contact region at these instances are also shown in (g), (h), (i), and (j) graphs, respectively. The green and red areas in (g), (h), (i), and (j) graphs represent attractive and repulsive interaction pressures, respectively. 109

Figure 43. Predicted F-d curves variation when the operational parameters and surface viscoelastic/adhesive properties are systematically changed. The labels for each sub-figure are specified at its bottom left. At each of the graphs except (c), only one of the parameters which are specified in the legend is changed and other surface properties or operational parameters are identical. At (c), both E_0 and E_∞ are changed while the E_∞/E_0 ratio remains constant. Full input parameters used for each set of simulations are listed in Table 11 with the same label specified at each graph. For all these simulations $\tau = 1\ \mu s$. Arrows are intended to visually help to distinguish the predicted changes on the F-d curve by increasing the parameter of interest at each sub-figure. 110

Figure 44. The used F-t curve parametrization method. The red dots shown on the curve are the 15 representative <F, t> pairs for the stable regions of an F-t curve acquired on a polyolefin-based elastomer (Engage 8003, The Dow Chemical Company). 113

Figure 45. A typical set of the models' predictive accuracy evaluation charts when 20% of the training data is considered as test data. In these charts, the actual and predicted values, which ideally supposed to be equal (represented as dashed red lines), for E_∞, E_0, H, and Z using each of the employed ML models are illustrated and compared..... 116

ABSTRACT

Atomic force microscopy (AFM) is widely used to study material properties and domain heterogeneity of polymers. In both quasi-static force spectroscopy and dynamic AFM, challenging complexities such as the presence of different effective tip-surface forces, surface dynamics, and material viscoelasticity can occur on polymer samples. Many models that attempt to link experimental observables to contact mechanics fail to rigorously account for these complexities. This may lead to inaccurate and unreliable predictions, especially when examining soft polymers. Therefore, having access to rigorous models that can facilitate the understanding of the underlying phenomena during tip-surface interaction, explain the observations, and make reliable and accurate predictions, is of great interest. Among the previously developed models, Attard et al. proposed a novel non-Hertzian-based model that has a versatile ability to systematically incorporate different linear viscoelasticity constitutive models and surface adhesive forces. However, the implementation of Attard's model into the AFM framework is challenging.

In a series of studies, we improve the computational speed and stability of Attard's viscoelastic contact model and embed it into an AFM framework by proposing algorithms for three AFM operational modes: tapping mode, bimodal, and peak force tapping. For each mode, the results are successfully verified/validated against other reliable AFM codes, FEM simulations, and experiments. The algorithms' predictions illustrate how viscoelasticity and surface adhesive hysteresis of polymeric samples is reflected in AFM observables. However, since Attard's model does not lead to a closed-form solution for tip-surface interaction force, using that to quantify the surface mechanical properties based on the AFM observables is not straightforward. Therefore, we utilize the data analytics-based approaches such as linear regression and machine learning algorithms to enable the material viscoelasticity and adhesive parameters estimation based on the provided instrument observables.

The set of results reported in this thesis improves the current knowledge about complex phenomena that occur during tip-surface interactions, especially on soft-viscoelastic-adhesive polymers. The introduced "improved Attard's model" fulfills the need for a continuum mechanics viscoelasticity contact model that rigorously captures the complexities of such samples. The viscoelasticity contact model and the proposed inverse solution algorithms in this thesis facilitate

quantitative measurement and discrimination of the surface adhesive and viscoelastic properties based on the acquired nanoscale AFM maps of polymeric samples.

1. INTRODUCTION

Atomic force microscopy (AFM) techniques are suitable tools to characterize nanoscale mechanical properties of surfaces such as elasticity, plasticity, failure, adhesion, friction, and wear. However, accurately nanoscale mapping of the mechanical properties of viscoelastic/adhesive surfaces of polymers and biological samples using AFM is challenging. Due to the wide range of the viscoelastic substances and their broad applications, their nanoscale mechanical properties characterization and consequently their resultant microscale behavior is of widespread importance. The encountered hurdles in accurately relating AFM observables to mechanical properties of this category of materials is mostly due to the complexity of their mechanical response in comparison with elastic materials. The simplistic *ad hoc* viscoelastic contact models, which are commonly used to connect AFM observables to mechanical properties of viscoelastic materials, lack the required reliability and accuracy [1]. Therefore, a fast first-principles viscoelastic contact mechanics model that enables rigorous prediction and interpretation of AFM images on soft, adhesive, and viscoelastic materials is needed. In this thesis, we first critically compare the proposed viscoelastic contact models in terms of their reliability and inclusivity of the effective parameters in contact phenomena on viscoelastic/adhesive samples. Next, we improve upon the viscoelastic contact model proposed by Attard [2] as arguably the most advanced contact mechanics model for such samples. Finally, a set of algorithms are developed to implement Attard's model in the AFM framework to predict and interpret the tip-surface interactions on viscoelastic/adhesive samples in selected AFM modes. For each of the assessed AFM modalities in this thesis, we complement the computational predictions by applying the developed algorithms to acquired AFM experimental data.

1.1 Atomic force microscopy

Scanning tunneling microscopy (STM) [3], which earned its inventors the 1986 Nobel Prize in Physics, can achieve atomic resolution when imaging conductive samples. In STM, a sharp conductive tip is placed in the proximity of a conducting surface. A bias voltage is applied to the probe-sample ensemble and the transmitted tunneling current is used to estimate the tip-surface distance. High-resolution STM facilitates imaging and manipulation of atoms [4].

Furthermore, STM can reconstruct the topography of a surface of a conductive sample by rastering the tip over the sample and using a feedback loop to maintain a constant tunneling current. Although STM made great breakthroughs in atomic-level resolution imaging [5], a major limitation is that it can be used only for electrically conductive samples. To overcome this, a new instrument called "Atomic Force Microscopy" (AFM)[6] was introduced by Binnig et al. in 1986.

In AFM, instead of tunneling current, the interaction force between the tip and surface is measured and interpreted. In contrast with STM, AFM can image both conductive and non-conductive materials. The interaction force sensed by the tip is measured through the observed deflection of a microcantilever on which the tip is mounted. The first AFM used an STM probe to measure the defection of the microcantilever. Since these initial measurements, AFM has made significant advances in design and methodology enabling it to grow into a popular multifunctional tool for nanoscale measurements. Other than the surface topography, AFM now can provide information about surface properties such as: mechanical, electrical, magnetic, chemical, and thermal properties of a wide variety of either conductive or non-conductive surfaces and materials [7, 8]. A wide range of AFM modes, techniques, and methods have been devised to visualize or manipulate surface and subsurface properties at the microscale, nanoscale, and atomic scale [9-11].

Contact mode AFM, the first AFM mode developed, uses a single control loop to maintain a constant microcantilever tip deflection (q) during imaging. The control loop in contact mode adjusts the altitude of the microcantilever tip (Z) while the AFM tip scans the surface in physical contact so that the tip-surface interaction force (F_{ts}) during imaging is constant (Figure 1). In contact mode, q and F_{ts} during imaging are related by the microcantilever's bending steady-state solution: $F_{ts} = k \times q$, where k is the quasi-static microcantilever bending stiffness. The conceptual, as well as implementation simplicity of contact mode, is helpful from a training point of view. Contact mode is also advantageous due to its ability to generate high-resolution images with even atomic level contrast [12]. However, the presence of substantial non-controlled lateral forces is considered as a drawback for contact mode. Large lateral forces can prevent the imaging of fragile surfaces that are common in biological applications. However, one can take advantage of the effect of lateral forces in contact mode to study the relevant parameters such as surface friction, adhesion,

and wear forces at the nanoscale [13-15]. A final limitation of contact mode is that it only provides information on sample topography and does not directly provide information on sample properties.

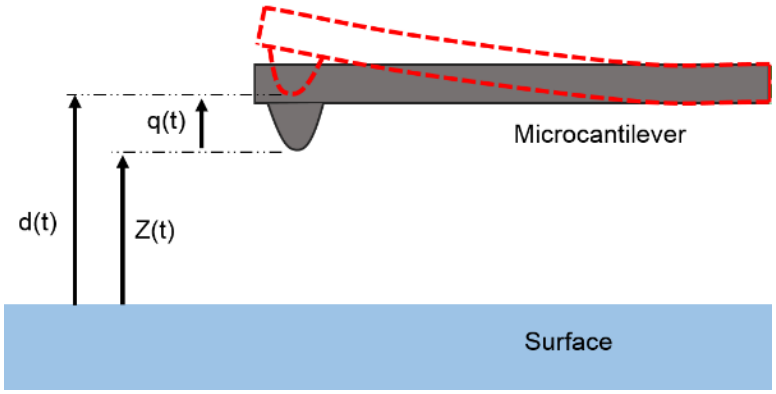

Figure 1. Schematic of AFM microcantilever and associated distance parameters with the surface. Z(t) is the distance between the undeflected tip and the undeformed surface, q(t) is the deflection of the cantilever, and d(t) is the separation between the deflected tip and undeformed surface. as obvious: $d(t) = Z(t) + q(t)$

To overcome the shortcomings of contact mode AFM, dynamic atomic force microscopy (dAFM) modes were introduced in which the microcantilever is vibrated by an excitation source and the tip is in intermittent contact with the sample [9]. The dAFM modes are advantageous in that they: (1) they allow imaging of fragile samples without damaging the soft surfaces, (b) they facilitate the spectroscopy of samples in the liquid environment [16, 17], (c) they minimize the effects of lateral forces [18, 19] and (d) they increase the number of the instrument observables enabling measurements of additional sample properties [20]. The improvements provided by introducing dAFM modes enable the study of delicate biological samples such as DNA, cells, viruses, and proteins in liquid and under conditions like their native environments. Furthermore, dAFM modes open the door to in situ [21] or more recently, video-rate [22] studies of the biological samples. The two initially developed dAFM modes are amplitude-modulation AFM (AM-AFM) [23] and frequency-modulation AFM (FM-AFM) [24].

In AM-AFM (also known as tapping mode), the microcantilever is excited at a fixed frequency, which usually is the first resonance frequency of the microcantilever. When the oscillating microcantilever approaches the surface, the tip-surface interaction force causes the oscillation amplitude and the phase lag between the response and excitation signal (ϕ) to change. The ratio of the microcantilever's tip oscillation amplitude when it interacts with the sample and

when it is far from the sample (negligible interaction), A and A_0 respectively, is termed the amplitude ratio $\left(A^{ratio} = A/A_0\right)$. In AM-AFM the feedback controller tracks the surface topography during a scan by maintaining A^{ratio} at a user-defined value through adjusting Z. The phase lag channel (ϕ) at AM-AFM enables discrimination of surface domains with different mechanical properties. However, the responsiveness of the microcantilever to the topographical or compositional changes on the surface is a function of the transient time scale of the microcantilever: $\tau = 2Q/\omega$ where, Q and ω are, respectively, the quality factor and the resonance frequency of the microcantilever fundamental eigenmode when it is not interacting with the surface [9]. This constrains the scanning speed of AFM in higher Q environments like UHV and encourages higher speed scans in lower Q environments such as air and liquid.

In FM-AFM, both the amplitude and phase lag of the oscillating tip are maintained constant during scanning. A phase-locked-loop (PLL) increases/decreases the excitation frequency by Δf, which is called "frequency shift", to always maintain $\phi = 90^{\circ}$ with respect to the input signal during scanning of a pixel of an FM-AFM image. The excitation frequency is initially set to the first resonance frequency of the microcantilever when it is far from the sample. The oscillation amplitude of the tip is also preserved by adjusting the amplitude of the excitation signal by ΔA_0. This shows that the required control scheme for FM-AFM is more complicated than AM-AFM. There are two feedback loops and two observables in FM-AFM: drive and frequency shift which allow separating the contributions of conservative and dissipative interaction forces [25-27]. In contrast with AM-AFM, the time scale of the microcantilever in FM-AFM is no longer a function of the microcantilever's Q factor: $\tau = 1/\omega$ [28].

The oscillation response of the microcantilever at different frequencies carries details of the nonlinear and complicated tip-surface interaction force. In AM-AFM, the amplitude of higher harmonic oscillations is more than two orders of magnitude smaller than the amplitude of the first mode [29] and is often associated with small signal-to-noise ratios. However, in multifrequency AFM [30], in which the microcantilever is excited and/or its dynamic response is measured at two or more frequencies [31], the employed lock-ins can accurately demodulate the output signal into the corresponding observable channels. In multifrequency AFM, as a subset of the dAFM family, the microcantilever is mostly excited/measured at harmonics of the fundamental frequency [32-

34] and/or at two or more flexural/torsional eigenfrequencies of the microcantilever [30, 35-37]. Bimodal AFM is the most common technique under multifrequency AFM in which first and another (mostly second) eigenmodes of the microcantilever are simultaneously excited. Several configurations for bimodal AFM are devised and deployed based on the utilized control schemes for the first and secondary excited modes of the microcantilever[38-40]. Among those, the most direct configuration is the one in which bimodal AFM scans the sample by regulating the amplitude ratio of the first mode (AM) and allowing the amplitude and phase of the secondary mode free to respond to the interaction between tip and surface[41]. In this configuration, both the phase and amplitude of the secondary mode are open to reflect the local surface properties [42]. The additional information channels provided by bimodal AFM can be used for material characterization purposes such as estimating the viscoelastic or adhesive properties of polymeric surfaces [37, 43-45]. Bimodal (or more generally multifrequency) AFM is mainly aimed to fulfill the demand for adding high-contrast compositional channels without significantly changing tapping forces, i.e. the forces are gentle [10, 39, 46]. However, even when there is no specific commensurate relationship between the two excitation frequencies, an undesirable interference of the secondary mode oscillation on the first mode dynamics and observables may be perceived. This interference may influence and disturb the first mode observables including the topography image of the surface. It is experimentally suggested by others to select a smaller ratio of the free amplitudes of the first and second modes to avoid the above-mentioned crosstalk between excited modes [47-50]. However, the underlying mechanism of the crosstalk between modes in bimodal AFM is not yet well understood.

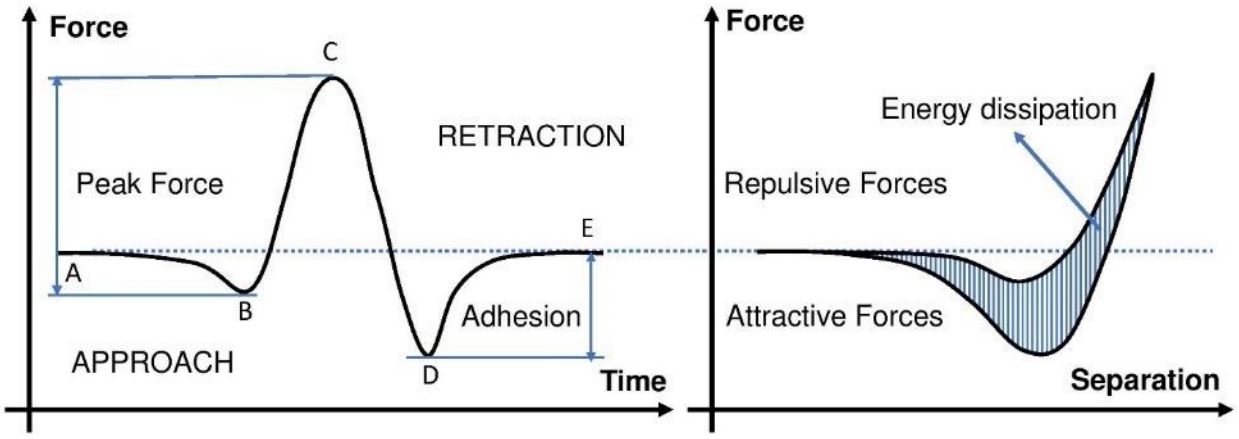

Figure 2. Force-time and force-separation curves for a typical PFT experiment. The relevant parameters are noted in the pictures.

Off-resonance AFM force spectroscopy modes such as quasi-static loading are historically the first developed AFM modes designed to estimate the mechanical properties of the samples [51]. In these modes, the microcantilever as-a-whole approaches, interacts, and retracts off the sample at each cycle while the deflection of the microcantilever is monitored. Usually, a 4-segment photodiode sensor is used to trace the interaction force experienced by the microcantilever at each sampling-step through the detected deflection as shown in Figure 2. This conveys information about the surface mechanical properties such as elastic/viscoelastic modulus, surface energy, and adhesion. During one oscillation cycle, the microcantilever undergoes positive/negative deflections due to repulsive/attractive interaction forces between the tip and the surface. Different regions of the acquired force vs. distance curves are used to extract corresponding surface properties based on the utilized contact mechanics models. Bruker's exclusive peak force tapping (PFT AFM) mode falls in this category which acquires a force-curve each time it taps on the surface while scanning the surface. These force curves can be used to estimate and map the surface mechanical properties with high resolution. The feedback parameter in PFT is the peak force value of the force-curve (Figure 2) which is maintained constant during scanning. In PFT, the Z excitation frequency is far below the fundamental resonance frequency and therefore, the quasi-static microcantilever bending model still holds to link the tip-surface interaction force to the observed deflection.

1.2 Mathematical models of tip-sample interaction forces

The Hertz model that can predict the contact force between an elastic sphere and an elastic half-space is the oldest classical contact model [52]. To accurately predict the contact force (F_{ts}) as a function of the indentation depth (δ), the Hertz model requires the contact radius (a) to be much smaller than the radius of the sphere(R). When the sphere is much stiffer than the half-space (in this case, we call the sphere "tip", hereinafter), the Hertz model provides the following closed-form equation to calculate the interaction force:

$$F_{ts} = \frac{4E}{3\left(1-\nu^2\right)}\sqrt{R}\,\delta^{3/2} \tag{1}$$

where, E and ν are Young's modulus and Poisson's ratio of the sample, respectively. The Hertz model ignores the surface adhesive forces and cannot make reliable and accurate predictions when attractive forces are significant.

Table 1. A comparison between well-known continuum mechanics contact models in terms of their ability to include surface forces, viscoelasticity, and surface dynamics. These are important parameters which are needed to be accounted for when working with soft, adhesive, and viscoelastic polymers.

Model	Adhesive Forces	Viscoelasticity	Surface Dynamics
Hertz [52]	×	×	×
DMT [53]	✓	×	×
JKR [54]	✓	×	×
Maugis [55]	✓	×	×
Ting [56]	×	✓	×
Attard [2]	✓	✓	✓

Since then, others have introduced new models to enhance and improve upon the Hertz model by removing the model's constraints such as the spherical shape of the tip and a/R ratio requirement of the model [57-59]. Two well-known models have been introduced in which the role of the surface adhesive forces on the contact phenomenon is observed: Derjaguin-Muller-Toporov (DMT) [53] and Johnson-Kendall-Roberts (JKR) [54]. It is widely accepted that the DMT model is more appropriate for contacts on "stiffer" samples while JKR is more suitable for "softer" and more adhesive samples. To quantify this qualitative relevance criterion for JKR and DMT models, Tabor [60] proposed a unitless number (Tabor parameter) to determine whether DMT or JKR is appropriate for a situation. Later, Maugis [55] developed a model that provides the bridge between JKR and DMT limits which can be used on either soft or stiff samples and it also includes the effect of the presence of surface adhesive forces. In Table 1, a comparison between several continuum mechanics-based contact modes is provided. These models are compared in terms of their inclusivity of the effective parameters when studying tip-surface interaction on soft

viscoelastic polymers. This table also can be used as a guide to distinguish the reliability criterion for each of these contact models. The *ad hoc* viscoelasticity models are not included in the list.

The other deficiency of the Hertz model is its constraint on making reliable predictions for contact phenomena on materials with more complex behavior such as viscoelastic materials. It is specifically an obstacle to study the mechanical properties of polymers as a large class of materials with ubiquitous usage in different fields [61-66]. Constitutive models which represent the material's viscoelasticity behavior were first incorporated into the contact problems firstly through an *ad hoc* addition of a Kelvin-Voigt viscoelasticity assumption within Hertzian or DMT contact mechanics theories [67-73]:

$$F_{ts}(d,\dot{d}) = \begin{cases} 0, & d > 0 \\ \frac{4}{3}E^*\sqrt{R}(-d)^{3/2} - \eta\dot{d}\sqrt{-Rd}, & d \le 0 \end{cases} \quad (2)$$

where F_{ts} is assumed to be a function of the tip-sample gap d and tip velocity $\dot{d}$. E^*, η, and R are the effective tip-sample elastic modulus, sample viscosity, and tip radius, respectively, where:

$$\frac{1}{E^*} = \frac{1-\nu_{tip}^2}{E_{tip}} + \frac{1-\nu_{surface}^2}{E_{surface}} \quad (3)$$

There are at least two fundamental problems with this *ad hoc* viscoelasticity model. First, when the tip is interacting with the sample ($d < 0$) and it is withdrawing from the sample ($\dot{d} > 0$), it is possible that $F_{ts} < 0$ for sufficiently large $\dot{d}$ and η. However, the Hertz contact model should only include repulsive surface forces ($F_{ts} \ge 0$), so this outcome of the model (Eq. (2)) is non-physical. Put another way, as the tip withdraws, the deformed sample does not return to its original condition instantly, but rather it takes a finite time to relax due to viscoelasticity allowing the tip to detach from the sample before $d = 0$. However, the *ad hoc* viscoelasticity model cannot account for this and applies an attractive force to constrain the tip to withdraw only as fast as the sample can relax. This is seen clearly in a force-indentation history during a single tap that is simulated using Hertz contact mechanics with an *ad hoc* Kelvin-Voigt viscoelasticity model which is generated by VEDA (Virtual Environment for Dynamic AFM) [74] as shown in Figure 3. The presence of attractive forces during the retraction phase arises from the *ad hoc* and incorrect assumption that the contact area history of the tip during the retraction phase of the oscillation for a viscoelastic material is not different from that of a purely elastic material. In contrast, Ting's model [56]

modifies the Hertzian contact model by using the viscoelastic correspondence principle and correctly predicts the contact area evolution for tip interaction with a linear viscoelastic solid. However, since surface forces are ignored in Ting's model, it cannot predict surface deformations occurring before tip-sample contact nor spontaneous and non-equilibrium surface instabilities such as sample snap off and jump to contact with the tip. These phenomena are especially relevant for dAFM on soft materials or viscoelastic surfaces with a moderate to large adhesion. In recognition of the likely role of surface relaxation in dAFM, recent works [75, 76] have included surface relaxation within dAFM simulations and modeled the contact as a bed of linear springs and viscous dashpots. However, they do not consider contact mechanics, 3D continuum viscoelasticity, and surface forces in a self-consistent manner. Therefore, a fast first-principles viscoelastic contact mechanics model that enables rigorous prediction and interpretation of AFM images on soft, adhesive, and viscoelastic polymers is still lacking.

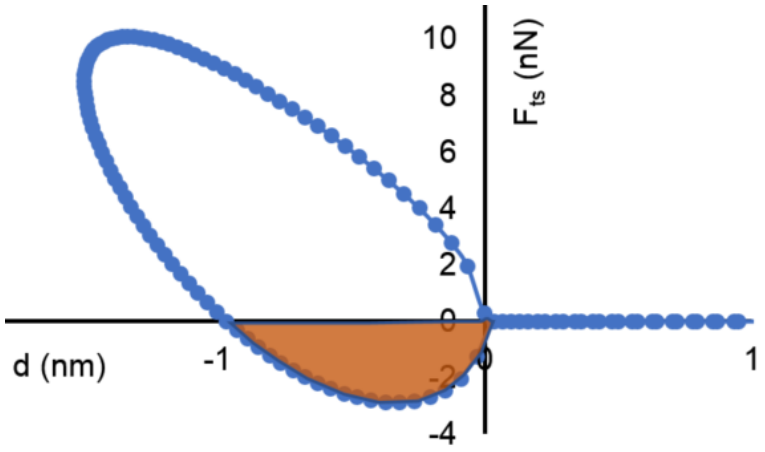

Figure 3. F – d history during a single taping cycle predicted by the AMAC tool in VEDA [77] using the Hertz model including Kelvin-Voigt viscoelasticity in an *ad hoc* manner. The computational input parameters are as follows: free amplitude: 60 nm; natural and driving frequency: 75 kHz; Q = 150; approach velocity: 200 nm/s; tip radius: 10 nm. The viscoelastic surface is characterized by E = 1 GPa and η = 500 Pa·s. Note that the retraction phase features a region of attractive forces shaded in brown which is an artifact of underlying model assumptions.

Attard and co-workers [2, 78-81] introduced a fundamentally different approach for including the relevant physics of the contact between an axisymmetric tip and an adhesive viscoelastic surface using the Boussinesq solution [82] of a tip-sample contact problem. Computationally, the proposed approach is akin to a boundary element method in that the sample surface is discretized with a mesh and the surface deformation and pressure are computed at each mesh point in time explicitly. Attard's approach does away with *ad hoc* assumptions of prior

models discussed before and computes the surface deformation field self-consistently using 3D linear elasticity/viscoelasticity and arbitrary surface forces. Attard's model has significant advantages relative to models that use an *ad hoc* approach to add viscoelasticity to DMT or Hertz based models:

1. Hertz and DMT based models with *ad hoc* Kelvin-Voigt elements assume a certain dependence of contact area on indentation depth regardless of history of deformation. The history dependence of the contact area was studied by Ting [56] but his approach does not include surface forces. Attard's model inherently addresses this dependence since it solves a 3-dimensional linear viscoelastic deformation problem without assumptions on contact area evolution. As a result, the detachment of the tip from the surface is correctly computed, unlike in the *ad hoc* viscoelastic models.
2. Hertz and DMT approaches with *ad hoc* Kelvin Voigt viscoelasticity are generally unable to predict viscoelastic dissipation when the tip oscillates in the attractive regime. Since Attard's model includes surface forces it allows for the viscoelastic surface to deform and relax and dissipate energy even if the tip oscillates in an attractive regime with the surface.
3. A viscoelastic surface will continue to relax as the oscillating tip detaches and moves away from the surface. This is an expected surface behavior that is not predicted by *ad hoc* Kelvin Voigt elements added on to classical contact mechanics models.
4. Finally, *ad hoc* Kelvin Voigt modifications of classical contact mechanics models can lead to artifacts such as the creation of negative tip-sample interaction forces even in the absence of surface forces. Attard's model systematically includes both general surface force models as well as linear 3-dimensional viscoelasticity of the sample surface and avoid these artifacts.

While utilizing the Hertz/DMT models with *ad hoc* Kelvin Voigt viscoelasticity may provide less inaccurate results on stiff samples with low adhesion and low viscoelasticity, to establish a relationship between AFM observables and local physical properties of soft, adhesive, and highly viscoelastic materials it may be desirable to use more accurate models such as Attard's model. However, since the algorithm is based on an iterative loop, it is computationally expensive. Moreover, the approach requires precise knowledge of the tip motion, which is not known a priori in dAFM, but rather depends on the material properties and operating conditions. In the following

chapters, detailed discussions on the underlying theory of Attard's approach and the proposed computational approach is provided.

1.3 Overview of the work

In this series of works, we both accelerate the computational method introduced by Attard and propose algorithms to embed it within the selected AFM modes (AM-AFM, bimodal AFM, PFT) to recover the instrument observables. Attard's model was chosen due to its systematic inclusion of different effective parameters in contact phenomena on soft polymers such as surface adhesive forces, material viscoelasticity, and surface dynamics that make it capable of making more realistic predictions. The proposed algorithms allow for the self-consistent inclusion of microcantilever dynamics, surface forces, and linear three-dimensional material viscoelasticity within AFM simulations. The developed codes and proposed improvements and approaches are all verified/validated by comparison with the results provided by Attard [2], FEM simulation results, VEDA simulation results, and experimental data for the corresponding modes. The approach is then used to study the effects of polymer relaxation modes and surface forces on interaction force, surface deformation history, and AFM observables. We believe this set of works will shed a light on the ongoing research in the interpretation of AFM observables on soft polymers. Each of chapters 2-5 of this thesis is constructed based on the published/ under review/ under preparation publication.

In chapter 2, we present a computational method that enables the prediction and interpretation of AM-AFM observables on samples with arbitrary surface forces and linear viscoelastic constitutive properties with a first-principles approach. The approach embeds the accelerated version of Attard's model within the tapping mode amplitude reduction formula (or equivalently frequency modulation frequency shift/damping formula) to recover the force history and instrument observables as a function of the setpoint amplitude or Z-distance. The role of surface forces and polymer relaxation times on the phase lag, energy dissipation, and surface deformation history is clarified. Experimental data on energy dissipation in AM-AFM for different free amplitudes and setpoint ratios are presented on a three-polymer blend consisting of well-dispersed phases of polypropylene, polycarbonate, and elastomer. An approach to experimental validation of the computational results is presented and analyzed.

In chapter 3, we first propose an algorithm that systematically accommodates surface forces and linearly viscoelastic three-dimensional deformation computed via Attard's model into a bimodal AFM framework. The proposed algorithm simultaneously satisfies the amplitude reduction formulas for both resonant eigenmodes and enables the rigorous prediction and interpretation of bimodal AFM observables with a first-principles approach. The dependence of bimodal observables on local adhesion and standard linear solid (SLS) constitutive parameters as well as the operating conditions are predicted. Secondly, we present an inverse method to predict quantitatively the local adhesion and SLS viscoelastic parameters from bimodal data acquired on a heterogeneous sample. We demonstrate the method experimentally using bimodal AFM on a polystyrene-low density polyethylene (PS-LDPE) polymer blend. This inverse method enables the quantitative discrimination of adhesion and viscoelastic properties from bimodal maps of such samples.

In chapter 4, we illustrate a method to render Attard's contact model into a faster and more robust computational tool compared to Attard's original method. In the proposed enhanced Attard's model (EAM) the surface deformation is reconstructed using a complete set of optimized biorthogonal basis functions as opposed to the computationally expensive radial discretization-based approach employed by Attard. The use of higher-order numerical procedures in EAM to solve the model's governing ordinary differential equations (ODEs) leads to more stable solutions even for soft and sticky samples. We also rearranged the original model's formalism to enable a fast and explicit solution of the model ODEs. Implementing these enhancements, EAM is more stable, three orders of magnitude faster, and equally accurate when compared to the original model. These improvements facilitate the inclusion of EAM into simulations of various AFM. This is demonstrated with fast simulations of force-distance curves and amplitude modulation AFM on soft polymer surfaces. On a typical desktop computer, simulation of an amplitude modulation approach curve with EAM takes less than a minute as compared to ≈ 15 hours by the original Attard's model. The Fast and rigorous EAM predictions for AFM on soft, viscoelastic polymers with surface forces provide significant insight into the complex tip-surface interaction phenomena on such samples.

In chapter 5, we develop a forward solution algorithm to predict the PFT AFM Force vs. time (F-t) curves based on the material viscoelastic and adhesive properties. The proposed algorithm can be adapted for other similar off-resonance modes. This algorithm allows the

inclusion of EAM to calculate the tip-surface interaction. Then we use a machine learning (ML) algorithm to tackle the inverse problem and estimate the viscoelastic and adhesive properties of the sample based on the acquired experimental F-t curves. We used the forward solution algorithm to generate the required simulation dataset with a vast range of known input parameters to train the ML algorithm. The method is demonstrated by predicting surface adhesive and viscoelastic properties from PFT AFM measurements on a Dow fabricated elastomer sample.

2. TAPPING MODE ON VISCOELASTIC POLYMER SAMPLES WITH SURFACE FORCES

2.1 Introduction

Dynamic atomic force microscopy (dAFM) offers many advantages and unique capabilities for the nanoscale characterization of advanced polymeric materials [61-66]. dAFM enables the high-resolution imaging of polymer samples in air/vacuum/liquid environments with gentle normal and lateral forces [83], thus allowing for minimally invasive imaging of these soft samples. Moreover, dAFM mode imaging always provides additional channels of observables (phase contrast, energy dissipation, higher harmonics, bimodal phase, etc.), which can be used to render nanoscale compositional contrast [84, 85] to complement topography images.

However, the dAFM compositional contrast on polymers can arise from different material properties (elasticity, viscoelasticity, relaxation times, hysteretic, or van der Waals (vdW) adhesion, etc.) and depends on the operating conditions (setpoint ratio, free amplitude, drive frequency, stiffness, tip radius, and quality factor) [9]. Due to the variety of effective parameters that characterize the physical properties of polymers, the interpretation of the instrument's observables on polymer samples is difficult.

To understand the link between dAFM compositional contrast on polymers and local material properties, a mathematical model that predicts the interaction between the dAFM oscillating tip and the viscoelastic sample surface is required. For example, to interpret contact-mode related AFM methods such as force modulation, or contact resonance, viscoelastic sample models without surface forces are often used [67-73]. However, such approaches cannot be applied to dAFM, where the tip intermittently interacts with the viscoelastic sample surface and requires an accurate and self-consistent inclusion of both surface forces and surface relaxation dynamics. Prior efforts linking dAFM compositional contrast on polymers to local properties have key limitations. For example, early works suggested that dAFM phase-contrast under moderate tapping conditions on polyethylene was merely correlated with polymer density and elasticity [61] rather than viscoelastic properties. However, understanding dAFM on polymers needs computational approaches in which the relevant physics of the interactions are considered in a self-consistent manner.

In this work, we both accelerate the computational method introduced by Attard and embed it within the tapping mode amplitude reduction formula (or equivalently frequency modulation frequency shift/damping formula) to recover the instrument observables (phase contrast/energy dissipation) and force and surface deformation history as a function of the setpoint amplitude or Z distance over adhesive viscoelastic surfaces. The algorithm allows for the self-consistent inclusion of resonant microcantilever dynamics, surface forces, and linear three-dimensional material viscoelasticity within dAFM simulations. The approach is validated by comparison with the results of Attard [78], as well as with VEDA simulations using Ting's model [56]. The approach is then used to study the effects of polymer relaxation modes and surface forces on interaction force and surface deformation history, and TM-AFM/AM-AFM observables such as energy dissipation and phase. Experimental data acquired using TM-AFM/AM-AFM on energy dissipation on a blend of polypropylene, polycarbonate, and elastomer are described. An approach for the experimental validation of computational results is presented and analyzed.

2.2 Theory of the proposed approach

In AM-AFM (commonly known as TM-AFM), a microcantilever with a sharp tip is excited near its fundamental frequency, and the microcantilever's vibration while interacting with the surface of the sample is monitored via a beam bounce technique. Here we review some key concepts from the analytical theory of AM-AFM upon which the proposed approach is based, recognizing that the proposed approach can be easily adapted for frequency modulation AFM (FM-AFM).

For steady-state AM-AFM oscillations in air/vacuum, the tip settles in a well-defined motion[86], which is dominated by the fundamental harmonic of tip motion: $q(t) = A\sin(\omega t - \phi)$, where $q(t)$ is the tip deflection, A is the amplitude of the oscillation, and ϕ is the phase lag relative to the excitation force. Higher harmonics also occur but they are about two orders of magnitude smaller than the fundamental in air or vacuum applications [29, 87]. If we assume that the higher harmonics of tip displacement are negligible compared to the primary harmonic, the unperturbed distance of the tip above the sample surface is Z which is adjusted by the Z piezo, the tip-sample gap is: $d(t) = Z + q(t)$ and $\dot{d}$ is the tip velocity. A schematic of an oscillating tip interacting with a sample is illustrated in Figure 4. During the interaction time, the tip experiences local surface

forces, both conservative and non-conservative. The oscillation amplitude A of the resonant probe decreases once the Z piezo approaches and the microcantilever begins to interact with the sample surface. Under these conditions, the virial $V_{ts}(A,Z)$ and energy dissipation $E_{ts}(A,Z)$ can be calculated as follows:

$$V_{ts} = \frac{1}{T}\int_0^T F_{ts}(Z + A\sin(\omega t - \phi)\,,\, \dot{Z} + A\omega\cos(\omega t - \phi)) \times A\sin(\omega t - \phi)\, dt = V_{ts}(A,Z)\,, \tag{4}$$

$$E_{ts} = \int_0^T F_{ts}(Z + A\sin(\omega t - \phi)\,,\, \dot{Z} + A\omega\cos(\omega t - \phi)) \times A\omega\cos(\omega t - \phi)\, dt = E_{ts}(A,Z)\,, \tag{5}$$

where F_{ts} is the tip-sample interaction force and T is the time-period of the oscillation. Furthermore, $A^{ratio} = A / A^{free}$, known as the amplitude setpoint ratio (dimensionless), is the ratio of the resonant amplitude A during interaction and the free amplitude (A^{free}) far from the sample. A^{ratio} is related to $E_{ts}(A,Z)$ and $V_{ts}(A,Z)$ using the amplitude reduction formula, which is derived by rearranging the virial and energy dissipation equations [88-90] of AM-AFM. Specifically,

$$A^{ratio} = \frac{1/Q}{\sqrt{\left(\frac{-2\,V_{ts}(A,Z)}{kA^2}\right)^2 + \left(\frac{1}{Q} + \frac{E_{ts}(A,Z)}{\pi kA^2}\right)^2}}\,, \tag{6}$$

where, V_{ts} (eV/cycle) is the virial, E_{ts} (eV/cycle) is the energy dissipation, k (N/m) is the equivalent microcantilever stiffness of the driven eigenmode [91], and Q is the quality factor of the microcantilever. Eq. (6) highlights the implicit relationship between amplitude reduction and tip-sample interactions. In particular, the amplitude A appears both on the left-hand side and on the right-hand side (through the E_{ts} and V_{ts} terms) of Eq. (6).

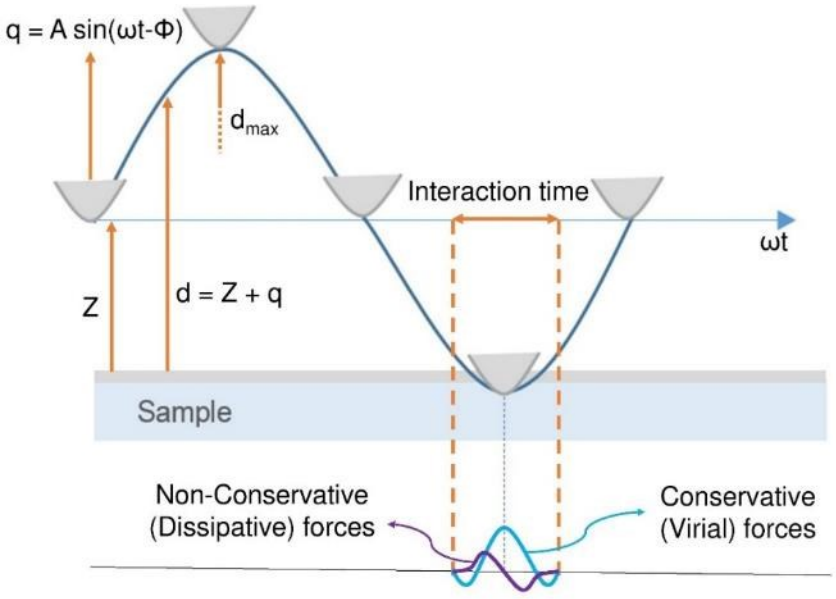

Figure 4. A schematic of an oscillating tip with tip-sample dissipative and conservative forces. $d\,(\mathrm{nm})$ is the tip-sample gap and $Z\,(\mathrm{nm})$ is the distance between the unperturbed microcantilever tip and the sample. The average of interaction force history during approach and retraction is the conservative part of interaction since it depends on the instantaneous tip-sample gap d and contributes to the Virial, while the difference of the approach and retraction force history during a cycle is the non-conservative part of the interaction and contributes to the energy dissipation.

We propose an algorithm for using Eq. (6) to find the Z-distance for each desired/observed A^{ratio} and thus predict the AM-AFM observables and surface deformation and force history as a function of A^{ratio}. As illustrated in Figure 5, $A^{ratio}_{current}$ is the desired/observed amplitude ratio, A^{ratio}_{new} is the computed amplitude ratio, tol is the tolerance band, dZ (nm) is a small decrement in Z and ΔZ is the initial guess for the Z piezo increment. The value dZ is updated at each iteration to facilitate faster convergence. In the proposed approach, the procedure starts with an initially guessed Z-distance value, which is adjusted (increased /decreased) such that the A^{ratio} obtained by computing E_{ts} and V_{ts} using Attard's method and inserting into the right-hand side of Eq. (3) matches the desired A^{ratio} on the left-hand side of Eq. (3), within tol, the defined tolerance. When the difference between the computed and desired A^{ratio} falls within tol, all observables like Z, energy dissipation, virial, indentation, amplitude, tip-sample force history, sample deformation history are recorded for the specific A^{ratio}. Additionally, the phase lag ϕ can be calculated for each desired A^{ratio} as follows:

$$\tan\phi = \frac{\frac{1}{Q} + \frac{E_{ts}(A,Z)}{\pi k A^2}}{\frac{-2V_{ts}(A,Z)}{kA^2}}. \tag{7}$$

After meeting the tolerance criteria for a given A^{ratio}, the algorithm goes to the next A^{ratio} in the range. The A^{ratio} range considered in the flowchart (Figure 5) is between A^{ratio}_{max} and A^{ratio}_{min} with ΔA^{ratio} steps. The advantage of the above algorithm is that it allows for the computation of the amplitude/phase/energy dissipation as a function of A^{ratio} without time-domain simulations of nonlinear governing equations of AFM microcantilever dynamics as in VEDA [77].

The described algorithm (Figure 5) thus only needs the fast computation of E_{ts} and V_{ts} using Attard's model [2, 78-81] for tip oscillation amplitudes A and Z distances for which it is called to execute. The underlying principle of Attard's model is highlighted in Figure 6, where an axisymmetric rigid tip is shown in close proximity to the sample surface. The radial coordinate r measures the radial distance along the undeformed surface from the projected location of the center of the tip. $h_0(r,t)$ is the gap between the tip and the undeformed surface. Specifically, when called by the proposed algorithm (Figure 5), with a specific A, Z, and ω value, $h_0(r,t)$ takes the following explicit time-dependent form:

$$h_0(r,t) = \left(1 + \frac{r^2}{2R}\right)\left(Z + A\sin(\omega t)\right), \tag{8}$$

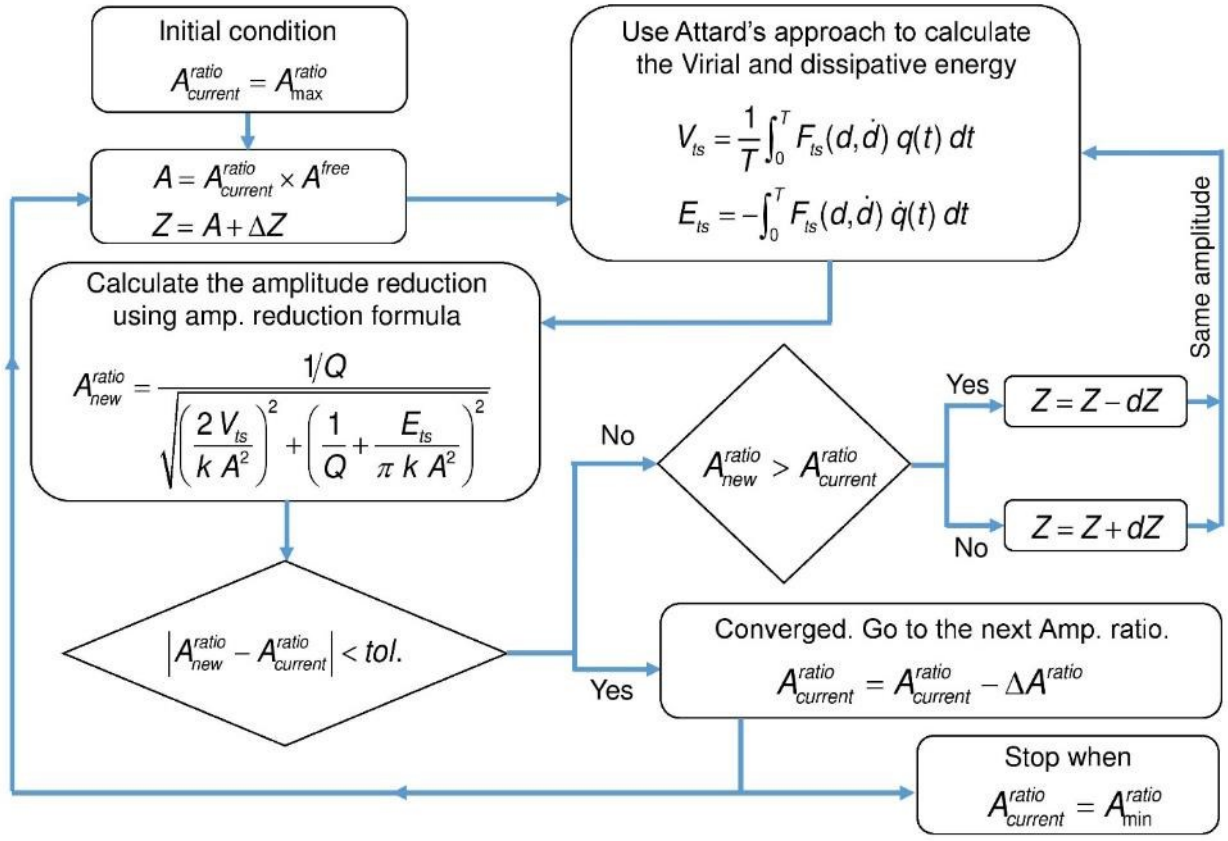

Figure 5. The proposed algorithm for predicting instrument observables by embedding Attard's model into the AM- AFM amplitude reduction formula.

Furthermore, $u(r,t)$ is the vertical displacement (deformation) of the sample, $h(r,t) = h_0(r,t) - u(r,t)$ is the gap profile between the tip and the deformed surface, and the illustrated nodes (Figure 6) show the spatial discretization on the surface of the sample. The spatial discretization is referred to by i/j indices. The Lennard-Jones pressure accounts for the surface force between the tip and the sample:

$$p(h(r,t)) = \frac{H}{6\pi h(r,t)^3}\left(\frac{z_0^6}{h(r,t)^6} - 1\right) = \frac{H}{6\pi (h_0(r,t) - u(r,t))^3}\left(\frac{z_0^6}{(h_0(r,t) - u(r,t))^6} - 1\right), \qquad (9)$$

where H is the Hamaker constant and z_0 is the equilibrium distance. Alternative surface force models can also be included in the approach. The viscoelasticity of the sample is incorporated by the creep compliance of a standard linear solid (three-element) viscoelastic model [92], however, the approach can in principle include any linear viscoelastic constitutive relation:

$$\frac{1}{E(t)} = \frac{1}{E_\infty} + \frac{E_\infty - E_0}{E_\infty E_0} e^{-t/\tau}, \tag{10}$$

$$\frac{1}{E(t)} = \frac{1-\nu^2}{E_s(t)}, \tag{11}$$

where, $E_s(t)$ and $E(t)$ are the time-dependent Young modulus and reduced elastic modulus of the sample as defined in Eq. (11), respectively, E_0 and E_∞ are short and long-time reduced Young's modulus of the sample ($E_0 > E_\infty$), and τ is the relaxation time for the creep compliance function. The rate of the change of the sample surface deformation and its deformation is correlated by [2]:

$$\dot{u}(r,t) = -\frac{1}{\tau}\left(u(r,t) - u_\infty(r,t)\right) - \frac{1}{E_0}\int_0^\infty k(r,s)\,\dot{p}(h(s,t))\,s\,ds, \tag{12}$$

where, $\dot{u}$ and $\dot{p}$ are time derivatives of sample deformation and the pressure, respectively. The longtime static deformation (u_∞) and $k(r,s)$ are given by

$$u_\infty(r,t) = -\frac{1}{E_\infty}\int_0^\infty k(r,s)p(h(s,t))\,s\,ds, \tag{13}$$

$$k(r,s) = \begin{cases} \frac{4}{\pi r} K\left(s^2/r^2\right) & s < r \\ \frac{4}{\pi s} K\left(r^2/s^2\right) & s > r \end{cases} \tag{14}$$

where, K is the complete elliptical integral of the first kind. Equations (12) and (13) can be spatially discretized by trapezoidal integration as follows:

$$\dot{u}(r_i,t) = -\frac{1}{E_0}\sum_{j=1}^{N}\dot{p}(h(r_j,t))\,\Delta r_j\,k(r_i,r_j)\,r_j - \frac{1}{\tau}(u(r_i,t) - u_\infty(r_i,t)), \tag{15}$$

$$u_\infty(r_i,t) = -\frac{1}{E_\infty}\sum_{j=1}^{N}p(h(r_j,t))\,\Delta r_j\,k(r_i,r_j)\,r_j \tag{16}$$

where, $\Delta r_j = r_j - r_{j-1}$ and N is the number of radial nodes. As can be seen, $\dot{u}$ appears explicitly and implicitly (through $\dot{p}(h)$) on both sides of Eq. (15). To solve this equation, Attard [2, 79] used a slow iterative approach in which a value of $\dot{u}$ is guessed at each time step and refined iteratively until the left and right-hand sides of Eq. (15) are within a defined tolerance.

It is important to emphasize that Attard's model represents the exact solution to the field equations of 3D elasticity and through the correspondence principle allows for any linear

viscoelastic constitutive relationship to be included. Interested readers are referred to Attard's papers for a complete theory of the employed model [2, 78-80].

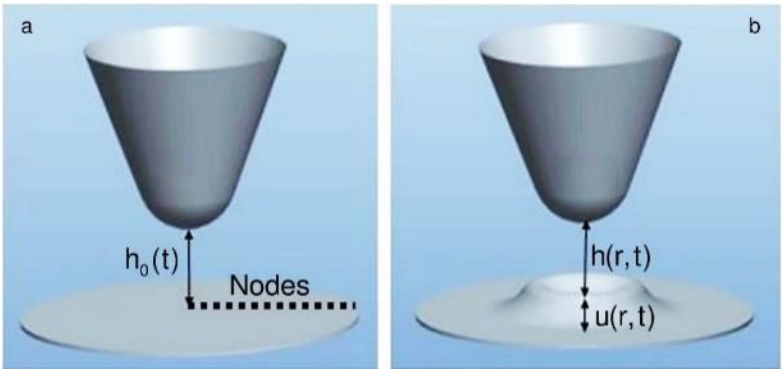

Figure 6. Attard's viscoelastic model assumes an axisymmetric rigid tip interacting with a flat polymer surface. In order to model the viscoelasticity of the sample, creep compliance of a standard three-element viscoelastic model is utilized (Eq. (10)) [92] in conjunction with arbitrary surface force models. (a) and (b) show the un-deformed and deformed sample, respectively.

In contrast to Attard's algorithm for solving these equations, we propose to take all the explicit $\dot{u}$ terms in Eq. (15) to the left side as follows:

$$\dot{u}(r_i,t) = J_{ij}^{-1}\, b_i \tag{17}$$

$$J_{ij} = \frac{1}{E_0}\Big(p'(h(r_j,t))\,\Delta r_j\, k(r_i,r_j)\Big) - \delta_{ij} \tag{18}$$

$$b_i = \frac{1}{E_0}\sum_{j=1}^{N} p'(h(r_j,t))\,\dot{h}_0(r_j,t)\,\Delta r_j\, k(r_i,r_j)\, r_j + \frac{1}{\tau}(u(r_i,t) - u_\infty(r_i,t)) \tag{19}$$

$$p'(h(r_j,t)) = \frac{dp}{dh} = \frac{H}{2\pi(h_0(r_j,t) - u(r_j,t))^4}\left(1 - \frac{3z_0^6}{(h_0(r_j,t) - u(r_j,t))^6}\right) \tag{20}$$

where, δ_{ij} is the Kronecker delta. Eq. (17) is thus a large set of nonlinear coupled ordinary differential equations with explicit time-dependent forcing through the $h_0(r_j,t)$ term. This is solved by discretizing time and evaluating the left-hand side of Eq. (14) at each time step and using the deformation velocities at the nodes to step forward to the new position of the deformed surface. The code is implemented in both FORTRAN for future deployment in VEDA and MATLAB. In both codes, the time is discretized per uniform increments/decrements of the tip-sample gap (d) and the surface is spatially discretized into nodes with equal radial increments. The selection of the appropriate number of temporal/radial discretization points is made through numerical studies

to ensure that the solution is converged, and the predictions are independent of the number of discretization points. This allows for the explicit computation of $u(r_i, t)$ and consequently $h(r_i, t)$ and thus $p(h(r_i, t))$. With this computation in place, it is easy to determine the tip-sample interaction force history as follows:

$$F_{ts}(t_k) = 2\pi \Delta r \sum_{j=1}^{N} p(h(r_j, t_k))\, r_j . \tag{21}$$

Once the tip-sample force history is calculated during an oscillation cycle for a specific Z and A value, the result can be plugged into the Eq. (5) and Eq. (6) to compute $E_{ts}(Z, A)$ and $V_{ts}(Z, A)$, which is needed to determine the Z value required to achieve a certain A and ϕ. Once this is computed as described in Figure 5, all the relevant dAFM observables such as sample deformation/relaxation history per cycle, energy dissipation, force history, virial, phase lag, etc., can be determined at the desired A^{ratio}.

2.3 Verification

By directly solving the set of ODE's in the time domain rather than an iterative solver as in Attard's original work, the present approach is nearly an order of magnitude faster than the original computational approach presented by Attard [78]. We present here the computational verification and validation of the proposed approach.

In order to verify the accelerated computational approach presented, we compare the predicted $F\text{-}d$ histories for a prescribed triangular tip motion with the ones in Attard's original work (Figure 7) [78]. These results are also compared with simulations performed using identical parameters but using Ting's viscoelastic model of contact mechanics without surface forces, which is calculated by using the VEDA set of tools [77]. The number of temporal discretization points is 10^4, the simulations are performed for an effective tip radius of $10\,\mu m$, and 600 radial nodes are used within a radius of 500 nm of the surface to ensure convergence of the solution. The characteristic relaxation time for the creep function is $1\,ms$, the short-time Young's modulus of the sample (E_0) is $10\,GPa$, and the long-time Young's modulus of the sample (E_∞) is $1\,GPa$. For Attard's viscoelastic model, the Hamaker constant H is $10^{-19}\,J$, the equilibrium position z_0 is $0.5\,nm$. A triangular oscillation with amplitude $20\,nm$ with three different tip velocities are

prescribed into the model and h_0 oscillates between $10\,\text{nm}$ and $-10\,\text{nm}$. The predictions of the developed code predict excellently the ones presented by Attard [78] and are in close agreement with Ting's model prediction during the approach phase but not during the retraction phase. This result is consistent with the lack of surface forces in Ting's model.

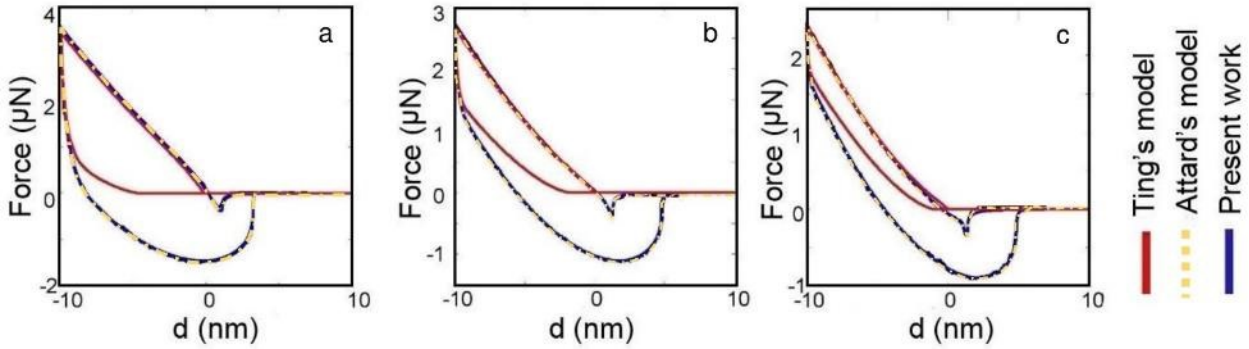

Figure 7. Attard's viscoelastic model results [78], Ting's analytical viscoelastic model [77], and the code developed in the present work are compared with a prescribed triangular motion time profile of a rigid spherical tip. The triangular drive velocities are (a): $\pm 5\,\mu\text{m/s}$, (b): $\pm 2\,\mu\text{m/s}$, and (c): $\pm 1\,\mu\text{m/s}$. Tip radius is $10\,\mu\text{m}$ and the other material parameters used are identical to the ones used by Attard to facilitate comparison [78].

Next, we validated the proposed algorithm (Figure 8) for computing the dynamic approach curves when using Attard's model for tip-sample interactions. AMAC (Amplitude Modulated Approach Curves) is an already validated tool on VEDA, which includes full microcantilever dynamics and makes reliable predictions for tapping mode AFM [77]. This tool can accurately use Ting's model (but not Attard's) as the tip-sample interaction model, which we choose for the validation of this algorithm. Therefore, the comparison between the instrument observables predicted by computing force-distance histories and embedding them within the AM-AFM amplitude reduction formula (Figure 5) and the ones computed directly from the AMAC tool help us to ensure the validity of the proposed algorithm. As illustrated in Figure 8, the A, ϕ, V_{ts}, E_{ts} graphs show an excellent match for both elastomer and polycarbonate material properties. Since polycarbonate is stiffer than the elastomer, the energy dissipation and virial values for the elastomer are greater than the ones of polycarbonate. The parameter values used for the polymers in these simulations are listed in Table 2.

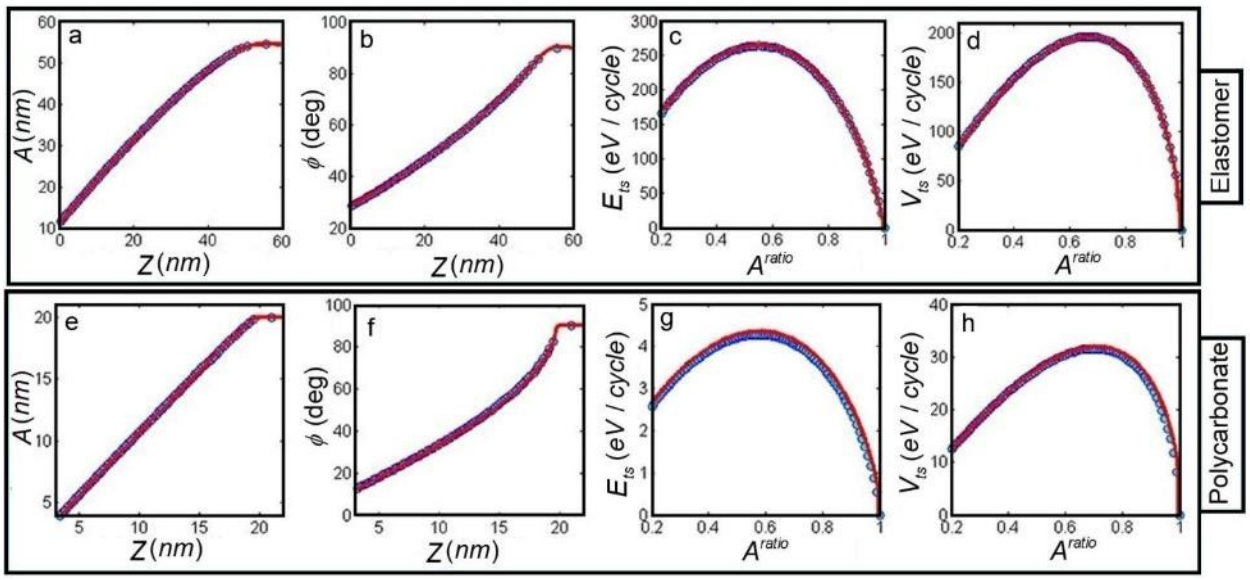

Figure 8. A comparison between the dynamic approach curves results predicted by using the present algorithm (Figure 5) and the ones from the AMAC tool which includes explicit microcantilever dynamics for elastomer (upper row), and polycarbonate (lower row). The blue circles are from the proposed algorithm and the red solid lines are the VEDA-AMAC tool's outputs. The used material property data for these simulations are listed in Table 2. The equivalent microcantilever properties are: $K = 28\ \mathrm{N/m}$ and $Q = 542$, and the oscillation period is 3×10^{-6} s.

Table 2. The parameter values used for the simulations in verification and computational results sections.

	τ	E_0	E_∞	H	z_0	A_0
	sec	GPa	GPa	J	nm	nm
Elastomer	5.47×10^{-8}	0.143	0.029	7.99×10^{-20}	0.6	60
Polycarbonate	6.56×10^{-8}	2.960	2.08	8.82×10^{-20}	0.3	20

2.4 Computational results

In order to visualize the physics of the tip-sample interaction during a single cycle, a simulation is carried out for a prescribed sinusoidal tip motion interacting with an elastomer sample (Figure 9). The elastomer sample is represented by a standard linear viscoelastic solid (three-element) model with the data provided in Table 2. The complete set of parameters used for this simulation is provided in the caption of the figure. The number of temporal discretization

points is 10^5, the simulations are performed for an effective tip radius of $100\,\text{nm}$, and 100 radial nodes are used inside a radius of $50\,\text{nm}$ on the surface to ensure convergence of the solution. Figure 9 shows the force history during one cycle as a function of d and $\dot{d}$ (inset). These force histories clearly show the dependence of hysteresis and adhesion on both d and $\dot{d}$. The series of tip-sample geometries corresponding to 12 instants during the force history (Figure 9b) are captured from the output video of the code. During the tip approach, the material's surface slightly deforms upwards from its initial flat state, and then snaps on to the tip, and then deforms downwards with the tip movement. However, it gradually peels away from the tip during the retraction process, until a final detachment occurs. After the detachment, the surface continues to relax until it returns to the initial state. These surface instabilities are in line with predictions by Attard's model [93, 94]. The cycle then repeats at every tap, unless the sample has not fully relaxed prior to a subsequent tap. This latter condition has not been explored in the present work where we assume the sample eventually fully relaxes prior to a subsequent tap. It is worth mentioning that the phenomena that are captured by the model and demonstrated in this figure are not fully accounted for by any of the classical models such as Hertz, JKR (Johnson, Kendall, and Roberts), DMT, or Ting's model.

In order to study the effect of diverse relaxation modes of polymers[92] on AM-AFM observables, a set of the relaxation times τ ranging between 2.9×10^{-6} and 2.8×10^{-9} (s) is used in the developed code as prescribed in Figure 5, and their effect on the outputs of the model such as V_{ts}, E_{ts}, F_{ts}, and indentation depth vs. A^{ratio} is investigated. The relaxation time τ determines how fast the instantaneous Young's modulus of the sample changes from E_0 to E_∞. All the other parameters except τ are identical for all the simulations.

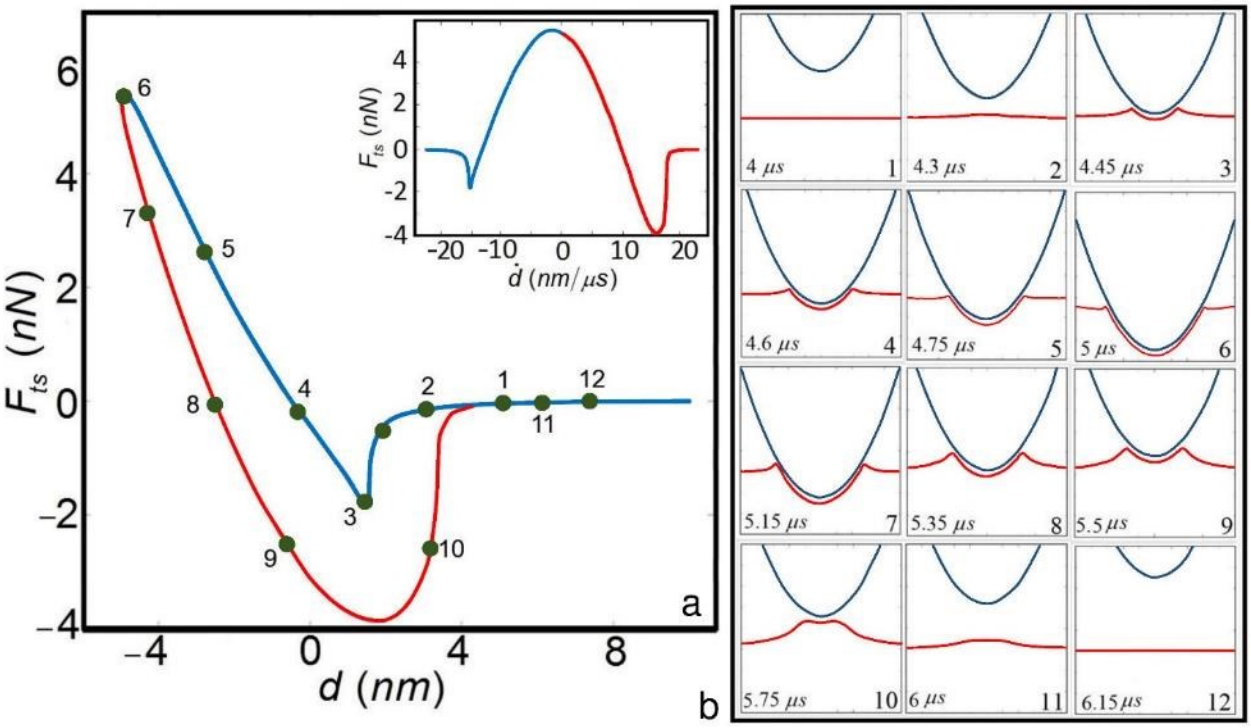

Figure 9. The interaction between a rigid axisymmetric tip and the elastomer sample surface is computed using the approach of the present work. The viscoelasticity of the elastomer is modeled by using a standard linear solid (SLS) model with the data provided in Table 2. The tip travels through a sinusoidal wave with $100\ \text{kHz}$ frequency and $Z = 45\ \text{nm}$. The oscillation amplitude is $50\ \text{nm}$ and tip radius $= 100\ \text{nm}$. In (a) the $F - d$ and the $F - \dot{d}$ history (inset) are graphed. In (b), the deformation history during a sequence of time instants labeled 1-12 is graphed.

As illustrated in Figure 10, energy dissipation values are significantly affected by τ. E_{ts} reaches its maximal values at specific relaxation times. Figure 10a also demonstrates an additional key result. The A^{ratio} at which maximum energy dissipation occurs [95] is highly dependent on τ. However, as depicted in Figure 10b, contrarily, the V_{ts} does not vary substantially when τ is changed.

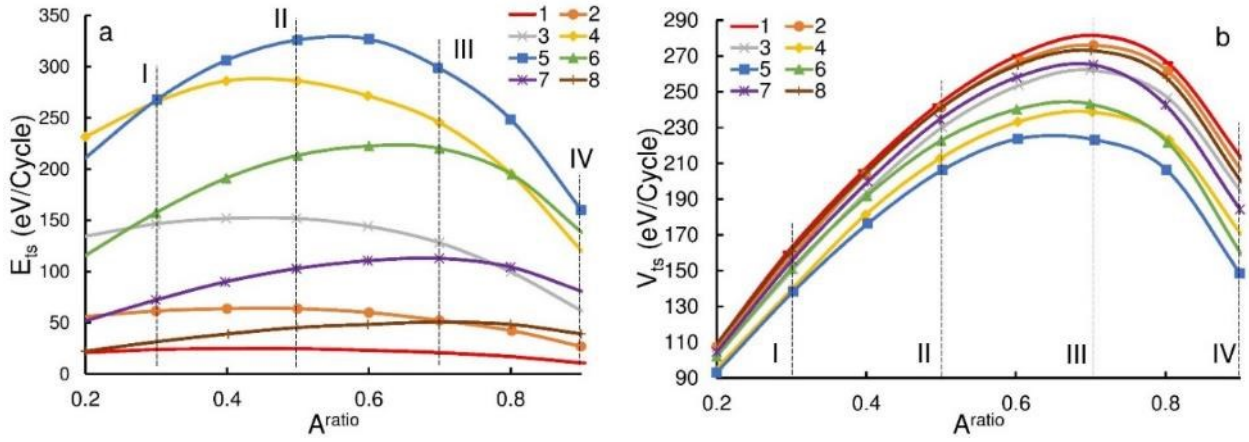

Figure 10. (a) Energy dissipation (E_{ts}) and (b) Virial (V_{ts}) vs. setpoint ratio (A^{ratio}) for a set of relaxation time (τ) values: 1: $2.9\,\mu s$, 2: $1.1\,\mu s$, 3: $0.40\,\mu s$, 4: $0.15\,\mu s$, 5: $54.7\,ns$, 6: $20.3\,ns$, 7: $7.6\,ns$, and 8: $2.8\,ns$. The Lennard-Jones parameters for all simulations are: $H = 8\times10^{-20}$ J, and $Z_0 = 0.6$ nm, and additional material properties are provided in Table 2 for the elastomer. The oscillation period is 3×10^{-6} s, the equivalent microcantilever properties are: $K = 28$ N/m and $Q = 542$, and the tip radius is 15 nm. The vertical lines marked by Roman numerals are discussed in Figure 12.

It is instructive to examine in Figure 11a, the F-d histories acquired as a part of the simulations presented in Figure 10 for a fixed A^{ratio} as the τ is changed in the stated range above. In Figure 11a, the force loops show minimal hysteresis when τ is small compared with the contact time, reach a maximum hysteresis when for an intermediate value of τ, and the hysteresis vanishes when τ is very large. To be more quantitative, we estimate the contact (interaction) time in each F-d history in Figure 11a from the time $A^{ratio} = 0.5$ spent in the repulsive interaction regime. Then we plot the corresponding indentation, E_{ts}, and V_{ts} as a function of τ non-dimensionalized by the contact time in Figure 11b, all at $A^{ratio} = 0.5$. Figure 11b illustrates that the indentation depth increases with decreasing τ. For τ <<contact time, the material has enough time to completely relax during the interaction time and therefore the modulus behaves more like E_∞ during both approach and retraction leading to a larger indentation, and small hysteresis leading to low energy dissipation E_{ts}. Likewise, when τ >>contact time the material responds with a stiff E_0 leading to a less indentation and small hysteresis leading to low energy dissipation E_{ts}. Figure 11b shows that E_{ts} is maximized when τ/contact time ~0.01-0.1. Put another way, E_{ts} is maximized

when the ratio of creep (retardation) time ($=\left(E_0/E_\infty\right)\times\tau$) to contact time $\sim 0.05-0.5$. Thus, if a polymer surface were to have many relaxation modes, those whose relaxation and creep times are $\approx 0.01-0.1$ and $\approx 0.05-0.5$ of the contact time, respectively, are likely to contribute most to the energy dissipation. In this sense, the energy dissipated in AM-AFM on a viscoelastic sample may be considered as a "narrowband filter" for capturing the effect of a narrow range of polymer relaxation times.

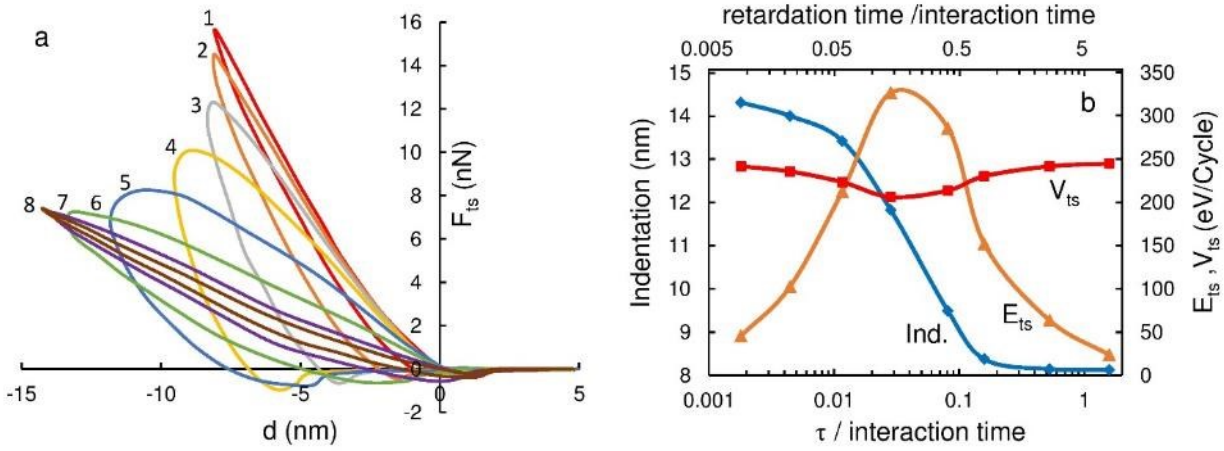

Figure 11. $F-d$ histories and indentation depth predictions at $A^{ratio}=0.5$ for a range of relaxation times (τ) are demonstrated. The τ values and other simulation parameters are identical to the ones in Figure 10 (b). The indentation depth, E_{ts}, and V_{ts} corresponding to the F-d histories in (a) are graphed as a function of τ non-dimensionalized by the tip-sample interaction time. Note that each of the cycles 1-8 in (a) has a different interaction time.

Figure 12 illustrates V_{ts} and E_{ts} vs. τ for four selected set point ratios: 0.3, 0.5, 0.7, and 0.9. These are extracted from the same set of simulations as in Figure 10 and are shown by vertical dashed lines marked by Roman numerals. The results show that while E_{ts} varies more significantly than V_{ts} with τ, E_{ts} is maximized and V_{ts} is minimized when the creep time is $\approx 0.05-0.5$ of the contact time.

The surface pressure parameters (H, z_0) that define the resultant surface adhesion, are also expected to play a role in the observed energy dissipation and hysteresis. In order to assess the sensitivity of E_{ts} vs A^{ratio} to these parameters, a range of H values between

$2\times10^{-19}-10\times10^{-19}$ J and a range of z_0 values between $0.5-0.8$nm are used in the model. For smaller values of z_0 chosen in this range, surface instabilities are observed with increased hysteresis. However, those simulations are also associated with computational instabilities. The range of z_0 chosen in these simulations is both comparable to prior computational results and appropriate for small roughness polymer surfaces [96]. As shown in Figure 13, within the range of chosen surface pressure parameters, E_{ts} increases as H is increased or as z_0 is decreased. This result is in line with the expectation that energy dissipation should increase with an increase in surface forces.

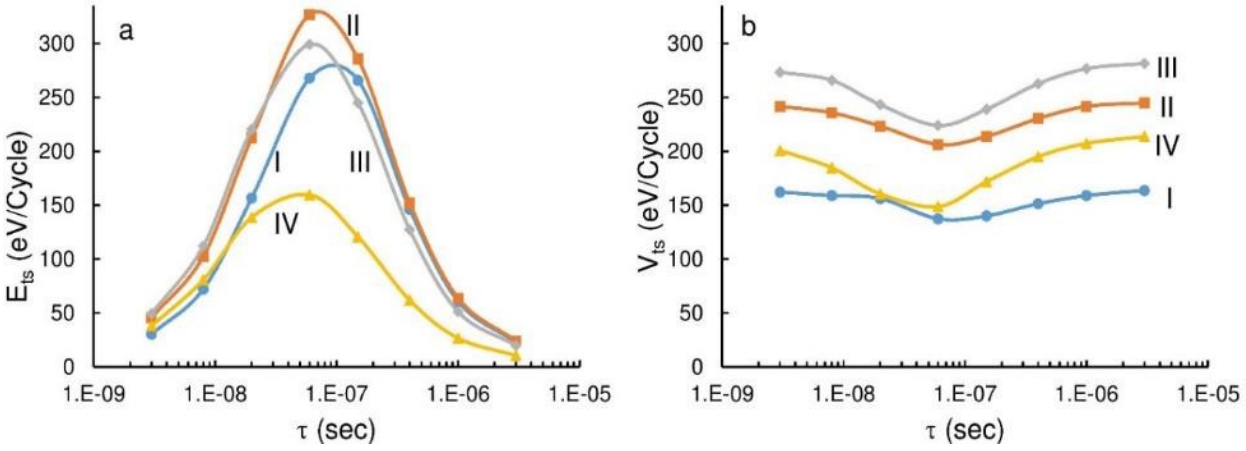

Figure 12. (a) Energy dissipation (E_{ts}) vs. relaxation time (τ) and (b) Virial (V_{ts}) vs. τ for a series of $A^{ratio}=0.3, 0.5, 0.7$, and 0.9 that are specified in Figure 10 by vertical dashed lines labeled I, II, III, IV, respectively. All of the simulation parameters are identical to the ones in Figure 10.

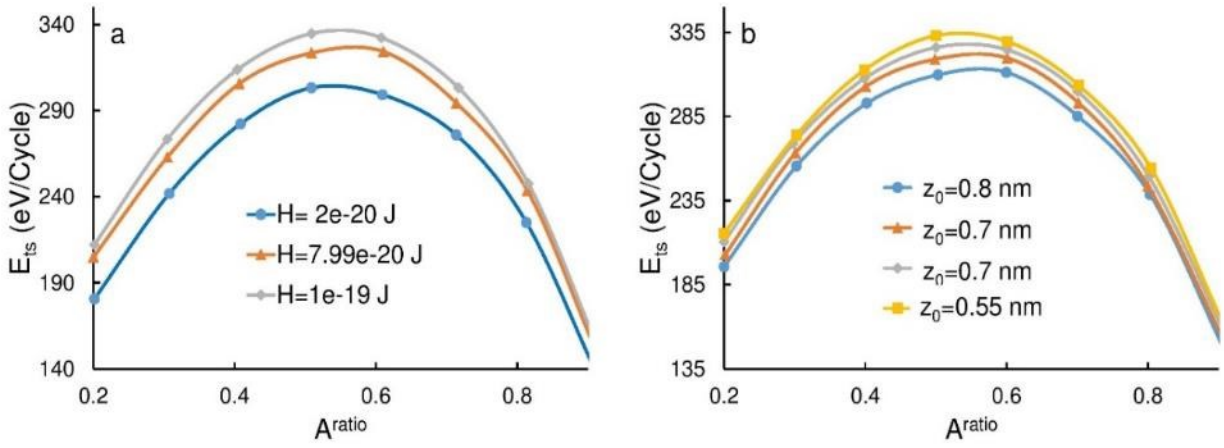

Figure 13. The Energy dissipation (E_{ts}) vs setpoint ratio (A^{ratio}) for (a) different Hamaker (H) constant values, (b) different values of the equilibrium position (z_0). For (a), $z_0 = 0.6$ nm and for (b), $H = 8\times10^{-20}$ J. The material properties are the ones recorded in Table 2 for the elastomer.

2.5 Experiments

To demonstrate how the proposed computational approach relates to experimental data acquired on polymers, a set of experiments using tapping mode (TM) or AM-AFM at 326.1 kHz, and quasi-static (QS) at 1 Hz are conducted on the surface of a three-component polymer blend sample. The sample consists of a glassy polymer, polycarbonate; a semicrystalline polymer, polypropylene; and a polyolefin-based elastomer. The full description of the employed instruments and sample preparation is provided in the methods section. A typical sample data is shown in Figure 12 that are acquired over a rectangular region with the TM microcantilever with $A^{free} = 35.9$ nm and $A^{ratio} = 0.7$. The resulting topography image (Figure 14a) shows areas of smooth PC are interspersed with areas of PP with more surface roughness. Smaller areas of elastomer are found embedded in and surrounded by PC and PP domains.

The methods and materials used to conduct experiments are described below in more details:

Instrument: All TM/AMAFM and QS measurements were made on a Bruker MultiMode 8 AFM with a Nanoscope V controller running v8.15 Nanoscope software. For the TM measurements, a Bruker TESP silicon microcantilever was used with a quality factor, spring constant, and fundamental frequency of 542, 28.0 N/m, and 326.1 kHz, respectively. These values were measured using thermal tuning of the undriven microcantilever. TM-AFM/AM-AFM

experiments are performed on a 10×5 μm rectangular region with 512 points/line resolution level and a scan rate of 0.5 Hz using two different free amplitudes (18.0 and 35.9 nm) and 9 different amplitude ratios (0.9, 0.8 … 0.1). For the TM imaging, the phase was zeroed when the microcantilever was within 100 nm of the surface for each amplitude ratio measurement. QS force curves are acquired over the same sample at 200 points (5 rows x 40 columns evenly spaced) on the same region using a Bruker TESP silicon type microcantilever whose spring constant was 21.2 N/m. Using a blind reconstruction method, the tip radius of the QS microcantilever was estimated to be 14.2 and the tip radius of the TM microcantilever was determined to be 14.0 nm.

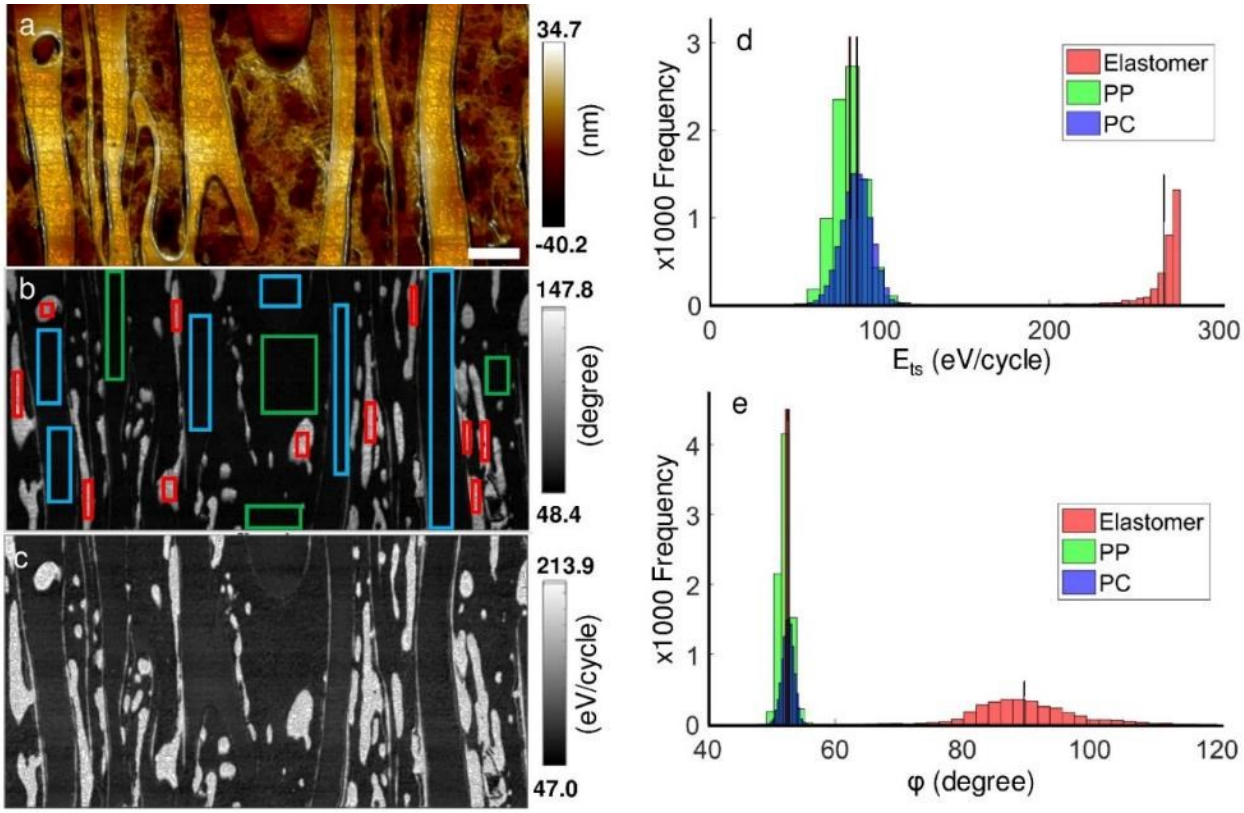

Figure 14. (a) Topography image, (b) Phase lag image, (c) Extracted energy dissipation on a three-phase blend polymer sample with $A^{ratio} = 0.7$ and $A^{free} = 35.9$ nm. (d) and (e) show histograms of the extracted energy dissipation and phase lag values acquired over the selected rectangular areas of the PC, PP, and elastomer marked in (b) with corresponding colors. The vertical bold lines shown for each histogram in (d) and (e) represent the mean value for each polymer. The scale bar is shown in (a) represents 1 μm.

Sample Preparation: The sample consists of a glassy polymer, polycarbonate (Calibre™ 302-6, Trademark of Trinseo); a semicrystalline polymer, polypropylene (Inspire™ 404, Trademark of

Braskem); and a polyolefin-based elastomer (Engage® 8003, Registered Trademark of The Dow Chemical Company). The sample was fabricated using injection-compression molding providing 2 inch x 2 inch x 1/8 inch plaques. Pieces of the plaque were removed via a punch and mounted into vice holders. Trapezoid faces were cryo milled in the plaques pieces at -120°C and then polished in a cryo-microtome at -120°C to produce block faces for AFM investigation.

The acquired phase data are converted to phase lag ϕ and adjusted so that when drive frequency equals the microcantilever's natural frequency far from the sample then $\phi = 90^{\circ}$. For these operating conditions, the AFM mostly operates in the net repulsive regime ($\phi < 90^{\circ}$, throughout the scan region) as seen in Figure 14b. The E_{ts} values (eV per tap) are extracted from the phase lag images by using the following relation [88, 89]:

$$E_{ts}(Z,A) = \frac{\pi k A A_0}{Q}\left(\sin(\phi) - A^{ratio}\right) \tag{22}$$

and mapped to the scan region as shown in Figure 14c. Histograms of E_{ts} and ϕ acquired over rectangular regions of the PP, PC, and elastomer phases are shown respectively in Figures 12 d and e.

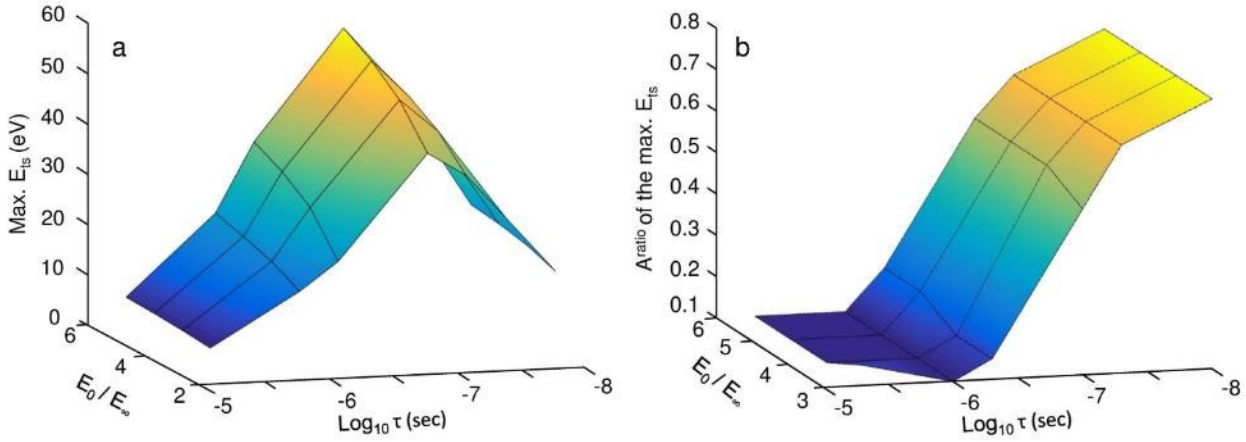

Figure 15. Maximum E_{ts} and A^{ratio} at which the maximum E_{ts} occurs plotted as a function of the relaxation time (τ) and E_0 / E_∞ ratio for PP. The employed material properties are listed in Table 3, $A^{free} = 18\,\text{nm}$, $K = 28\,\text{N/m}$, and other parameters are identical to the ones described in the experiments section.

The experimental validation of our computational approach is challenging due to uncertainties associated with the model parameters. For example, viscoelastic bulk properties can

be measured using Dynamic Mechanical Analysis (DMA). However, their correlation with viscoelastic surface properties measured using AFM methods remains an active topic of research. Specifically, with moderate to large net indentation, contact resonance (CR) method-based AFM studies have reported local elasticity values consistent with bulk DMA [97, 98]. However, in AM-AFM in which gentler forces are used, indentations are much smaller, and the local properties may be more influenced by surface effects [99-105]. Moreover, the sample under consideration features significant interphase effects due to the mixture of small volumes of the three phases. Even if the AFM measures properties far from interphase regions on the sample surface, there can be sub-surface interphases that influence surface AFM measurements. Last, but not least, the surface force parameters z_0 and H are very hard to estimate experimentally. While H can be approximated using theory, there is no clearly accepted method to approximate z_0 for the specific sample.

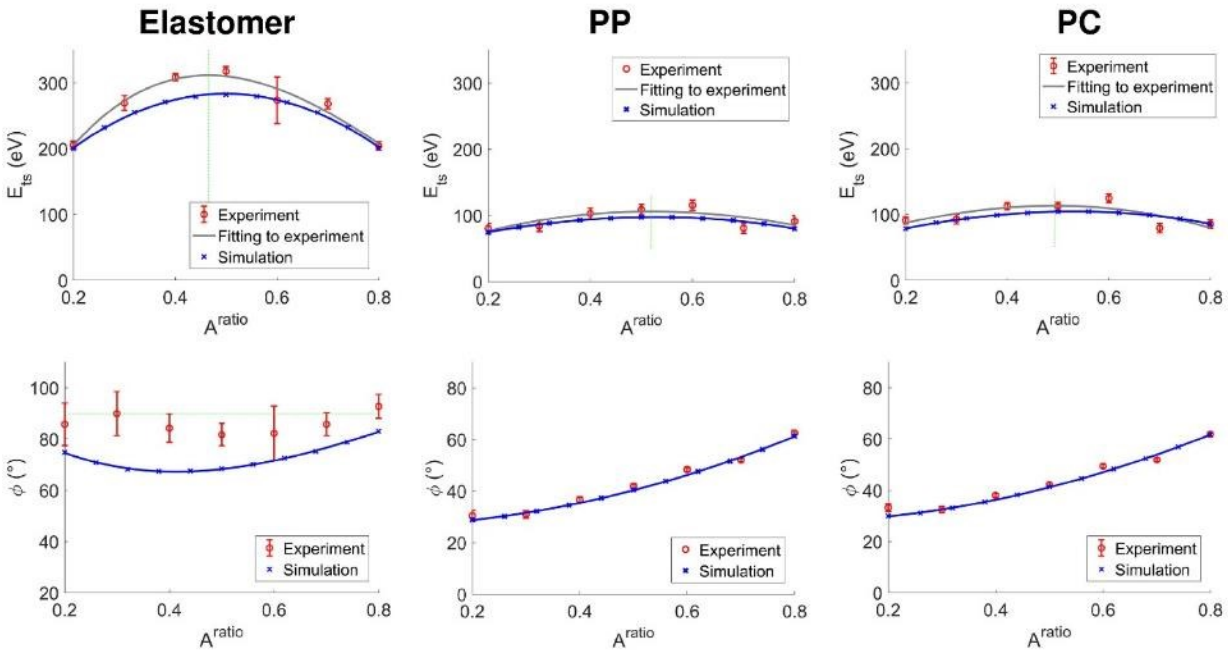

Figure 16. Comparison between theory and experiment for the three phases following calibration of τ and E_0 to best match the amount E_{ts} and the A^{ratio} at which it occurs in the experimental data acquired with $A^{free} = 35.9$ nm. A cubic polynomial is fitted to theory and experimental data to facilitate the identification of the maximum E_{ts} location and magnitude. To help to clarify the regime of the oscillation, the 90-degree phase lag is marked by a green horizontal dashed line.

We chose to adopt the following strategy for estimating parameters for subsequent experimental validation:

1. We estimate the Hamaker constants between native Si oxide on the tip surface and the specific polymer using Lifshitz theory[96]. z_0 is chosen within the range of prior works[96] and is made as small as possible to enable stable computation.

2. We use the QS force curves acquired on each of the three phases to estimate the long-timescale elastic modulus E_∞ using Hertz contact mechanics. This is a reasonable approach since the QS curves are performed at extremely slow rates (1Hz) and the quantification of uncertainties in measuring surface elastic modulus using standard force-distance curves is well understood [106].

3. We then estimate E_0 and τ by fitting these numbers to match various features of the E_{ts} vs A^{ratio} curve acquired on the three polymer phases with $A^{free} = 35.9\,\text{nm}$. Specifically, for each of the polymer domains:

   a. τ is adjusted until the A^{ratio} at which maximum energy dissipation occurs in simulations results matches within 10% the one found in the experiment. This is based on a key theoretical prediction that the A^{ratio} at which the maximum E_{ts} energy dissipation occurs is mostly affected by τ (Figure 15b) and to a much lesser extent by E_0 / E_∞. As an initial starting guess τ is chosen to be 1% of the microcantilever oscillation period.

   b. E_0 value is increased from E_∞ so that the maximum energy dissipation (E_{ts}) of the model matches within 10% of the peak value of the fitted curve.

   c. τ is again tuned to ensure that the A^{ratio} at which maximum energy dissipation occurs in simulations remains within 10% of the one in the experiment.

The estimated values for the material properties using this approach are provided in Table 3. The resulting computational and experimental E_{ts} vs A^{ratio} are compared in Figure 16. As can be seen, the computational results using material properties estimated with the experimental data set at $A^{free} = 35.9\,\text{nm}$ matches the experimental results within 5% across a wide range of A^{ratio}. These estimated material properties are in line with the results provided by others[107, 108].

Using the material properties estimated using the calibration data (Table 3) we validate the computational approach by comparing predictions with experimental data for $A^{free} = 18.0$ nm. As illustrated in Figure 17, the predicted and measured E_{ts} are within 10% over a wide range of A^{ratio} for both PP and Elastomer. The good match obtained on the elastomer is particularly interesting since for $A^{free} = 18.0$ nm most of the approach curve is in the attractive regime of oscillation.

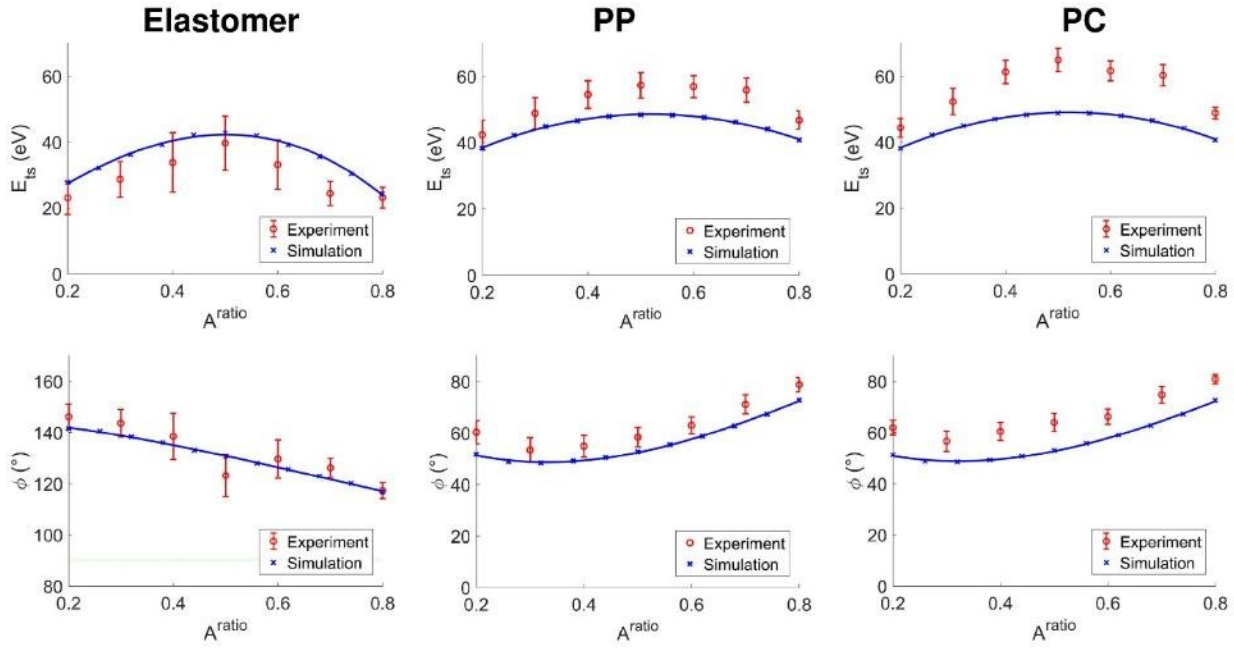

Figure 17. Comparison of computational predictions and experimental results for $A^{free} = 18$ nm on the three polymer phases. The material property data used for the computation (Table 2) are based on quasi-static force curves, theoretical estimates, and with τ and E_0 calibrated from similar data acquired for $A^{free} = 35.9$ nm (Figure 16). The observed discrepancy between simulation and experimental results are less than 11%, 11%, and 22% for Elastomer, PP, and PC, respectively.

However, the computational approach underpredicts actual energy dissipation by over 20% for PC. In contrast with the other polymer phases in the blend, PC is hydrophilic, so that under the ambient conditions of the experiment, water bridges may form leading to capillary forces and significant additional energy dissipation that are unaccounted for in the present approach[109-111]. To estimate the influence of capillary forces on the total observed energy dissipation, a set of Peak Force Tapping experiments were conducted under ambient and dry nitrogen flushed conditions.

Based on the observed results, the hysteresis of a single force cycle at ambient condition is about 8%, 7%, and 50% higher for PP, elastomer, and PC respectively under ambient conditions compared to under dry nitrogen. Thus, capillary forces are likely to contribute more to AM-AFM under ambient conditions on PC than on PP or elastomer and might have resulted in unrealistic predictions for PC.

Table 3. The material property estimations/extracted from the set of experiments with $A^{free} = 35.9$ nm and used for subsequent validation with another set of experiments with $A^{free} = 18$ nm on the three blend polymer sample.

	τ	E_0	E_∞	H	z_0
	sec	GPa	GPa	J	nm
Elastomer	1.05×10^{-8}	2.5	0.115	8×10^{-20}	0.26
Polypropylene	2.18×10^{-8}	9.01	1.64	7.6×10^{-20}	0.19
Polycarbonate	4.5×10^{-9}	110	3.7	8.8×10^{-20}	0.19

Finally, it is worth mentioning that there is a potential bi-stability between attractive and repulsive regimes of oscillation in AM-AFM[9, 112, 113]. Under the free oscillation amplitudes considered in these simulations, the tip either remained exclusively in the attractive (for example, on the elastomer in Figure 17) or repulsive regime of oscillation in the range of setpoint amplitudes considered. If there is an initial attractive regime, the algorithm tracks that solution until that solution bifurcates and the algorithm jumps to the repulsive regime as the setpoint is decreased.

2.6 Conclusions

Understanding dAFM on polymers needs computational approaches in which the relevant physics of the interactions are considered in a self-consistent manner. By accelerating Attard's model computations and embedding it within dAFM amplitude reduction formulas it is possible to efficiently compute key dAFM observables such as surface deformation history, indentations, energy dissipation, phase, etc. as a function of the amplitude ratio. This allows the inclusion of arbitrary surface forces and linear 3D viscoelasticity in a self-consistent manner in such simulations, representing a significant advance in computational AFM on polymers. This method

alleviates the issues with the artifacts arising from the use of ad hoc viscoelastic contact mechanics models. The code and algorithm have been validated against prior results and other reliable codes. Experimental data on energy dissipation in TM-AFM/AM-AFM for different free amplitudes and amplitude ratios are presented on a three-polymer blend consisting of well-dispersed phases of polypropylene, polycarbonate, and elastomer. An approach to experimental validation of computational results is presented using TM-AFM data on a blend of PP-elastomer-PC. The computational and experimental approaches presented in this work clarify the role of surface forces and polymer relaxation times on the phase lag, energy dissipation, and surface deformation history. Such approaches are expected to aid ongoing efforts to interpret dAFM observables on polymers in terms of quantitative physical properties.

3. DISCRIMINATION OF ADHESION AND VISCOELASTICITY FROM NANOSCALE MAPS OF POLYMER SURFACES USING BIMODAL ATOMIC FORCE MICROSCOPY

The simultaneous excitation and measurement of two eigenmodes in bimodal atomic force microscopy (AFM) during sub-micron scale surface imaging augments the number of observables at each pixel of the image compared to the normal tapping mode. However, a comprehensive connection between the bimodal AFM observables and the surface adhesive and viscoelastic properties of polymer samples remains elusive. To address this gap, we first propose an algorithm that systematically accommodates surface forces and linearly viscoelastic three-dimensional deformation computed via Attard's model into the bimodal AFM framework. The proposed algorithm simultaneously satisfies the amplitude reduction formulas for both resonant eigenmodes and enables the rigorous prediction and interpretation of bimodal AFM observables with a first-principles approach. The dependence of bimodal observables on local adhesion and standard linear solid (SLS) constitutive parameters as well as operating conditions are predicted. Secondly, we present an inverse method to predict quantitatively the local adhesion and SLS viscoelastic parameters from bimodal data acquired on a heterogeneous sample. We demonstrate the method experimentally using bimodal AFM on polystyrene-low density polyethylene (PS-LDPE) polymer blend. This inverse method enables the quantitative discrimination of adhesion and viscoelastic properties from bimodal maps of such samples and opens the door for advanced computational interaction models to be used to quantify local nanomechanical properties of adhesive, viscoelastic materials in bimodal AFM.

3.1 Introduction

The continuing need for sub-micron scale compositional imaging of complex material surfaces has led to the increased use of multi-frequency AFM methods. Bimodal AFM is a popular subset of multi-frequency AFM methods[31, 43, 44, 114] that provides additional information channels beyond the traditional Amplitude-Modulated AFM (AM-AFM) or tapping mode. AM-AFM usually requires a trade-off between greater compositional contrast and greater imaging forces which may be detrimental for the fragile samples.[115] Bimodal AFM can enhance achieved compositional contrast while applying gentle imaging forces without damaging the

surface.[10, 30, 39, 46, 116, 117] In bimodal AFM the microcantilever is excited at its fundamental eigenmode frequency along with an additional small amplitude "perturbation" excitation of a higher flexural eigenmode (secondary eigenmode) (Figure 18)[31, 118]. The resulting tip motion occurs at different timescales, a slow timescale corresponding to that of the fundamental mode and a fast timescale corresponding to the higher eigenmode. The lock-in amplifiers demodulate and measure the averaged amplitude and phase of tip motion at the two excitation frequencies.

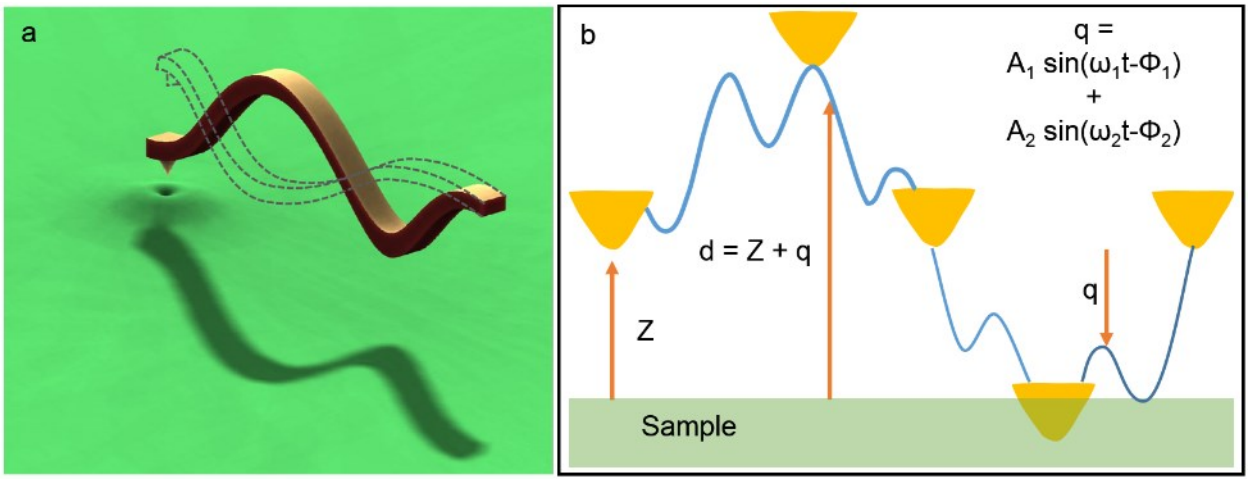

Figure 18. (a) Bimodal AFM simultaneously excites the first and a higher eigenmode of the microcantilever. (b) The resulting tip trajectory is assumed to be the sum of two harmonics whose steady-state amplitudes and phases change due to the tip-sample interaction and the microcantilever properties. In this figure ω_i is the excitation frequency and A_i and ϕ_i are the amplitude and phase lag relative to the excitation force of the i^{th} mode. Z and $d(t)$ are the distance of the microcantilever base and tip with respect to the undeformed surface level, respectively. $q(t)$ is the microcantilever tip deflection.

Bimodal AFM scans of a surface are characterized by three observables at each pixel in addition to the topography, regardless of the feedback control loops used. There are many ways to configure the feedback control loops to operate bimodal AFM [38-40]. In the most direct and commonly used configuration, the amplitude of the first mode is regulated at a fixed setpoint amplitude by adjusting the Z distance and the slow-timescale averaged phase of the fundamental mode and the amplitude and phase of the secondary mode are allowed to respond to changes in local surface properties (AM-AM)[41]. In the other common feedback loop arrangement, AM-FM, the first mode's amplitude is regulated by adjusting the Z distance while the secondary mode's phase lag and amplitude are controlled by the excitation frequency and the amplitude, respectively. in this mode which is also referred to as constant amplitude phase-locked loop (CA-PLL), the

excitation amplitude provides a measure of the tip-sample dissipation. During imaging, the slow-timescale averaged phase lag of the fundamental mode and frequency shift and dissipation of the secondary mode at each pixel is recorded. Finally, in FM-FM, two PLLs and drive modulation are used to regulate the slow-timescale averaged amplitudes and phases of both modes [38]. The three observables for these most common implementations of bimodal AFM: AM-AM, AM-FM, and FM-FM are listed in Table 4 **Error! Reference source not found.**[42]. The complexity of the required feedback loops for these bimodal AFM configurations is different and the associated control schemes become more complicated in the order they listed in Table 4.

Table 4. Three observables of the most common modalities of bimodal AFM Observable.

	#	1	2	3
	Mode #	First mode	Secondary mode	Secondary mode
Config. 1	AM-AM	Phase (ϕ_1)	Phase (ϕ_2)	Amplitude (A_2)
Config. 2	AM-FM	Phase (ϕ_1)	Freq. shift (Δf_1)	Drive (D_2)
Config. 3	FM-FM	Freq. shift (Δf_1)	Freq. shift (Δf_1)	Drive (D_2)

Quantitative bimodal AFM on polymeric surfaces requires the pixel-by-pixel inversion of three observables of the mode to extract quantitative maps of local polymer properties. Garcia et al. used an energy balance theory method to link the bimodal AM-FM observables to the material viscoelastic properties.[43, 114] The method is based on a simple Hertzian contact model for tip-sample interaction force with *ad hoc* addition of a Kelvin-Voigt viscoelastic element without any surface forces (adhesion). In another work[39], the *ad hoc* tip-sample viscoelastic model approach[114] was extended to a fractional calculus-based method to calculate the material viscoelastic properties. Proksch et al.[44] used Oliver and Pharr method[119] to link the tip-sample interaction stiffness to the contact radius. They calculated the tip-sample interaction using a Hertz model's elastic generalization and neglect the velocity-dependency of the tip-sample interaction force and long-range surface forces. All these prior-tip sample interaction models have the advantage that when combined with energy balance laws for each mode, they offer simple closed-form expressions that allow the inversion of bimodal observables to quantitative estimates of the local elastic/viscoelastic properties.

However, one of the major shortcomings of these prior inversion approaches is that they utilize simple or *ad hoc* tip-sample models which are limited in their ability to represent tip contact with soft, adhesive, and viscoelastic surfaces. Specifically: (a) *ad hoc* viscoelastic models are unable to accurately predict the tip-detachment from the surface[39, 68, 69] and are unable to predict surface relaxation post-detachment (b) they can lead to artifacts such as the presence of apparently attractive forces[1] even if the model does not contain attractive forces, and (c) they do not include attractive/adhesive forces. These shortcomings can lead to artifacts in estimated parameters, especially on soft viscoelastic adhesive samples. In one example, a bimodal map inversion based on an *ad hoc* viscoelastic model[39] led to an effective viscosity prediction for the PS domain in a PS-LDPE blend to be 4 times greater than the viscosity for the LDPE domain when measured in the same scan. This ratio of damping characteristics prediction for stiff PS, which is in the glassy state in room temperature, and soft LDPE which is in rubbery state in room temperature is not physically acceptable.

In this work, we develop an algorithm including Attard's model to link the surface properties of an adhesive and viscoelastic sample to associated AM-AM bimodal AFM observables. The algorithm has several advantages: (1) it can easily be adapted to other implementations of bimodal AFM such as AM-FM or FM-FM bimodal operation, (2) it simultaneously satisfies the amplitude reduction formulas for both excited modes in AM-AM bimodal AFM, and (3) it requires the computation of tip-surface interaction and surface deformation history which is implemented here using an accelerated computational approach[1] for Attard's model which is more than two orders of magnitude faster than the original implementation[2, 79].

We use the proposed algorithm to illustrate the dependence of the bimodal AFM observables on the properties of adhesive, viscoelastic surfaces modeled by Lennard Jones pressure and SLS viscoelastic constitutive relations. Then, we present an approach to invert the three bimodal AFM parameters using a linear surrogate model based on the forward computations carried out over a vast range of sample parameters selected by the Latin hypercube sampling method[120]. The computational surrogate model, applicable for the specific cantilever and operating conditions, then relates physical properties of the local polymer such as adhesion, long- and short-term elastic moduli, to the three AM-AM bimodal observables via a computed 3 by 3 matrix. The three observables measured at each pixel can then be converted to quantitative

estimates of these physical properties via matrix inversion at each pixel and that relates the observables to physical polymer properties. Thus, this approach can discriminate quantitatively between adhesion and viscoelastic properties which is normally considered very challenging for adhesive viscoelastic samples. The approach is demonstrated using experimental measurements using AC160 cantilevers on a PS-LDPE sample. The resulting quantitative maps of adhesion, long- and short-term elastic moduli are in line with ones reported previously in the literature [114, 121, 122].

3.2 Theory

We model the transverse deflection of the microcantilever, $w(x,t)$, with Euler-Bernoulli partial differential equation (PDE) for a beam with rectangular cross-section, as follows:

$$\rho_c A_c \ddot{w}(x,t) + F_{hydro}\left(\dot{w}(x,t), \ddot{w}(x,t)\right) + E_c I_c w''''(x,t) = F_{ts}(d,\dot{d})\,\delta(x - L_c) + F_{direct}(x,t), \quad (23)$$

where, x, t, ρ_c, A_c, E_c, I_c, and L_c are the longitudinal distance from the base of the microcantilever, time, the linear density, cross-sectional area, elastic modulus, area moment, and tip location distance from the base of the microcantilever, respectively. $\dot{w}(x,t)$ and $\ddot{w}(x,t)$ are the first and second derivative of $w(x,t)$ respect to t, respectively. $w''''(x,t)$ is the fourth derivative of $w(x,t)$ with respect to x. d and $\dot{d}$ are the tip-sample gap and its velocity relative to the undeformed surface level as shown in Figure 18. $F_{hydro}(\dot{w}(x,t), \ddot{w}(x,t)) = \overline{F}_{hydro}(x,t)$ is the uniformly distributed hydrodynamic force per unit length computable in the frequency domain using Sader's method [123], acting on the oscillating microcantilever. The tip-surface interaction force, $F_{ts}(d,\dot{d})$, which acts locally at the tip location is described with a Dirac delta function, δ. The microcantilever is excited directly[124], i.e. via photothermal, magnetic, or Lorentz for excitation, which exerts a Spatio-temporal distributed force per unit length, $F_{direct}(x,t)$. Dither piezo excitation will be included through the boundary conditions as described later in this section. The absolute deflection of the microcantilever is composed of the Z-piezo motion, $Z(t)$, the dither-piezo motion, $y(t)$, and the transverse vibration in the non-inertial frame attached to the base, $u(x,t)$:

$$w(x,t) = Z(t) + y(t) + u(x,t). \quad (24)$$

Substituting Eqn. (24) in the beam PDE, Eqn. (23), the equation of motion can be cast into the moving reference frame attached to the base of the microcantilever:

$$\rho_c A_c \ddot{u}(x,t) + F_{hydro}\left(\ddot{y}(t) + \ddot{u}(x,t) + \ddot{Z}(t), \dot{y}(t) + \dot{u}(x,t) + \dot{Z}(t)\right) + E_c I_c u''''(x,t) = F_{ts}(d,\dot{d})\,\delta(x - L_c) + F_{direct}(x,t) - \rho_c A_c\left(\ddot{y}(t) + \ddot{Z}(t)\right). \quad (25)$$

and the corresponding boundary conditions, ignoring the tip-mass effect become:

$$u(0,t) = 0, \qquad u'(0,t) = 0, \qquad u''(L_c,t) = 0, \qquad u'''(L_c,t) = 0. \quad (26)$$

For bimodal operation, excitation forces are applied at two eigenfrequencies of the microcantilever, $i = 1$, or fundamental mode frequency, and $i = 2$ or secondary mode frequency. The secondary mode is often the second eigenmode of the microcantilever, but it can instead be any higher order eigenmode. As a result, we can combine the net external excitation on the microcantilever as the sum of direct excitation and inertial excitation:

$$F_{direct}(x,t) - \rho_c A_c \ddot{y}(t) = \sum_{i=1}^{2} F_{drive,i}(x,t) \quad (27)$$

where $F_{drive,i}(x,t)$ are the net forcing functions at the two different drive frequencies. Therefore, we discretize Eqn. (25) using Galerkin's method based on microcantilever excited eigenmodes:

$$u(x,t) = \sum_{i=1}^{2} \bar{\Phi}_i(x)\, q_i(t), \quad (28)$$

where $\bar{\Phi}_i(x)$ and $q_i(t)$ describe the microcantilever eigenmodes of free vibration and the associated generalized coordinates, respectively. The mode shapes are normalized so that $\bar{\Phi}_i(L_c) = 1$ for each of the eigenmodes [91] and the generalized coordinates represent the tip motion in each eigenmode:

$$\rho_c A_c \sum_{i=1}^{2} \bar{\Phi}_i(x)\, \ddot{q}_i(t) + F_{hydro}\left(\sum_{i=1}^{2} \bar{\Phi}_i(x)\, \ddot{q}_i(t), \sum_{i=1}^{2} \bar{\Phi}_i(x)\, \dot{q}_i(t)\right) + E_c I_c \sum_{i=1}^{2} \bar{\Phi}_i''''(x)\, q_i(t) = F_{ts}(d,\dot{d})\,\delta(x - L_c) + \sum_{i=1}^{2} F_{drive,i}(x,t)\,. \quad (29)$$

Next, we use the biorthogonality of $\bar{\Phi}_i(x)$ terms to extract the discretized equations of motion of excited modes by multiplying Eqn. (29) once with $\bar{\Phi}_1(x)$ and then with $\bar{\Phi}_2(x)$, and then integrating respect to x. The resultant ODEs are:

$$\left(\rho_c A_c \int_0^{L_c} \bar{\Phi}_i^{\,2}(x)dx\right)\ddot{q}_i(t) + \int_0^{L_c} F_{hydro}\left(\sum_{i=1}^{2}\bar{\Phi}_i(x)\,\ddot{q}_i(t), \sum_{i=1}^{2}\bar{\Phi}_i(x)\,\dot{q}_i(t)\right)\bar{\Phi}_i(x)dx$$
$$+\left(E_c I_c \int_0^{L_c}\left(\bar{\Phi}_i''(x)\right)^2 dx\right)q_i(t) = F_{ts}(d,\dot{d}) + \int_0^{L_c}\bar{\Phi}_i(x)\sum_{i=1}^{2}F_{drive,i}(x,t)\,dx\,. \tag{30}$$

In order to simplify the F_{hydro} term, we note that in bimodal AFM operation the cantilever response generally combines harmonic motion at two discrete frequencies. Under these conditions it is reasonable to approximate the Fourier transform of F_{hydro} [123] as follows:

$$\bar{F}_{hydro}\left(x|\omega\right) = \int_{t=-\infty}^{\infty}\bar{F}_{hydro}\left(x,t\right)e^{-j\omega t}dt = \frac{\pi}{4}\rho\,\omega^2\,b^2\,\Gamma(\omega)\sum_{i=1}^{2}\bar{\Phi}_i(x)\int_{t=-\infty}^{\infty}q_i(t)\,e^{-j\omega t}dt \tag{31}$$

where, ρ, b, and $\Gamma(\omega)$ are the air density, nominal width of the microcantilever, and the dimensionless hydrodynamic function, respectively. The hydrodynamic force per unit length on the microcantilever can be converted into two frequency-dependent parameters: effective modal damping, $\hat{c}(\omega)$, and added mass, $\hat{M}(\omega)$ [123]. However, since the excitation forces in bimodal operation are applied on relatively narrow frequency ranges, the frequency dependence of $\hat{c}(\omega)$ and $\hat{M}(\omega)$ is weak and we can safely express them as follows:

$$\begin{aligned} m_j^* &= \hat{M}(\omega_j)\,, \\ c_j^* &= \hat{c}(\omega_j)\,. \end{aligned} \tag{32}$$

After rearranging Eqn. (30) to include experimentally observable parameters, the beam's PDE reduces into two coupled ODEs as follows:

$$\begin{aligned} \frac{1}{\omega_1^2}\ddot{q}_1(t) + \frac{1}{\omega_1 Q_1}\dot{q}_1(t) + q_1(t) &= \frac{1}{k_1}F_{ts}(d,\dot{d}) + \frac{1}{k_1}F_{11}(\omega_1,t) + \frac{1}{k_1}F_{12}(\omega_2,t) \\ \frac{1}{\omega_2^2}\ddot{q}_2(t) + \frac{1}{\omega_2 Q_2}\dot{q}_2(t) + q_2(t) &= \frac{1}{k_2}F_{ts}(d,\dot{d}) + \frac{1}{k_2}F_{21}(\omega_1,t) + \frac{1}{k_2}F_{22}(\omega_2,t) \end{aligned} \tag{33}$$

where,

$$F_{ij}(\omega_j,t) = \int_0^{L_c}\bar{\Phi}_i(x)\,F_{drive,i}(x,t)dx \quad,\ i,j = 1,2\,, \tag{34}$$

and k_i, $\omega_i = 2\pi f_i$, and Q_i are equivalent stiffness, natural frequencies (rad/s), and quality factor of the i^{th} mode ($i = 1, 2$), respectively. Solutions of Eqn. (33) show that $F_{ij}(\omega_j,t)$ has a negligible

effect on tip motion when $i \neq j$ and can be ignored. Then, we express the discretized ODEs by re-writing the excitation magnitudes in terms of the oscillation amplitudes in absence of the tip-sample interaction:

$$\begin{aligned}
&\frac{1}{\omega_i^2}\ddot{q}_1(t)+\frac{1}{\omega_i Q_i}\dot{q}_1(t)+q_1(t)=\frac{1}{k_1}F_{ts}(d,\dot{d})+\frac{A_{01}}{Q_1}\cos(\omega_1 t),\\
&\frac{1}{\omega_2^2}\ddot{q}_2(t)+\frac{1}{\omega_2 Q_2}\dot{q}_2(t)+q_2(t)=\frac{1}{k_2}F_{ts}(d,\dot{d})+\frac{A_{02}}{Q_2}\cos(\omega_2 t),\\
&d(t)=Z+q_1(t)+q_2(t)
\end{aligned} \tag{35}$$

where, A_{0i} is the "free" oscillation amplitude of the i^{th} mode, which is the forced steady-state amplitude in the absence of tip-sample interaction. Eqn. (13) represents the tip dynamics in bimodal AFM when the excitation frequencies exactly coincide with the natural frequencies. The method needs to be adapted if there is any intentional detuning between excitation and natural frequencies.

To derive amplitude reduction equations for bimodal AFM, we assume that the tip motion can be expressed as the sum of two harmonics at two different excitation frequencies, i.e.:

$$q(t)=q_1(t)+q_2(t)=A_1\cos(\omega_1 t-\phi_1)+A_2\cos(\omega_2 t-\phi_2), \tag{36}$$

where A_i and ϕ_i are the steady-state tip oscillation amplitude and phase lag of the i^{th} mode relative to its corresponding modal excitation force[42, 48]. This assumes that any slow time-scale amplitude and phase modulation leading to sidebands around the excited modes are considered negligible for amplitude reduction. It is also assumed that higher harmonics of the excited modes play a negligible role in the amplitude reduction at the two excitation frequencies, a condition generally met for air or in vacuum applications when higher eigenfrequencies are not integer multiples of the excited modes [49, 87, 125].

Next, we substitute $q_1(t)$ and $q_2(t)$ from Eqn. (36) into Eqn. (35):

$$\begin{aligned}
&-\frac{k_1}{Q_1}\left(A_1\sin(\omega_1 t-\phi_1)+A_{01}\cos(\omega_1 t)\right)=F_{ts}(d,\dot{d}),\\
&-\frac{k_2}{Q_2}\left(A_2\sin(\omega_2 t-\phi_2)+A_{02}\cos(\omega_2 t)\right)=F_{ts}(d,\dot{d}),
\end{aligned} \tag{37}$$

where, $d(t)=Z+q_1(t)+q_2(t)$. Then, we multiply Eqn. (37) with $q_i(t)$ and integrate with respect to time over 0 to $n_c T_1$. Then, we repeat the process by multiplying Eqn. (37) with $\dot{q}_i(t)$

and then integrating with respect to time over 0 to $n_c T_1$. The coefficient n_c represents the number of slow time-scale periods that the mode parameters are computed and averaged over. Thus yielding:

$$V_{ts,i} = \frac{1}{n_c T_i}\int_0^{n_c T_i} F_{ts}\left(d,\dot{d}\right) q_i(t)dt = \frac{1}{n_c T_1}\int_0^{n_c T_1} F_{ts}\left(d,\dot{d}\right) A_i \cos(\omega_i t - \phi_i)dt = -\frac{k_i A_{0i} A_i}{2Q_i}\cos(\phi_i),$$

$$E_{ts,i} = -\frac{1}{n_c}\int_0^{n_c T_i} F_{ts}\left(d,\dot{d}\right) \dot{q}_i(t)dt = \frac{T_i}{n_c T_1}\int_0^{n_c T_1} F_{ts}\left(d,\dot{d}\right) \times A_i\omega_i \sin(\omega_i t - \phi_i)dt = \frac{\pi k_i A_i A_{0i}}{Q_i}\left(\sin(\phi_i) - \frac{A_i}{A_{0i}}\right). \quad (38)$$

Here, T_i, $V_{ts,i}$, and $E_{ts,i}$ are the time period, the average value of the virial (conservative interactions), and dissipation (non-conservative interactions) associated with the i^{th} mode during each interaction cycle[89]. $V_{ts,i}$ and $E_{ts,i}$ are computed and averaged over many time-periods of the fundamental mode ($n_c T_1$). This mimics the experimental conditions where lock-in amplifiers average these quantities for the two excited modes over the slow timescale. If the ratio of excitation frequencies is equal to the ratio of two integer numbers, the resultant bimodal tip trajectory is periodic, and it simplifies the parameters' calculation. However, the driving frequencies of the microcantilevers are generally incommensurate[126] and the tip motion can be quasi-periodic[127].

The amplitude reduction formulas for the first and secondary modes are then attained by eliminating ϕ_i in Eqn. (38) as follows:

$$A_i^{ratio} = \frac{A_i}{A_{0i}} = \frac{\pi k_i A_i^2/Q_i}{\sqrt{\left(-2\pi V_{ts,i}\right)^2 + \left(\frac{\pi k_i A_i^2}{Q_i} + E_{ts,i}\right)^2}}, \quad (39)$$

where, $i = 1, 2$ and A_i^{ratio} is the amplitude ratio for the i^{th} mode: $\left(A_i/A_{0i}\right)$. In addition to the amplitude reduction equations, removing $\sin(\phi_i)$ and $\cos(\phi_i)$ terms in Eqn. (38) leads to the phase lag equations:

$$\phi_i = \tan^{-1}\left(\frac{\pi k_i A_i^{\,2}/Q_i + E_{ts,i}}{-2\pi V_{ts,i}}\right), \tag{40}$$

The tip-sample interaction force (F_{ts}) in Eqn. (38) can, in principle, be calculated using any appropriate contact model. Here, the tip-surface interactions on viscoelastic polymeric surfaces are computed using the accelerated Attard's model and the viscoelastic behavior of the polymer is modeled by using an SLS model, except otherwise specified. The Creep compliance function of the SLS constitutive model is:

$$\frac{1}{E(t)} = \frac{1}{E_\infty} + \frac{E_\infty - E_0}{E_0 E_\infty} e^{-t/\tau}, \tag{41}$$

that includes a single relaxation time, which governs how fast the instantaneous modulus of the sample changes from E_0 (short-term modulus of the sample) to E_∞ (long-term modulus once the material is completely relaxed). Attard's three-dimensional viscoelasticity model correlates the radial time-dependent sample surface deformation, $u(r,t)$, to its rate of change, $\dot{u}(r,t)$, through its interaction with an axisymmetric rigid tip[2]:

$$\dot{u}(r,t) = -\frac{1}{\tau}\left(u(r,t) - u_\infty(r,t)\right) - \frac{1}{E_0}\int_0^\infty k(r,s)\,\dot{p}(h(s,t))\,s\,ds, \tag{42}$$

where, $p(h(r,t))$ is the interaction force per unit area (pressure) between the tip and the surface. $p(h(r,t))$ is a function of $h(r,t)$ which is the radial time-dependent gap between the axisymmetric tip and the deformed sample at time t and radius r from the central axis. In this work, we calculate $p(h(r,t))$ based on the Lennard-Jones pressure equation:

$$p(h(r,t)) = H/6\pi h(r,t)^3\left(z_0^6/h(r,t)^6 - 1\right), \tag{43}$$

where z_0 and H are the intermolecular equilibrium distance and Hamaker constant, respectively. Also, $\dot{u}(r,t)$ and $\dot{p}(h(r,t))$ are time derivatives of $u(r,t)$ and $p(h(r,t))$, respectively. The long-time static deformation of the surface, $u_\infty(r,t)$, is defined as:

$$u_\infty(r,t) = -\frac{1}{E_\infty}\int_0^\infty k(r,s)\,p(h(s,t))\,s\,ds, \tag{44}$$

and the kernel of the integral, $k(r,s)$, can be expressed in terms of the complete elliptic integral of the first kind[81], K, as shown below:

$$k(r,s)=\begin{cases}\dfrac{4}{\pi r}K(s^2/r^2) & s<r\\ \dfrac{4}{\pi s}K(r^2/s^2) & s>r\end{cases}. \qquad (45)$$

Attard's model parameters and the associated computational methods are elaborated elsewhere [1].

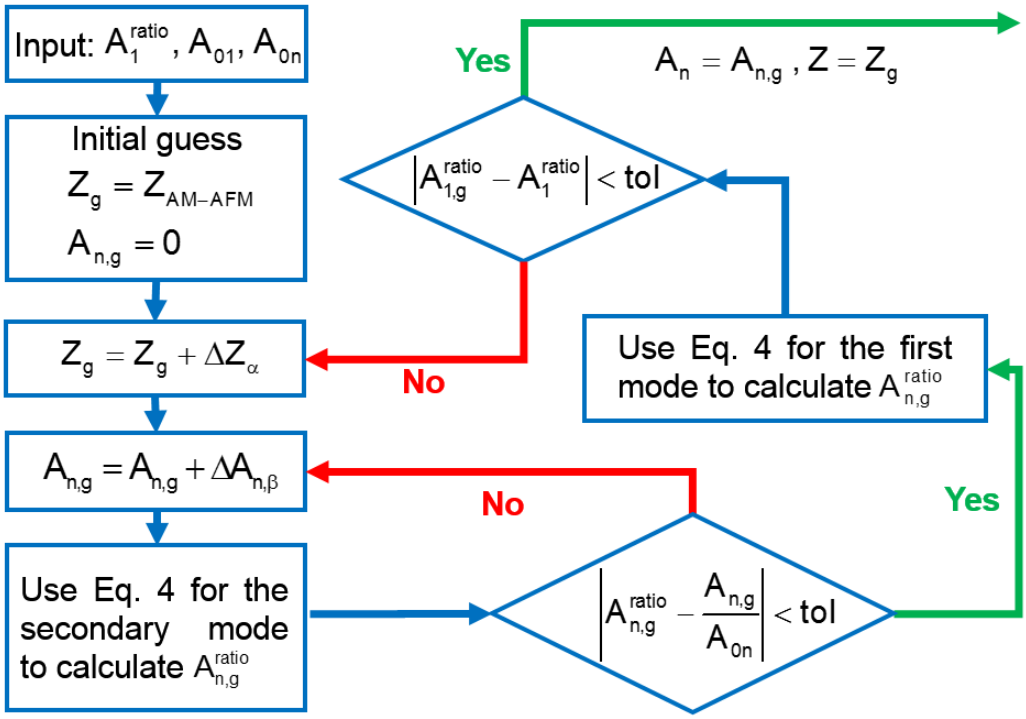

Figure 19. The algorithm proposed in this work for predicting instrument observables in bimodal AFM through simultaneous compliance of the amplitude reduction formulas for both driven modes.

To embed Attard's model into the bimodal AFM framework, we propose an algorithm (Figure 19) that can predict the Z distance and associated ϕ_1, A_n, and ϕ_n for a given A_1^{ratio}, A_{01}, and A_{0n}. In this algorithm, we assume the cantilever is simultaneously excited exactly at two of its eigenfrequencies (i=1 and i=n) and the relevant parameters are labeled accordingly. The algorithm simultaneously satisfies the amplitude reduction formulas (Eqn. (39)) for both excited modes and computes the resulting bimodal phases (Eqn. (40)). The subscript "g" denotes a guessed value for a parameter and the subscripts "α" and "β" represent the number of iterations of each loop. $Z_g = Z_{AM-AFM}$ is the initially guessed Z value using a previously proposed algorithm for AM-AFM[1]. ΔZ_α and $\Delta A_{n,\beta}$ are the adjustments made to Z and A_n at each iteration,

respectively which are applied to the guessed values to facilitate the convergence process. These values (ΔZ_{α} and $\Delta A_{n,\beta}$) are updated at each iteration to achieve accelerated convergence. When both loops are satisfied as directed by the algorithm, all bimodal AFM parameters such as Z, indentation, second mode amplitude, energy dissipations, and virials are recorded for the given set of input parameters. A tolerance (" tol " as shown in Figure 19) of 10^{-2} which facilitates a reasonable accuracy is used to fulfill the condition of the algorithm.

3.3 Verification of the amplitude reduction algorithm

To verify Eqn. (39) and (40), the predictions from the proposed algorithm are compared to experimental data from literature[42] extracted on a stiff (silicon) elastic sample and simulation results from the AMAC (amplitude modulated approach curves) tool of VEDA (Virtual Environment for Dynamic AFM) which includes explicit microcantilever dynamics in bimodal AFM[74]. The interaction force $\left(F_{ts}\right)$ is calculated using the DMT (Derjaguin, Muller, and Toporov) model[53], and the surface and interaction parameters[42] are mentioned in the caption of Figure 20. The results from the algorithm show an excellent agreement with the experimental and simulation data. In these simulations, the tip oscillates in the attractive regime ($\phi_1 > 90^{\circ}$).

To examine the accuracy of the model predictions when the tip-surface interaction is in the repulsive regime, we conducted another set of simulations on a softer elastic surface which its parameters are mentioned in the caption of Figure 21. The interaction force $\left(F_{ts}\right)$ is calculated using the DMT model. The predictions from the proposed algorithm (Figure 21) again show excellent consistency with the results of VEDA tools for this scenario in which the oscillation regime is repulsive ($\phi_1 < 90^{\circ}$) (Figure 21).

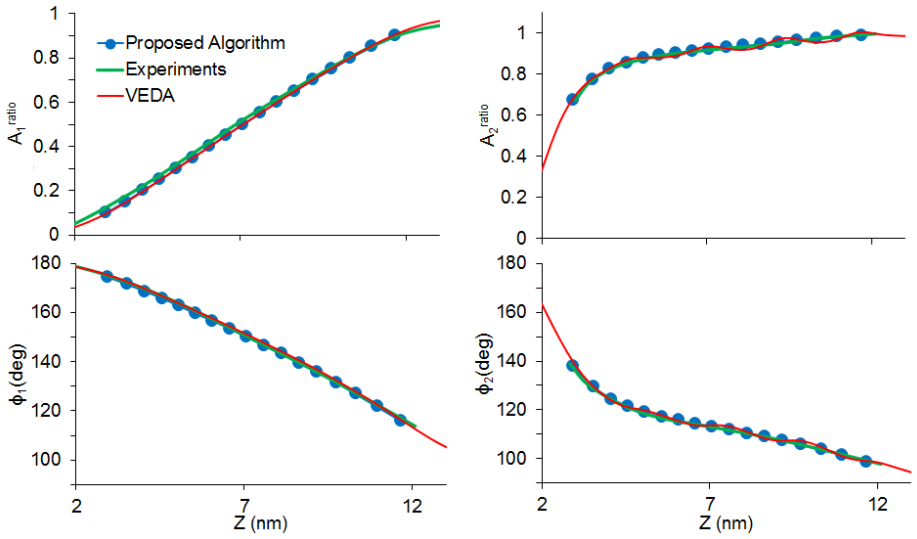

Figure 20. Validation of Eqn.'s (39) and (40) against previously published bimodal AFM experimental data *[42]* and simulation results extracted using the AMAC tool of VEDA *[74]* on a Silicon sample illustrates excellent agreement. The A_1^{ratio} range used for these simulations is between 0.1 and 0.9. The employed parameters in these simulations are as follows: $A_{01} = 10\,\text{nm}$, $A_{02} = 1\,\text{nm}$, $H = 9.03\times10^{-20}\,\text{J}$, $k_1 = 0.9\,\text{N/m}$, $k_2 = 35.2\,\text{N/m}$, $f_1 = 48.913\,\text{kHz}$, $f_2 = 306.194\,\text{kHz}$, $Q_1 = 255$, and $Q_2 = 1000$ *[42]*.

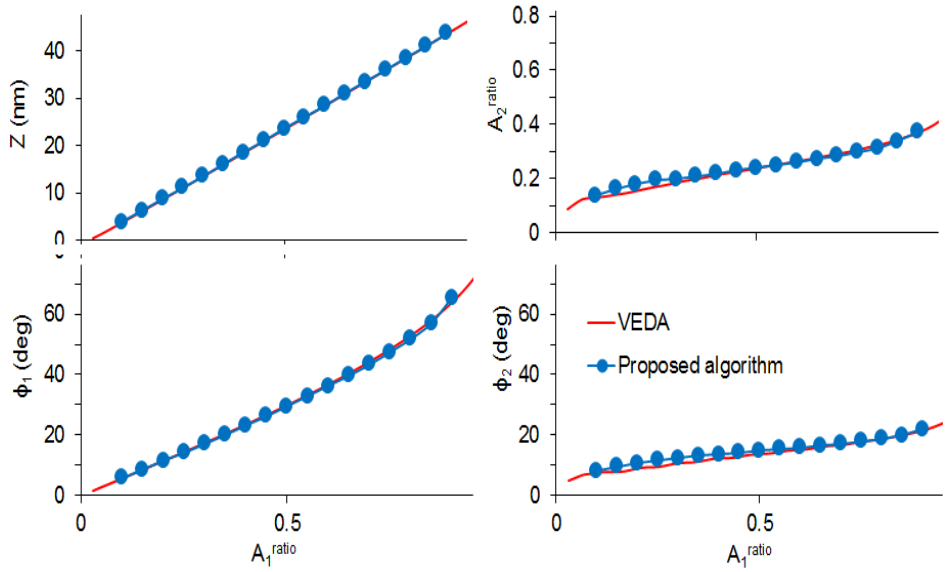

Figure 21. Validation against bimodal AFM simulation results extracted using the AMAC tool of VEDA [74] on an elastic sample illustrates perfect agreement with the proposed algorithm. The used values for material properties, microcantilever, and DMT model parameters are: $A_{01} = 50\,\text{nm}$, $A_{02} = 1\,\text{nm}$, $f_2/f_1 = 6.26$, $E = 1\,\text{GPa}$, and $H = 7.55\times10^{-20}\,\text{J}$. The Ar_1 range used for these simulations is between 0.1 and 0.9.

3.4 Computational results

To predict the dependence of bimodal AFM observables on adhesive and viscoelastic properties of local polymeric domains using the proposed Attard's model, we conduct a set of simulations using typical viscoelastic polymer properties[92]. The values for operational parameters and the cantilever properties are chosen in range with what is commonly used for bimodal AFM experiments on polymers. Different creep (retardation) times (τ) ranging between 3.2×10^{-5} s and 3.2×10^{-10} s are employed in the simulations while all other parameters are held fixed. This range for τ was chosen to span the range from much smaller to much larger than tip-surface interaction time.

Typical calibration values of Olympus AC160-R3 microcantilevers are used in these simulations: $f_1 = 280\,\text{kHz}$, $k_1 = 28.1\,\text{N/m}$, $Q_1 = 430$, $f_2 = 1593\,\text{kHz}$, and $Q_2 = 600$. The calibration methods are explained in the experimental section. A_{01} and A_{02} are selected to be $50\,\text{nm}$ and $1\,\text{nm}$, respectively. We specifically chose a small A_{02}/A_{01} ratio to avoid crosstalk between modes as suggested by others [47-50].The surface properties used are listed in Table 5.

Table 5. The surface properties used to predict the dependence of bimodal observables on local adhesive and viscoelastic polymer properties using the proposed algorithm.

τ	E_0	E_∞	H	z_0	ν
varies	2.0 GPa	0.5 GPa	5×10^{-20} J	0.28 nm	0.49

Simulation results are shown in Figure 22 as a function of A_1^{ratio} . As discussed elsewhere [1], the calculated values for ϕ_1 (Figure 22-a), which depend on the average dissipated energy during each interaction cycle[95], are a function of the ratio between the interaction time (the duration on which the tip experiences surface forces) and the effective relaxation (or creep) time for viscoelastic samples. When $\tau \ll$ contact time or $\tau \gg$ contact time, the polymer is either nearly completely relaxed or relaxes very little during the interaction time, respectively. In both cases, minimal hysteresis occurs during tapping cycles. However, when τ value gradually changes between these two extremes, energy dissipation during each interaction cycle appears, rises to its maximum, and then gradually vanishes. This phenomenon leads to the non-monotonic behavior of

ϕ_1 and E_{ts} vs. τ for a fixed A_1^{ratio} in Figure 22 (a and e) as observed previously for tapping mode[1] on viscoelastic and adhesive surfaces.

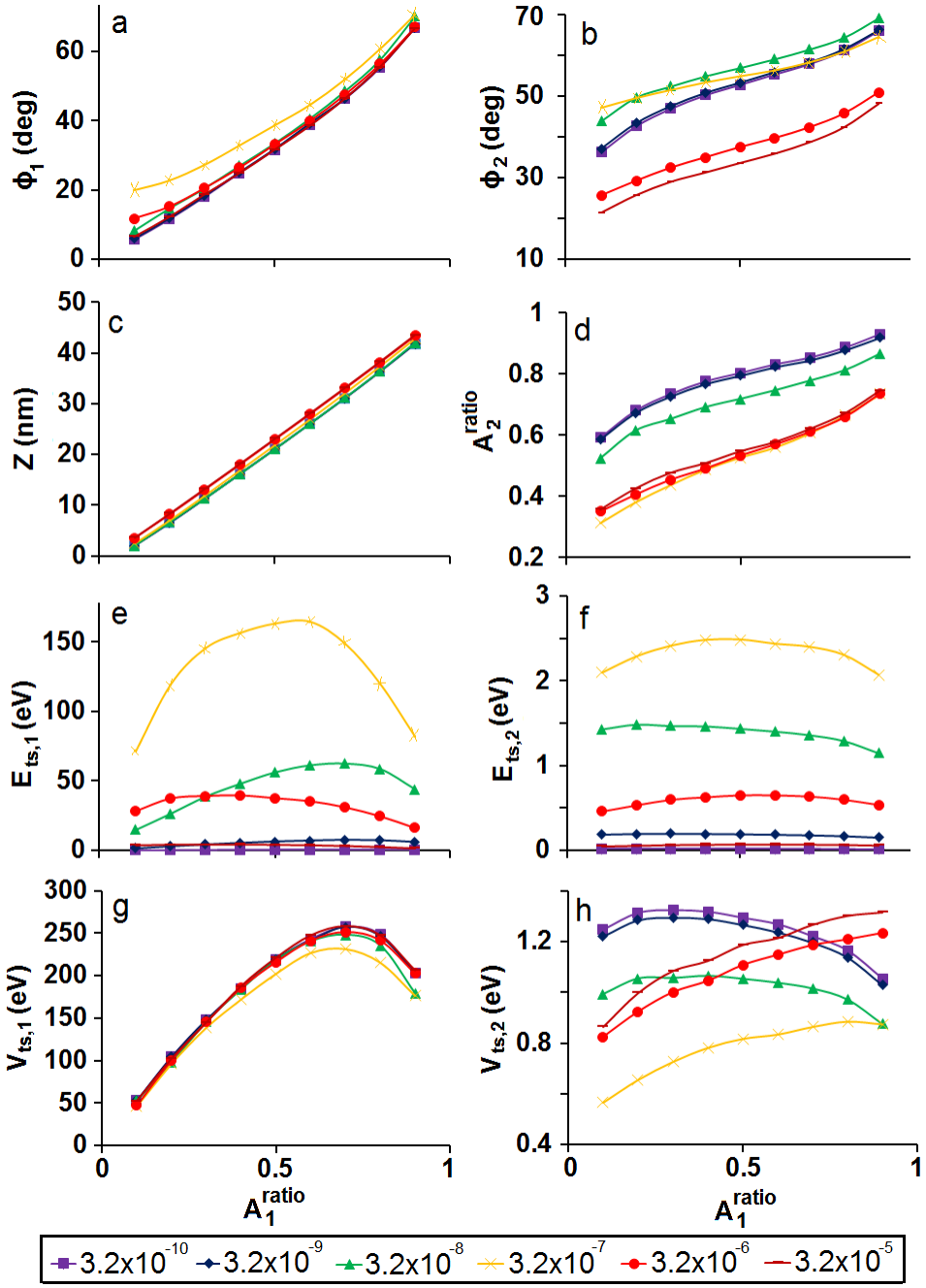

Figure 22. Study of the bimodal observables' sensitivity to the effective creep time of the polymer (τ). Selected τ values are stated in the legends and the range is between 3.2×10^{-5} s to 3.2×10^{-10} s.

Figure 5 provides key insights into the sensitivity of bimodal observables to local changes in tau while scanning a hypothetical sample where other parameters such as E_∞ and E_0 are held constant. While ϕ_1 changes more sensitively with A_1^{ratio} than ϕ_2, when the main difference between two adjacent domains on the surface is their associated effective relaxation time, ϕ_2 can discriminate much more effectively between regions where τ is much smaller or much larger than the contact time. A clue to the underlying reasons for this behavior can be found in Figure 22 f and h which show that across the five orders of magnitude changes in τ studied, the range of attained values for $V_{ts,2}$ is much smaller than the range of ones attained for $E_{ts,2}$. When combined with the fact that $\pi k_2 A_2^2/Q_2 \ll \pi k_1 A_1^2/Q_1$ due to the amplitude difference between modes, the resulting ϕ_2 (Eqn. (40)) thus depends proportionally more on $E_{ts,2}$ and $V_{ts,2}$ compared to the dependence of ϕ_1 on $E_{ts,1}$ and $V_{ts,1}$. For these reasons ϕ_2 appears more sensitive than ϕ_1 to τ change. In addition, the amplitude of the second mode (A_2), as depicted in Figure 22 (b), monotonically changes with relaxation time (). As illustrated, for the same setpoint for the amplitude of the first mode, when ($\tau \ll$ contact time) and sample's stiffness is almost like E_∞ (softer), A_2 is larger than when ($\tau \gg$ contact time) and the sample's stiffness is almost like E_0 (stiffer). In both of these cases, the energy dissipation due to viscoelasticity is ≈ 0 and according to Eqn. (38), A_2 is related to ϕ_2 as follows: $A_2 = A_{02}\sin(\phi_2)$. Therefore, when energy dissipation by the second mode is negligible, larger ϕ_2 results in a greater A_2 prediction.

A comprehensive study of the dependence of bimodal AFM observables on local adhesive and viscoelasticity parameters for a fixed τ is presented in Figure 23. The microcantilever properties, A_{01}, and A_{02} of these simulations are identical to the ones used for Figure 22 and the A_1^{ratio} is 0.5. The simulation results for various viscoelasticity model parameters and two different surface adhesions are presented in Figure 23. These are the identical parameters used for all the conducted simulations: $R = 3\,\text{nm}$, $A_1^{ratio} = 0.5$, and $\tau = 0.1\,\mu\text{s}$. The Poisson ratio (ν) for the LDPE and PS domains are chosen as the nominal values provided by the manufacturer, 0.49 and 0.35, respectively. . E_0 and E_∞ values for the simulations are selected based on the Latin hypercube sampling method. Since ($A_{02}/\text{indentation depth} << 1$), the interaction time is mainly dictated by the first mode and our previous studies on the relaxation mode(s) of the polymer that contributes

the most to energy dissipation during a tapping cycle of AM-AFM *[1]* is indeed applicable to bimodal AFM. Therefore, we chose the creep time of the polymers to be $0.1\,\mu s$ for all simulations conducted.

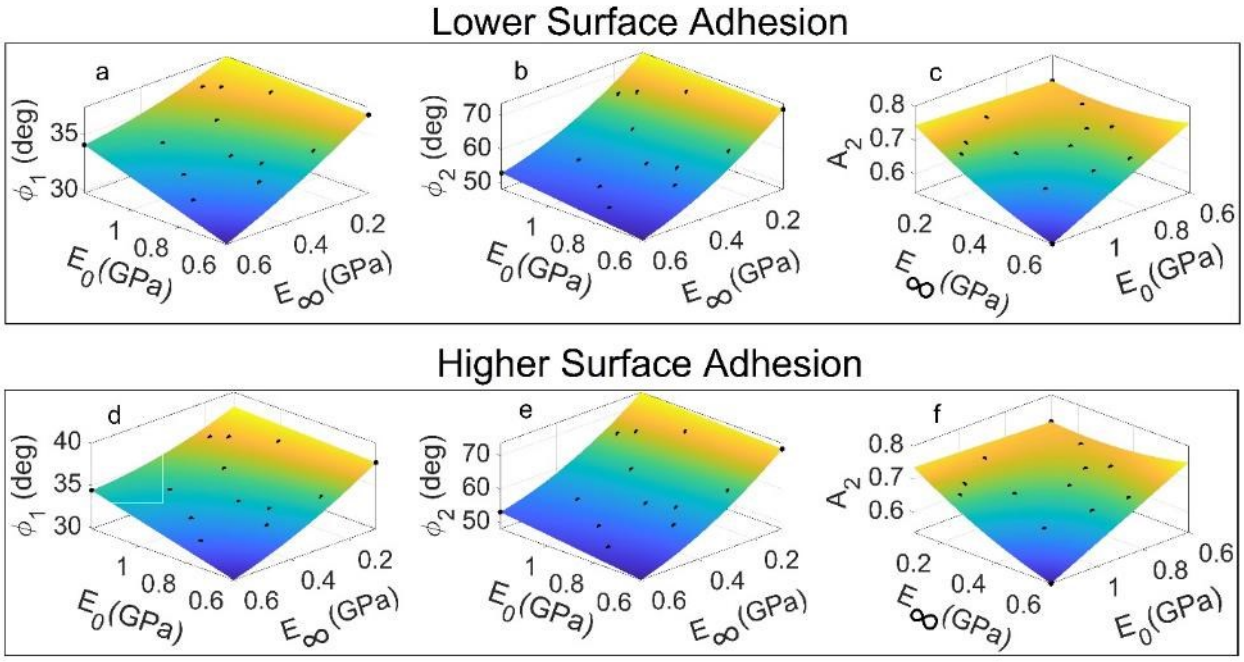

Figure 23. Study of the bimodal observables' dependence on the surface adhesion (quantified as $HR/6z_0^2$) and viscoelasticity level. The first row (a-c) and second row (d-f) simulations have smaller and larger adhesions associated with $H = 1\times10^{-20}$ J and $H = 7\times10^{-20}$ J, respectively. The selection of E_0 and E_∞ in the performed simulations are done based on the "Latin hypercube sampling" method. The used material and interaction parameters are stated in the text. In these conducted simulations $R = 3$ nm, $A_1^{ratio} = 0.5$, $\nu = 0.49$, and $\tau = 0.1\,\mu s$

As seen in Figure 23, the hysteresis due to surface adhesive forces is larger when E_∞ and/or adhesive forces are relatively smaller and larger, respectively. Furthermore, while ϕ_2 is generally more sensitive to changes in surface viscoelasticity, the surface adhesion is better resolved via ϕ_1. The higher sensitivity to the magnitude of surface adhesion of ϕ_1 in comparison with ϕ_2 can be explained through the tip velocity-dependency of the energy dissipation as expressed in Eqn. (38). Therefore, since the adhesive forces between tip and surface during the interaction time occur when the tip experiences the largest first mode velocities, their contribution toward first-mode dissipation weighs more than equally-in-size repulsive forces. This relation holds either during

approach or retraction off the surface. However, in terms of the secondary mode energy dissipation contributions, there is no such relation between the tip secondary mode velocity and the adhesive forces.

3.5 Material viscoelasticity and adhesive properties estimation

We explore utilizing the proposed computational approach to post-process the experimental observables and estimate the surface adhesive and viscoelastic properties. Since the accelerated Attard model does not provide a closed-form solution, finding a correlation between the experimental data and the surface properties is challenging. Here we present a data analysis approach to connect the bimodal AFM observables to the material's properties through an inverse model.

The data analysis approach requires a comprehensive set of simulations with an appropriate range for E_0, E_∞, surface static adhesion, and tip radius (R) values for known AFM microcantilever properties and operating conditions (k_1, k_2, Q_1, Q_2, A_{01}, A_1^{ratio}, A_2^{ratio}). We select $\tau = 0.1\,\mu s$ with the same reasoning described previously. The Poisson ratio (ν) for the LDPE and PS domains are chosen as the nominal values provided by the manufacturer, 0.49 and 0.35, respectively. This inclusive bimodal database with known input parameters facilitates a regression-based analysis to identify and recognize the existing dataset patterns. We used a method based on the multivariate linear regressions to estimate E_0, E_∞, and surface static adhesion from the measured ϕ_1, ϕ_2, and A_2 values at each pixel. In order to minimize the precision loss due to using linear regression, we select the range of E_∞ in the simulation results datasets in accordance with the expected material properties. The process utilized can be represented as a conversion matrix and vector, as follows:

$$\begin{Bmatrix} \phi_1 \\ \phi_2 \\ A_2 \end{Bmatrix} = \begin{bmatrix} c_1 & c_2 & c_3 \\ c_4 & c_5 & c_6 \\ c_7 & c_8 & c_9 \end{bmatrix} \begin{Bmatrix} E_0 \\ E_\infty \\ Adh \end{Bmatrix} + \begin{Bmatrix} d_1 \\ d_2 \\ d_3 \end{Bmatrix} \tag{46}$$

3.6 Experiments

To validate the performance of the described inverse approach, we acquired a set of experimental bimodal AFM data on a polymer blend sample and used it to estimate its viscoelastic and adhesive properties. The bimodal AFM experiments are performed using a commercial Cypher AFM setup (Asylum Research, Santa Barbara, CA) on a fresh PS-LDPE polymer blend which was purchased from Bruker Nano Inc. The experiments are performed on a $4\times4\ \mu m$ rectangular region with a 1024 points/line resolution level and a scan rate of 1 Hz. The sample is selected due to the significant mechanical difference between polymer domains, as the bulk nominal Young's modulus for PS and LDPE are 2 GPa and 0.1 GPa, respectively, as per the product description. By calibrating Olympus AC160 microcantilevers, the following parameters are determined: $f_1 = 281\,\text{kHz},\quad f_2 = 1.593\,\text{MHz},\ k_1 = 28.1\,\text{Nm}^{-1},\quad k_2 = 509.8\,\text{Nm}^{-1},\quad Q_1 = 429,\quad Q_2 = 600,$ $A_{01} = 50\,\text{nm},$ and $A_{02} = 1\,\text{nm}$. The calibration of the first mode stiffness was performed based on two well-established calibration techniques: the Sader method [128] and the thermal noise method[129]. This arrangement which does not require mechanical contact with a hard sample during the calibration is accessible through the GetReal™ tool in the instrument software. The calibration of the second mode stiffness was performed using the suggested power-law relationship between stiffness and frequencies of the excited modes: $k_2 = k_1\left(f_2/f_1\right)^{\xi_2}$, where ξ_2 is the calibration parameter which is empirically determined for specific microcantilevers[130, 131]. The calibration values obtained using the mentioned method were compared with the ones from the slope of the dynamic amplitude approach curve for the second eigenfrequency and the one for the quasi-static force curve for the first resonance mode on a fresh clean silicon sample and the agreement of the acquired values was satisfactory. The blueDrive photothermal excitation system excites the microcantilever at two eigenfrequencies (1 and 2). Modal amplitudes and phases were tuned when the microcantilever was within 100 nm above the surface. We specifically suggest A_1^{ratio} at 0.5 for the experiments to maximize the energy dissipation during each cycle[1]. The experiments were conducted under ambient temperature and dry nitrogen flushed conditions to minimize the effect of capillary forces. As shown in Figure 24, The polymeric domains are well separated. The round shapes on the images are LDPE domains which are surrounded by a homogeneous PS background. We use the bimodal observables of each pixel of the images, i.e.

ϕ_1, ϕ_2, and A_2, to estimate the surface nanoscale properties using the regression model (Eqn. (44)).

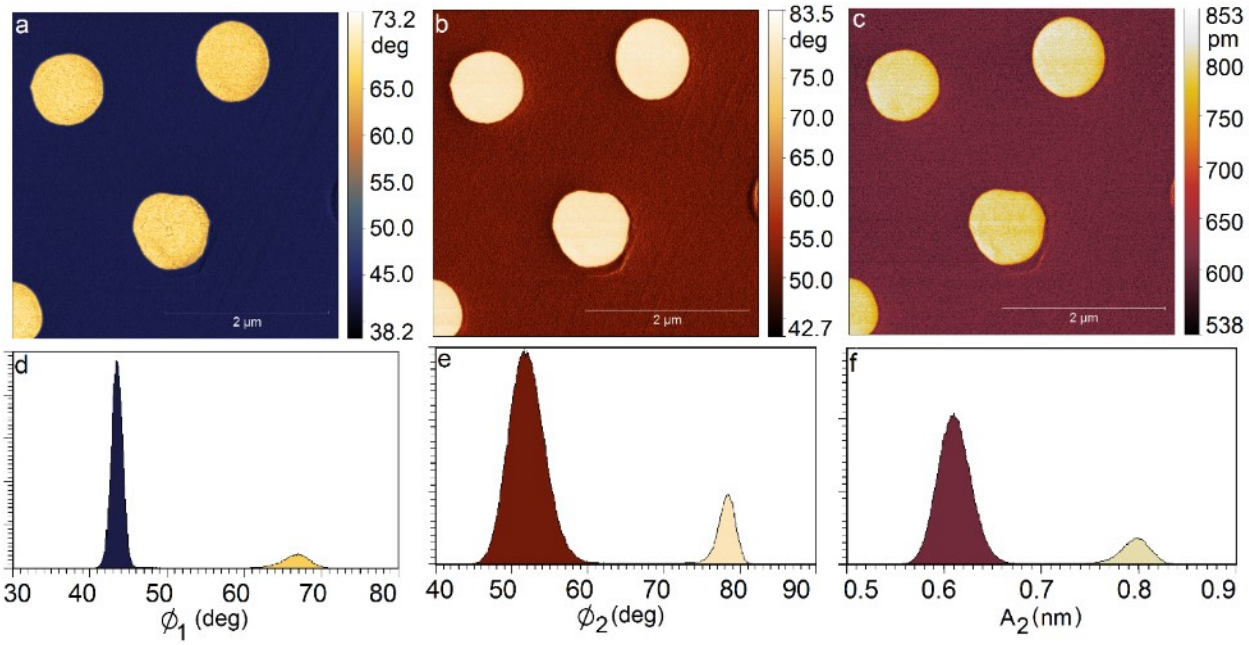

Figure 24. Bimodal images of the PS-LDPE sample illustrate phase lag of the first and second mode, and amplitude of the 2nd mode from left to right, respectively. The associated histograms are shown in the second row. The size of the images is 4×4 µm.

The calculated c_i and d_i constant terms of Eqn. (44) are determined through linear regression on the relevant simulation results datasets and are listed in Table 6. The spatially resolved surface properties estimations using the described inverse approach are shown in Figure 25 and the predicted mean values for polymer domains are listed in Table 7. Since similar samples were previously explored by others, here we compare our results with their predictions. Garcia et al.[114] presented a method in which the model parameters were first calibrated on the PS domain so that the model predictions for PS stiffness becomes comparable with expected values. Then, the calibrated model was applied to LDPE domain leading to stiffness estimates of 0.11 ± 0.02 GPa which compares well to our E_∞ value prediction as listed in Table 7. In their method, the viscoelasticity of the surface was described by a so-called "3D Kelvin–Voigt model" in which the surface adhesion is neglected. Meng et al.[132] employed an elastic-based model to estimate the PS-LDPE surface adhesion and stiffness using magnetic-drive soft probes. The resultant mean reduced modulus predictions for PS and LDPE phases were 0.1 and 1.8 GPa, respectively which

compare well to our results. Since each group used different microcantilevers to conduct experiments, we compare the predicted adhesion force values for PS and LDPE phases through the ratio of the mean predicted adhesions for these domains. Meng et al. and Solgaard et al. reported adhesions ratio as 1.26[132] and 1.2~2.0[121] which is in agreement with 1.29 predicted by our method. Therefore, we conclude that despite the simplifications applied to the proposed algorithm, the attained results prove the capability of the employed model to make realistic predictions.

Table 6. The coefficients of the conversion matrix and vector as described in Eqn. (46) determined through linear regression on simulation results. The tip radius estimate is 8.7 nm.

	c_1 (GPa)	c_2 (GPa)	$c_3\left(\frac{\text{GPa}}{\text{nm}}\right)$	c_4 (GPa)	c_5 (GPa)	$c_6\left(\frac{\text{GPa}}{\text{nm}}\right)$
PS	0.89	6.81	-0.21	0.14	-33.72	0.15
LDPE	0.23	2.41	-0.07	0.07	-1.24	-0.003
	c_7 (nN)	c_8 (nN)	c_9 (Pa)	d_1 (GPa)	d_2 (GPa)	d_3 (nN)
PS	0.18	-1.62	-0.14	-22.54	8.36	-0.08
LDPE	0.008	0.69	-0.02	-4.06	-0.49	0.99

Table 7. Predicted mean viscoelastic properties for the polymer domains based on the acquired bimodal AFM data. The predictions agree with the ones in the literature *[114, 121, 132]*.

domain	E_0(GPa)	E_∞(GPa)	Static Adhesion (nN)
PS	5.68 ± 0.31	1.82 ± 0.31	8.08 ± 0.91
LDPE	2.73 ± 0.11	0.11 ± 0.03	6.28 ± 0.22

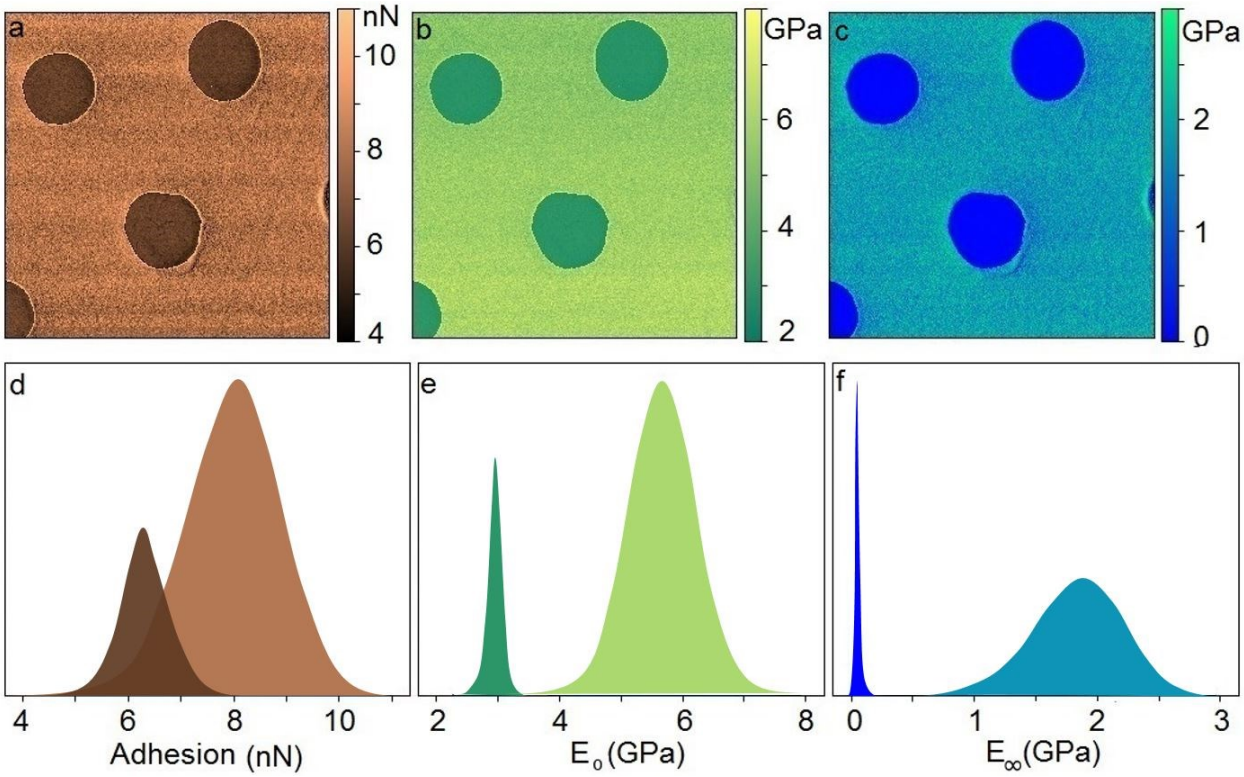

Figure 25. The estimates for adhesion force, E_∞ and E_0 values for the scanned polymer domains are predicted using the proposed algorithm. The static adhesion is calculated based on $HR/6z_0^2$.

3.7 Conclusions

This work features a proposed algorithm that systematically accommodates surface forces and linear viscoelastic three-dimensional deformation into the bimodal AFM framework. To establish the algorithm, we derived the amplitude reduction formulas for the resonant modes in bimodal AFM based on the Euler Bernoulli assumption for the microcantilever behavior. The algorithm simultaneously satisfies the derived amplitude reduction formulas for both resonant eigenmodes while the tip-surface interaction is computed using the accelerated Attard's model. The algorithm enables the rigorous prediction and interpretation of bimodal AFM observables with a first-principles approach. Simulations illustrate that bimodal AFM can provide enhanced contrast between domains with relaxation time discrepancies in comparison with the conventional tapping mode AFM. The results show that ϕ_2 channel is more responsive to the viscoelasticity level of the sample than ϕ_1. However, ϕ_1 channel is more sensitive to the surface adhesion level than ϕ_2.

Furthermore, simulations showed that the phase lag and amplitude ratio of the secondary mode illustrates a nonmonotonic and monotonic variation versus relaxation time, respectively. Then, we presented an inverse surrogate-model-based method that quantitatively predicts the local adhesion and standard linear solid viscoelastic parameters from acquired bimodal data. The application of this method on bimodal AFM data on a PS-LDPE polymer blend leads to quantitative discrimination of adhesion and viscoelastic properties of the sample. Taken together, the results presented here successfully open the way to advanced interaction models to be used to quantify local nanomechanical properties of soft, adhesive, and viscoelastic materials in bimodal AFM.

4. A FAST FIRST-PRINCIPLES APPROACH TO MODEL ATOMIC FORCE MICROSCOPY ON ADHESIVE VISCOELASTIC SURFACES

The previous chapters have illustrated approaches that allow Attard's model to be accelerated computationally and embedded in algorithms that can predict the dAFM observables given the sample adhesive and viscoelastic properties. In this chapter, we render Attard's contact model, one of the most rigorous models for tips interacting with adhesive viscoelastic samples, into an easy-to-use, fast, and more robust computational tool than either Attard's original method or the accelerated implementation of the previous chapters. In the proposed enhanced Attard's model (EAM) the surface deformation is reconstructed using a complete set of optimized biorthogonal basis functions as opposed to the computationally expensive radial discretization-based approach employed by Attard. The use of higher-order numerical procedures in EAM to solve the model's governing ordinary differential equations (ODEs) leads to more stable solutions even for soft and sticky samples. We also rearranged the original model's formalism to enable a fast and explicit solution of the model ODEs. Implementing these enhancements, EAM is more stable, 3+ orders of magnitude faster, and equally accurate when compared to the original model. These improvements facilitate the inclusion of EAM into simulations of various AFM modes of operation. This is demonstrated with fast simulations of force-distance curves and amplitude modulation AFM on soft polymer surfaces. On a typical desktop computer, simulation of an amplitude modulation approach curve with EAM takes less than a minute as compared to ≈ 15 hours by the original Attard's model. The Fast and rigorous EAM predictions for AFM on soft, viscoelastic polymers with surface forces provide significant insight to better understand the complex tip-surface interaction phenomena and also AFM images interpretations on such samples.

4.1 Introduction

In this work, we use strategies to significantly enhance the computational part of Attard's model and turn it into a faster and more robust first-principles approach. First, we rearranged the model formalism so that its governing differential equations become explicitly solvable. Next, we approximate the deformed surface profile using a complete set of optimized biorthogonal basis functions to replace the radial discretization in the original model. Finally, we used higher-order

numerical procedures to solve the model's ordinary differential equations instead of the original forward Euler's method. To demonstrate the utility of EAM in the AFM context, we performed simulations of an AFM force-distance curve and a dynamic approach/retract curve on polymeric surfaces. EAM utilization to make predictions or interpret AFM images of soft viscoelastic sticky polymers provides a fast path to gain further insight into the complex tip-surface interaction phenomena on such samples.

4.2 Methods

The elastic equation for a semi-infinite half-space predicts the surface deformation due to a distributed applied force as follows [133]:

$$u(\mathbf{r}) = -\frac{1-\nu^2}{\pi E}\int \frac{p(\mathbf{s})}{|\mathbf{r}-\mathbf{s}|}d\mathbf{s}\,, \tag{47}$$

where $\mathbf{r}$ is the position vector to the point of interest on the surface, $u(\mathbf{r})$ is the surface deformation at $\mathbf{r}$, and $p(\mathbf{s})$ defines the distributed pressure applied on the surface with elastic modulus E and Poisson ratio ν. When a rigid tip contacts a surface, $p(\mathbf{r})$ arises from the local instantaneous tip-surface interaction forces which their magnitude depends on $h(\mathbf{r},t)$, the tip-deformed surface distance. These parameters for an interacting tip-surface ensemble are shown in Figure 26. With a parabolic approximation of the rigid tip profile, the geometry parameters can be correlated as:

$$u(\mathbf{r},t) = h_0(t) + \mathbf{r}^2/2\,R - h(\mathbf{r},t)\,. \tag{48}$$

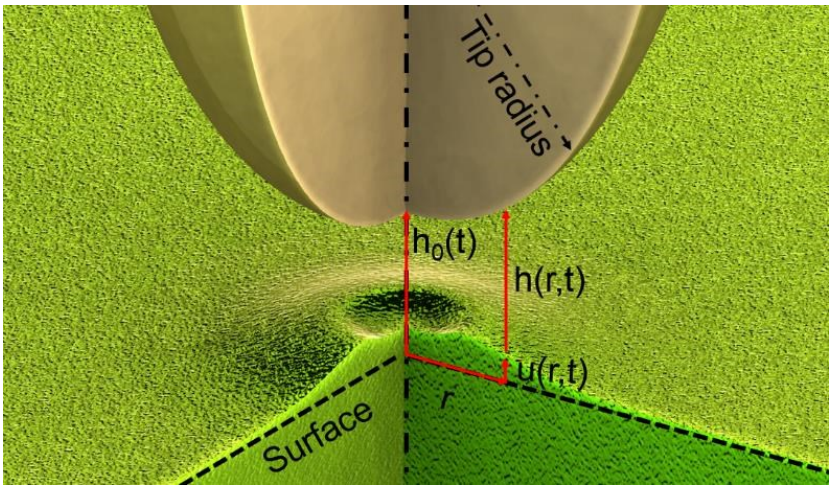

Figure 26. The tip-sample interaction schematic illustrating the parameters used in the model. Dashed lines on the surface represent the surface rest level before the deformation.

To extend Eqn. (47) to tip-surface contact on linear viscoelastic materials, the surface deformation history is accounted for by implementing the correspondence principle on the linear elastic equation as follows:

$$u(\mathbf{r},t)-u(\mathbf{r},t_0)=\int_{t_0}^{t}-\frac{1-\nu^2}{\pi E(t-t')}\int\frac{\dot{p}(h(\mathbf{s},t'))}{|\mathbf{r}-\mathbf{s}|}\,d\mathbf{s}\,dt', \tag{49}$$

where, $\dot{p}(h(\mathbf{r},t))=dp(h(\mathbf{r},t))/dt$ and t_0 is the initial time instant of the computations. Tip position at t_0 is assumed to be far enough from the sample so that the surface is flat and stationary ($u(\mathbf{r},t_0)\approx 0$) and tip-surface interaction is negligible. As seen in Eqn. (49), the deformation of viscoelastic surfaces in a continuum mechanics perspective requires a time integral over its preceding deformation history.

In this work, we choose to model the surface viscoelasticity behavior using the constitutive relationship of a standard linear solid (SLS) whose creep compliance function is defined as:

$$\frac{1}{E(t)}=\frac{1}{E_\infty}+\frac{E_\infty-E_0}{E_\infty E_0}e^{-t/\tau}, \tag{50}$$

where, E_0 and E_∞ are the short and long-term modulus of the surface, $E(t)$ is the effective instantaneous viscoelastic modulus, and τ is the characteristic creep(retardation) time. when is very short or long comparing with the interaction time, the SLS model reduces to the Kelvin-Voigt or Maxwell models, respectively. However, when is chosen to be comparable with interaction time, the SLS model can capture more complex material behavior that none of those models can exhibit.

We calculate the tip-surface pressure between any point on the surface with the tip using a Lennard-Jones (LJ) model of the van der Waals interaction between two infinite parallel surfaces:

$$p(h(\mathbf{r},t)) = \frac{H}{6\pi h(\mathbf{r},t)^3}\left(\frac{{z_0}^6}{h(\mathbf{r},t)^6} - 1\right), \tag{51}$$

where H is the Hamaker constant and z_0 is the equilibrium distance. These two physical parameters, H and z_0 define the work of adhesion which is the reversible thermodynamic work to separate two interfaces from equilibrium state to distance of infinity:

$$W_a = \gamma_1 + \gamma_2 - \gamma_{12} = \frac{H}{16\pi {z_0}^2}, \tag{52}$$

where, γ_1 and γ_2 are surface energies of the two bodies and γ_{12} is the interfacial energy. Attard's calculates the distributed tip-surface pressure ($p(h(\mathbf{r},t))$) as a function of $\mathbf{r}$ using the well-known Derjaguin approximation [134, 135] which applies to smooth convex surfaces that their curvature compared to the gap between interacting bodies is small. The model can accommodate alternative and/or extra surface force models or more sophisticated linear viscoelasticity constitutive models such as the generalized Maxwell model (also known as Prony series) or power-law rheology to capture more complex sample behavior.

SLS model's creep compliance substitution into Eqn. (49) and subsequently, its differentiation respect to time cast the equations in the form of differential equations and remove the time-convolution integral, as follows:

$$\dot{u}(\mathbf{r},t) = -\frac{1}{\tau}\left(u(\mathbf{r},t) - u_\infty(\mathbf{r},t)\right) - \frac{1}{\pi E_{0,s}}\int \frac{\dot{p}(h(\mathbf{s},t'))}{|\mathbf{r}-\mathbf{s}|}\,d\mathbf{s}, \tag{53}$$

$$u_\infty(\mathbf{r},t) = -\frac{1}{\pi E_{\infty,s}}\int \frac{p(h(\mathbf{s},t'))}{|\mathbf{r}-\mathbf{s}|}\,d\mathbf{s}. \tag{54}$$

where, $E_{0,s}$ and $E_{\infty,s}$ are reduced short- and long-term modulus of the sample, respectively:

$$\begin{aligned} E_{0,s} &= \frac{1-\nu^2}{E_0}, \\ E_{0,\infty} &= \frac{1-\nu^2}{E_\infty}, \end{aligned} \tag{55}$$

Due to axisymmetry of the problem, Attard further simplifies the equation by expressing the kernel in terms of the complete elliptic integral of the first kind:

$$\dot{u}(r,t) = -\frac{1}{\tau}\big(u(r,t) - u_{\infty}(r,t)\big) - \frac{1}{E_{0,s}}\int_{0}^{r_d} \dot{p}(h(s,t))\, k(r,s)\, s\, ds\,, \tag{56}$$

$$u_{\infty}(r,t) = -\frac{1}{E_{\infty,s}}\int_{0}^{\infty} p(h(r,t'))\, k(r,s)\, s\, ds\,, \tag{57}$$

where r_d is the computational domain beyond which the tip-sample interaction is considered negligible. $k(r,s)$ is defined as:

$$k(r,s) = \begin{cases} \dfrac{4}{\pi r} K(s^2/r^2) & s < r \\ \dfrac{4}{\pi s} K(r^2/s^2) & r < s \end{cases}, \tag{58}$$

where, K is the complete elliptical integral of the first kind. Since $k(r,s) = k(s,r)$ the k square matrix is symmetric.

4.3 Attard's original computational model:

The equations (47)-(58) and described methodology are identical to the ones suggested by Attard et al. [2, 79, 81]. Introducing radial discretization on Eqn. (56)/(57) yields a set of nonlinear differential equations that each represents the surface deformation rate at the associated radial node specified by radial distance r. Due to concealed $\dot{u}(r,t)$ in $\dot{p}(h(s,t))$ term on the right side of Eqn. (56), the resultant set of ODEs cannot be treated and solved explicitly. Therefore, Attard solves them through iteratively adjusting a guessed $\dot{u}(r,t)$ until the equality between both sides of Eqn. (56) is established. Attard also suggests using forward Euler's method to predict $u(r,t)$ for each time-step based on the calculated $\dot{u}(r,t)$ for preceding time-step. Attard numerically calculates the integrals in Eqn. (56) and (57) using introduced radial nodes as integration points. Simultaneously these nodes are used to reconstruct the deformed surface profile at each time-step and act like degrees of freedom (DOF) of the surface. This bifunctionality of the radial nodes is not computationally efficient since the number of radial discretization for sufficiently accurate integral calculations might not be necessarily the same as the required DOF to render the deformed surface. We will refer to the above-described computational method proposed by Attard as the "iterative" approach.

4.4 Improved computational framework:

Despite the iterative computational approach's output accuracy, it is very sluggish and computationally expensive. To improve the computational part of the model, we first remove the incompetent iterative solution of the model's differential equations. To do so, we expand the rate of pressure change in Eqn. (56) as follows:

$$\dot{p}(h(r,t)) = p'(h(r,t))\,[\dot{h}_0(t) - \dot{u}(r,t)] \tag{59}$$

where $p'(h) = dp/dh$. Then, we substitute Eqn. (59) into Eqn. (56) and rearrange it so that $\dot{u}(r,t)$ terms are all on the left side of the equation, as below:

$$\frac{1}{E_{0,s}} \int_0^{r_d} p'(h(s,t))\,\dot{u}(s,t)\,k(r,s)\,s\,ds - \dot{u}(r,t) = \frac{1}{\tau}\left(u(r,t) - u_\infty(r,t)\right) + \frac{\dot{h}_0(t)}{E_{0,s}} \int_0^{r_d} p'(h(s,t))\,k(r,s)\,s\,ds\,. \tag{60}$$

The result is a set of nonlinear coupled ordinary differential equations with explicit time-dependent forcing through the $\dot{h}_0(t)$ term. Hereafter, this method is referred to as the "explicit" approach in this chapter. Eqn. (60) can be solved by introducing radial and temporal discretization like the iterative approach. Using the explicit approach solution significantly reduces the computational time in comparison with the iterative approach.

Furthermore, we propose a method to optimize the computations speed by separating the dual functionality of the radial nodes in the original contact model. To do so, we apply separation of temporal and radial variables on $u(r,t)$ as follows:

$$u(r,t) = \sum_{i=0}^{n_b} a_i(t)\,f_i(r)\,, \tag{61}$$

where $a_i(t)$ represent the time-dependent coefficients of the radial basis functions and $f_i(r)$ are a complete set of functions that approximate the surface deformation profile at each time-step. Substitution of Eqn. (61) into Eqn. (60) results in a set of differential equations as follows:

$$\sum_{i=0}^{n} \frac{\dot{a}_i(t)}{E_{0,s}} \int_0^{r_d} p'(h(s,t))\, f_i(s)\, k(r,s)\, s\, ds - \sum_{i=0}^{n_b} \dot{a}_i(t)\, f_i(r) = \frac{1}{\tau}\left(\sum_{i=0}^{n_b} a_i(t)\, f_i(r) - u_\infty(r,t) \right) + \frac{\dot{h}_0(t)}{E_{0,s}} \int_0^{r_d} p'(h(s,t))\, k(r,s)\, s\, ds \,. \tag{62}$$

Thus, instead of solving a set of ODEs in Eqn. (60) each associated with a radial element, we solve Eqn. (62) for the time-dependent coefficients, $a_i(t)$, that each associated with a selected radial basis function. The resultant advantage is that the number of basis functions can now be adjusted and optimized independently of the number of radial integral partitions. While almost any complete set of functions can be chosen for $f_i(r)$, an accurate reconstruction of the deformed surface is achieved with smaller n_b if the shape of selected functions resembles the expected deformed surface profiles during an interaction cycle. To further simplify Eqn. (62), we choose $f_i(r)$ to be a complete biorthogonal set of functions. Since the problem is axisymmetric, we only consider the even terms of selected basis functions. Then, we multiply both sides of Eqn. (62) with $f_j(r)$ and integrate over $(0, r_d)$ to utilize the terms biorthogonality to simplify the resultant equation:

$$\sum_{i=0}^{n_b} \frac{\dot{a}_i(t)}{E_{0,s}} \int_0^{r_d} p'(h(s,t))\, f_i(s)\, s\, \rho_j(s)\, ds - \dot{a}_j(t)\, \zeta_j = \frac{a_j(t)}{\tau}\, \zeta_j + \frac{1}{\tau\, E_{\infty,s}} \int_0^{r_d} p(h(s,t))\, s\, \rho_j(s)\, ds + \frac{\dot{h}_0(t)}{E_{0,s}} \int_0^{r_d} p'(h(s,t))\, s\, \rho_j(s)\, ds \,, \tag{63}$$

$$\rho_j(s) = \int_0^{r_d} f_j(r)\, k(r,s)\, dr \,, \tag{64}$$

$$\zeta_j = \int_0^{r_d} f_j(r)^2 dr \,, \tag{65}$$

where, i and j are integer numbers between 0 to n_b. $\rho_j(s)$ and ζ_j are time-independent variables and hence, are not required to be calculated for each time-step. We rearrange Eqn. (63) into a matrix representation and introduce temporal discretization as follows:

$$\dot{a}_i(t_q) = J_{ij}^{-1}\, b_j \,, \tag{66}$$

$$J_{ij} = \frac{1}{E_0}\int_0^{r_d} p'(h(s,t_q))\, f_i(s)\, s\, \rho_j(s)\, ds - \delta_{ij} \times \zeta_j \,, \tag{67}$$

$$b_j = \frac{a_j(t)}{\tau}\,\zeta_j + \frac{1}{\tau\, E_{\infty,s}}\int_0^{r_d} p(h(s,t))\, s\, \rho_j(s)\, ds + \frac{\dot{h}_0(t)}{E_{0,s}}\int_0^{r_d} p'(h(s,t))\, s\, \rho_j(s)\, ds \,, \tag{68}$$

where, δ_{ij} is the Kronecker delta. We use the Riemann approach to calculate the integrals for the simulations in this chapter. Solving the set of nonlinear ODEs for time-step t_q yields the set of associated $\dot{a}_i(t_q)$ coefficient rates. Then, Eqn. (61) reconstructs the deformed surface profile at each time-step. This allows for the explicit computation of $u(r,t)$ and thus $h(r,t)$ and consequently $p\big(h(r,t)\big)$. The tip-surface interaction force, $F_{ts}(t)$, for each time-step is calculated as follows:

$$F_{ts}(t) = 2\pi \int_0^{r_d} p(h(r,t)\, r\, dr \,. \tag{69}$$

To evaluate and optimize the performance of the proposed computational approach, we studied an alternative way of implementing the approximating basis functions. In this scenario, we express the tip-surface distance $h(r,t)$ in terms of a complete set of biorthogonal radial basis functions, as follows:

$$h(r,t) = \sum_{i=0}^{n_b} a_i(t)\, f_i(r) \,. \tag{70}$$

The implementation process for Eqn. (70) is similar to the previously explained procedure.

4.5 Computational Stability

In cases where the selected model to calculate $p(h(r,t))$ switches between attractive and repulsive forces depending on the gap between interacting bodies, the Attard's model computations may become unstable. As illustrated in Figure 27-b, the computational instability occurs when the surface undergoes rapid non-equilibrium movements during the interaction cycle, specifically during snap-in or off surface processes for which the model predicts large $\dot{u}(r,t_q)$. Attard suggests using forward Euler's method to project $u(r,t_{q+1})$ at each time-step based on the calculated $\dot{u}(r,t_q)$ for previous time-step [2]:

$$u(r,t_{q+1}) = u(r,t_q) + dt \times \dot{u}(r,t_q)\,, \tag{71}$$

where "dt" is the infinitesimal time interval between time-steps. Using forward Euler's method, the projected $u(r,t_{q+1})$ is directly proportional to $\dot{u}(r,t_q)$ of the proceeding time-step. Therefore, when $\dot{u}(r,t_q)$ is very large, it may lead to discontinuities in the reconstructed deformed surface profile and resultant computational instabilities. This may happen due to surface deformation instabilities during interaction time such as snap-in and/or snap-off instances when the tip approaches or retracts off the surface, respectively, especially on highly soft and sticky surfaces. To alleviate this issue, we employed the generalized Euler's method to establish a more controlled link between $u(r,t)$ at each time-step and $\dot{u}(r,t)$ of the proceeding time-steps:

$$u(r,t_{q+1}) = u(r,t_q) + dt \times \sum_{i=0}^{n_E} a_i \times \dot{u}(r,t_{q-i})\,, \tag{72}$$

where, as per definition the rate coefficients must satisfy this condition: $\sum_{i=0}^{n_E} a_i = 1$.

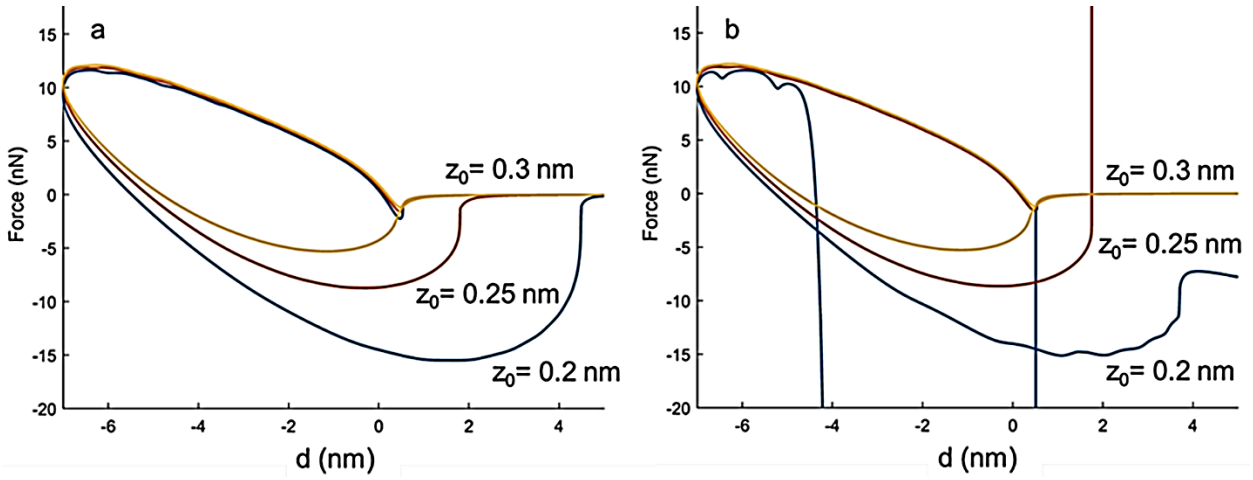

Figure 27. Computational stability improvements by employing generalized Euler's method (Eqn. (72)) with (a): $n_E = 1$ in comparison with (b): forward Euler's method. The rigid tip oscillates through a sinusoidal wave and interacts with the LDPE surface as characterized in Table 8. All the employed simulation parameters for (a) and (b) are identical to enable robustness comparison. The surface adhesion level is regulated by employing various z_0 which are mentioned in the figures.

To visualize the achieved computational stability enhancement, we used the generalized Euler's method (Eqn. (72)) with two different number of terms: $n_E = 0$ (forward Euler's method) and $n_E = 1$ to predict a single force-distance (F-d) curve when a rigid tip oscillating through a sinusoidal wave interacts with a low-density polyethylene (LDPE) sample as characterized in Table 8. We regulated the adhesion of the surface by decreasing z_0 in the LJ pressure equation (Eqn. (51)) to study when computational instabilities arise. As illustrated in Figure 27, generalized Euler's method implementation stabilizes the computations in comparison with forward Euler's method. We name the described method as formulated by Eqn. (17)-(19) combined with Eqn. (72) as "enhanced Attard's model" (EAM).

Table 8. The employed values for LJ pressure and surface viscoelasticity properties for LDPE in the conducted simulations. H, z_0, ν, E_0, E_∞, and τ are Hamaker constant, equilibrium distance, Poisson's ratio, short-term modulus, Long-term modulus, and creep time, respectively. The tip radius in these simulations is set to be 10 nm.

H (J)	z_0 (nm)	ν	E_0 (GPa)	E_∞ (GPa)	τ (sec)
1×10^{-19}	0.25	0.49	2	0.1	1×10^{-7}

4.6 EAM Verification

To verify EAM and assure the reliability of the developed code, we compare EAM predicted F-d curves for a prescribed triangular tip motion with the ones presented in Attard's original work [2]. In this set of simulations, the paraboloid tip has a radius of $10\,\mu m$ which oscillates through a triangular wave between $h_0 = 10\,nm$ and $h_0 = -10\,nm$. The employed material properties and interaction parameters are: $E_0 = 10\,GPa$, $E_\infty = 1\,GPa$, $H = 10^{-19}\,J$, $z_0 = 0.5\,nm$, and $\tau = 1\,ms$. The sample and tip movement parameters are identical with the ones used in the original work to enable comparing the results. The number of temporal discretization points and employed cosine basis functions to reconstruct the deformed surface are 10^4 and 250, respectively. the short/ long time Young's modulus of the sample (E_0 / E_∞) are 10/ 1 GPa, respectively. Hamaker constant, H, is 10^{-19} J and the equilibrium position, z_0, is 0.5 nm. The rigid

tip oscillates between 10 and −10 nm through a triangular waveform with an abrupt velocity change. The characteristic relaxation time for the creep function (retardation time) is 1 ms.

The results are checked to be independent of the number of employed temporal and radial discretization. The employed surface and interaction parameters except tip velocities are identical in all Figure 28 simulations. The variation of predicted F-d curves indicates the velocity dependency of the model when interacting with a viscoelastic surface. Figure 28 illustrates an excellent agreement between the original Attard's model and EAM predictions.

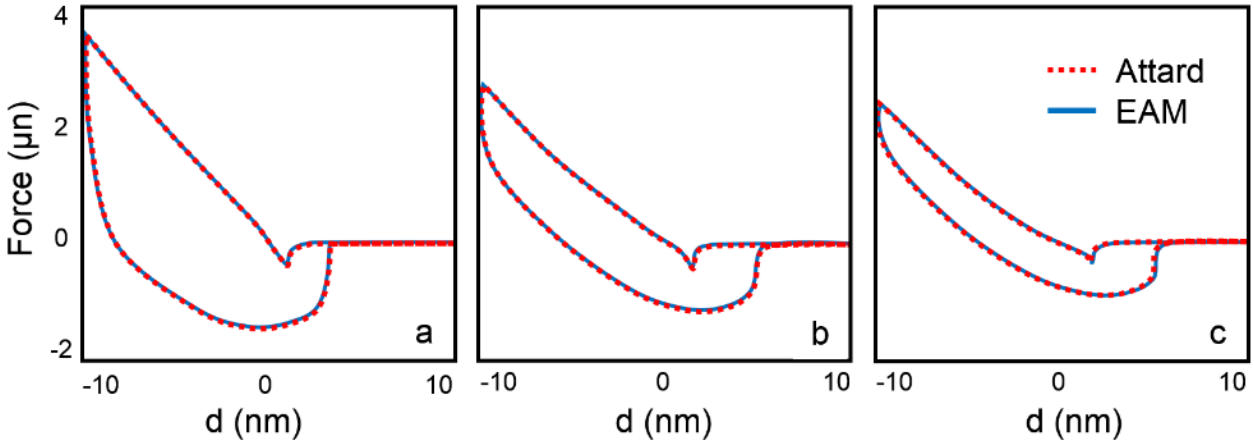

Figure 28. The interaction between a rigid axisymmetric paraboloid tip oscillating through a prescribed triangular wave and a viscoelastic surface is simulated using EAM. The triangular excitation velocities are (a) $\pm 5\ \mu m/s$, (b) $\pm 2\ \mu m/s$, and (c) $\pm 1\ \mu m/s$. The employed material and interaction parameters are identical with the ones used by Attard[2] to facilitate comparison.

4.7 EAM performance

We simulate tip-surface interaction in amplitude-modulation AFM (AM-AFM) on an LDPE sample using various configurations of EAM to evaluate, compare, and optimize their output computational accuracy. We assume tip oscillation is steady-state and sinusoidal in AM-AFM which is a reasonable approximation when the operation is performed in air/vacuum [86]: $q(t) = A\sin(\omega t - \phi)$, where q and t are the tip deflection and time, and A, ω, and ϕ are the steady-state amplitude of oscillation, excitation frequency, and phase lag relative to excitation force, respectively. Since the output computational error of "iterative" and "explicit" approaches can be minimized by employing a proper number of radial and temporal discretization, we consider them as "exact" solutions. EAM simulations converge to exact predictions if a sufficient number of basis functions (n_b in Eqn. (61)) are employed. To quantify the convergence of EAM solutions,

we use virial (V_{ts}) and energy dissipation (E_{ts}) values of a single AM-AFM force history on an LDPE sample:

$$V_{ts} = \frac{1}{T}\int_0^T F_{ts}(t)\, q(t)\, dt\,, \tag{73}$$

$$E_{ts} = -\int_0^T F_{ts}(t)\, \dot{q}(t)\, dt\,, \tag{74}$$

where $\dot{q}(t)$ is the tip velocity and T is the period of a single oscillation cycle.

Table 9. The convergence rate of these EAM implementation setups is evaluated to realize the optimized configuration.

#	Radial disc.	Solution type of nonlinear diff. eq. set	Basis function	Approximated parameter	Orthogonality implementation
A	Yes	Iterative	NA	NA	NA
B	Yes	Explicit	NA	NA	NA
C	No	Explicit	Fourier	$u(r,t)$	No
D	No	Explicit	Fourier	$h(r,t)$	No
E	No	Explicit	Fourier	$u(r,t)$	Yes
F	No	Explicit	Fourier	$h(r,t)$	Yes
G	No	Explicit	Bessel first kind	$u(r,t)$	Yes

V_{ts} and E_{ts} are commonly used parameters to quantify AM-AFM and represent the conservative and non-conservative part of the interaction energy during tip-surface contact [1]. The utilized LDPE properties and the employed EAM setups are listed in Table 8 and Table 9, respectively. Typical calibration values of Olympus AC160-R3 microcantilevers are used in these simulations: $f = 278\,\text{kHz}$, $k = 28.1\,\text{N/m}$, and $Q = 430$, where f, k, and Q are the excitation frequency, equivalent stiffness, and quality factor of the microcantilever. The free amplitude, A_0, is 62 nm and the amplitude setpoint is 0.8 for these simulations. Setups 'C' and 'E'/'G' are computed using Eqn. (62) and Eqn. (63), respectively and setups 'D' and 'F' refer to employing Fourier expansion basis functions to approximate $h(r,t)$ instead of $u(r,t)$. All solutions are

checked to be independent of the selected domain and temporal discretization values. Since the problem is assumed to be axisymmetric, only the even terms of the employed basis functions are considered. The number of the employed basis functions are in the range of 0 to 56. The convergence of the EAM configurations is appraised using the exact solutions ('A' and 'B') [1, 2, 79] and the associated energy errors are expressed as a percentage. We considered the 1% error on both V_{ts} and E_{ts} parameters as the convergence threshold and we determined the convergence when this criterion is met constantly beyond a specific n_b. The number of the time discretization is identical for all simulations $\left(10^4\right)$ and the number of radial discretization for exact computational methods is 70.

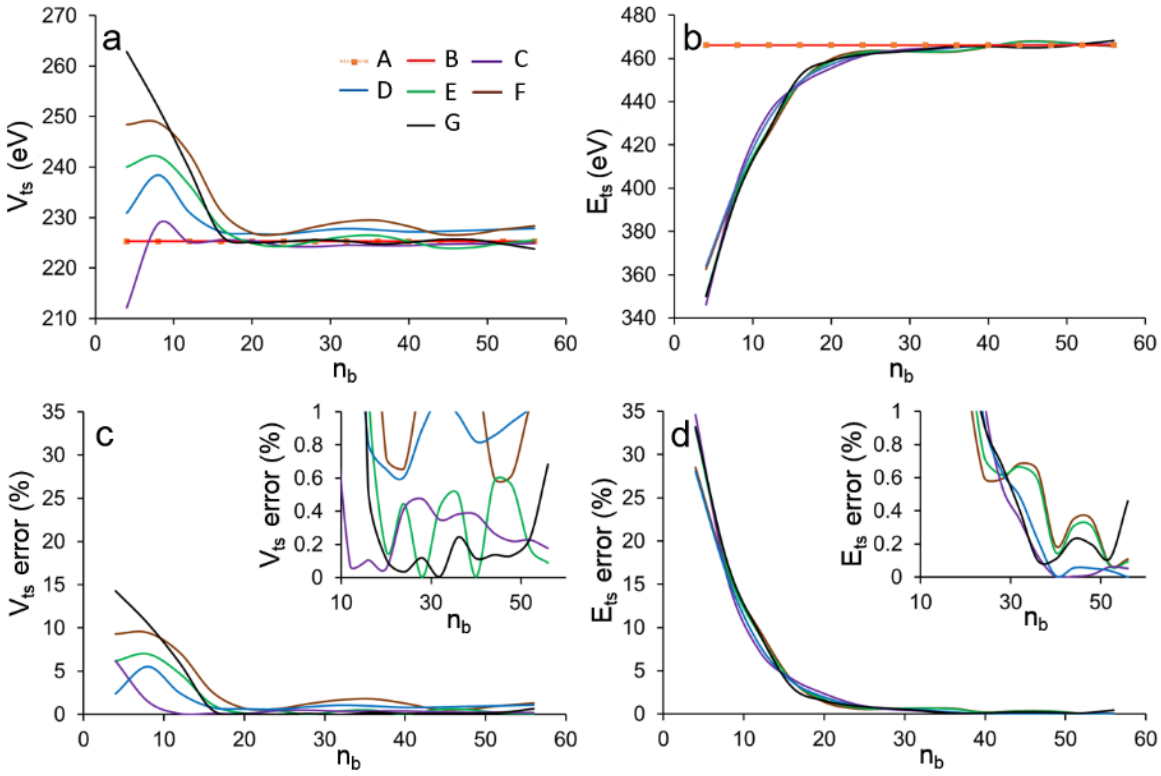

Figure 29. Comparison of the convergence performance of different configurations of EAM implementation as listed in Table 9. The graphs are color-coded according to legends of graph 'a' and the labels defined in Table 9. The insets of the second-row graphs are intended to envision 1% error criteria of the energy parameters with respect to exact solutions.

The results illustrated in Figure 29 (a-b) show that V_{ts} and E_{ts} of the considered EAM setups gradually converge to the associated exact values by increasing n_b. Figure 29 (c-d) depicts the percentage error of each of these setups and the insets are intended to assist in realizing the specific n_b beyond which the 1% error threshold for convergence is met. Figure 29 (c) shows that the Fourier basis function's implementation leads to a more optimized V_{ts} convergence when used to approximate $u(r,t)$ (setups 'C' and 'E') than $h(r,t)$ (setups 'D' and 'F'). Moreover, Figure 29 (d) shows that in terms of E_{ts} convergence, the ones with biorthogonality implementation (setups 'E' and 'F') converge in slightly smaller n_b numbers than others. Figure 29(a and b) illustrate a faster convergence for V_{ts} than E_{ts}. We visualized this on predicted F-d histories as shown in Figure 30. In this graph, F-d history predictions by configuration 'E' when n_b increases from 0 to values specified in the legend are illustrated. When $n_b = 0$, the surface deformation is characterized by a sole function of time: $u(r,t) = u(t) = a_0(t)$. The force history predictions gradually converge to the exact solution and do not visually seem to vary significantly beyond $n_b = 20$. The repulsive phase of the force history converges faster to the exact solutions than the attractive phase. It means that EAM prioritizes the reconstruction of the more effective and central parts of the deformed profile earlier than the outer regions of the contact area.

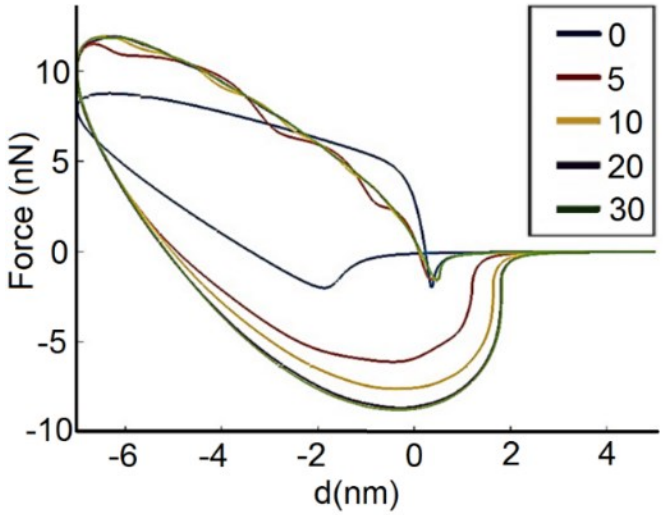

Figure 30. Visualization of F-d history convergence to the exact solution by increasing the number of employed basis functions (n_b). The surface and LJ interaction parameters are listed in Table 8.

The time elapsed to compute a single tip-sample interaction cycle when using the setups listed in Table 9 is compared in Figure 31. The significant difference between iterative ('A') and other computational approaches depicts the considerable enhancement achieved through the applied strategies. Furthermore, the setups with biorthogonal basis functions (Setups 'E', 'F', and 'G') which enjoy a further simplified formalism (Eqn.s (66)-(68)) lead to faster computations (Figure 31). The Bessel set of basis functions ('G') despite the acceptable convergence rate, is slower than Fourier ones due to the intrinsic computational complexity of the Bessel functions and their orthogonality implementation. Figure 31 illustrates that in terms of the computational time, EAM can outperform the "explicit" approach with a far fewer number of employed basis functions in EAM than the number of the implemented radial discretization in the "explicit" approach.

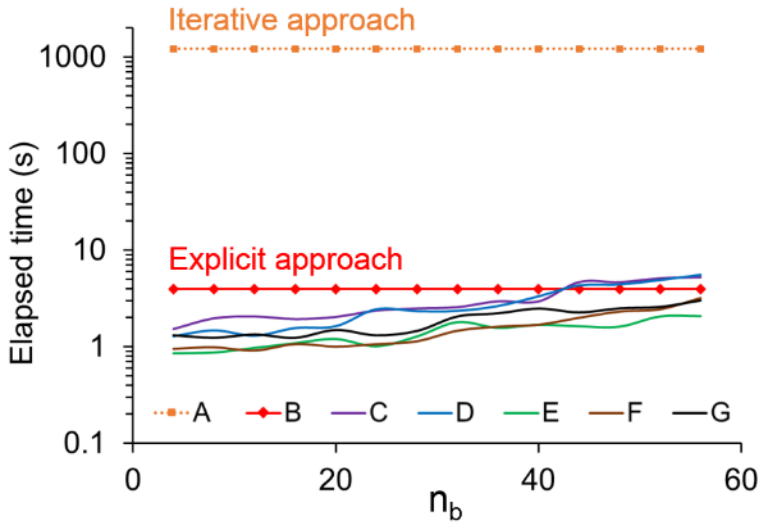

Figure 31. Elapsed time to compute a tip-surface interaction cycle using different EAM configurations as listed in Table 9. The labels in the legend are defined in the first column of Table 9. The surface and interaction parameters are listed in Table 8. It shows the computational rate of EAM is about three orders of magnitude faster than the original iterative approach proposed by Attard[2, 79]. All simulations are carried out on a typical desktop computer.

Considering both results in Figure 29 and Figure 31, amongst the evaluated EAM setups the tip-sample interaction phenomenon is most efficiently computed by EAM when the surface deformation is approximated by cosine terms of Fourier expansion as formulated in Eqn. (66)-(68) (setup 'E'). Hereafter, we only employ this configuration to carry out EAM simulations in this chapter. Observing 1% virial and dissipation energy values error as the convergence criterion, the

number of required basis functions (n_b) to approximate $u(r,t)$ is ~24 for this set of the input parameters.

4.8 AFM Simulations using EAM

EAM is a fast first-principles approach that can make reliable predictions when studying the interaction with viscoelastic and/or adhesive surfaces. The achieved improvements facilitate the inclusion of EAM into simulations of various AFM modes of operation. In this chapter, first, we use an algorithm to embed EAM into the AFM force spectroscopy simulations on soft polymer samples. AFM force spectroscopy is commonly used to study the surface mechanical properties [136-138]. In AFM force spectroscopy the microcantilever due to the Z-piezo expansion approaches the surface, snaps into the surface, indents into the sample until it reaches the defined setpoint, and then withdraws back to its initial state. The schematics and used parameters are shown in Figure 32. Interaction force is inferred from q(t) using the microcantilever equivalent stiffness (k) which is determined by calibration of the AFM microcantilever.

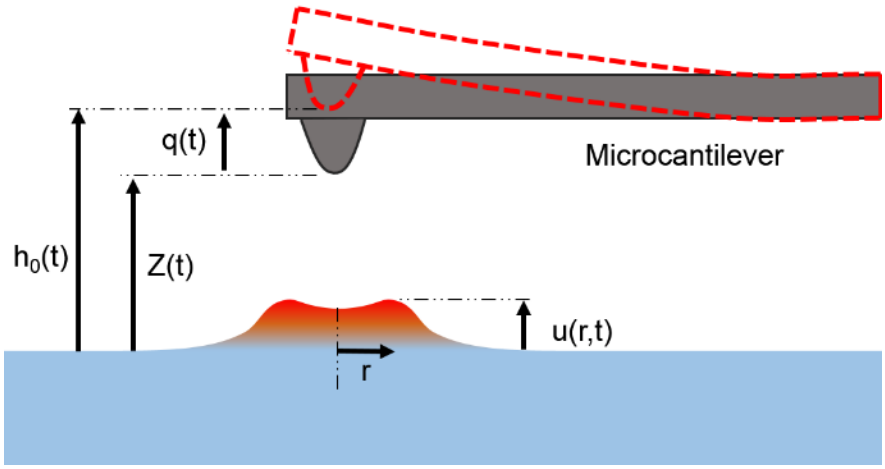

Figure 32. AFM force spectroscopy schematics and used parameters. In this mode, the input signal to Z-piezo prescribes the defined Z motion. The microcantilever moves toward the surface, indents, and then retracts as it reaches the defined force setpoint. Tip and surface parameters are shown in Figure 26.

The tip trajectory in AFM force spectroscopy with respect to the unperturbed surface level, $h_0(t) = Z(t) + q(t)$, is not known *a priori*. Therefore, we need an algorithm to enable embedding EAM into the force spectroscopy framework. The quasi-static force curves are conducted in low

and off-resonance frequencies. Besides, we assume the microcantilever deflections are small enough so that it acts as a linear spring with equivalent stiffness k. Therefore, the designed algorithm iteratively determines q(t) at each time-step so that the quasi-static solution holds:

$$q(t) = F_{ts}(t) \,/\, k \tag{75}$$

The transient microcantilever responses such as the ringing effect which occur experimentally are not captured due to the quasi-static solution assumption. We applied the algorithm to simulate an AFM force spectroscopy on an LDPE sample with viscoelasticity and LJ pressure parameters as specified in Table 8 except $\tau = 0.01\,\text{ms}$. In this simulation, the microcantilever equivalent stiffness is 28.1 N/m and the microcantilever base travels through a triangular wave with 1 Hz frequency and 50 nm amplitude.

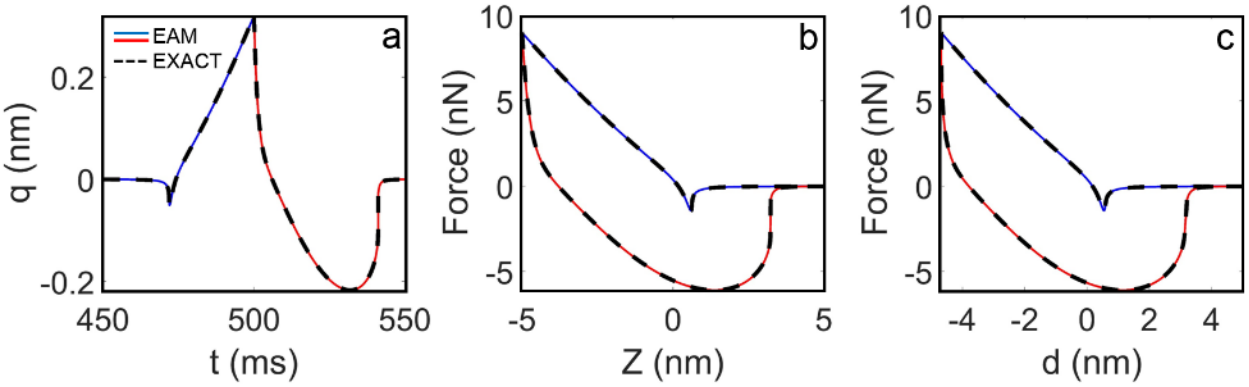

Figure 33. Study the surface-microcantilever ensemble dynamics in AFM force spectroscopy. (a) shows the predicted microcantilever deflection during one oscillation cycle. (b) and (c) illustrate the predicted F-Z and F-d curves, respectively. The blue and red solid lines represent the approach and retraction branches of the force curve computed using EAM with $n_b = 25$, respectively. The dashed black line is computed using the explicit approach.

The results shown in Figure 33 illustrate the model's ability to well capture the surface instabilities both when approaching and retracting the surface. During retraction, the adhered surface to the tip gradually peels away until the adhesive forces again dominate and the microcantilever deflects downward (negative force). This will lead to a hysteretic loop in which the long-range surface forces may significantly contribute to the resultant energy dissipation. The whole cycle computation took less than a minute to complete using a typical desktop computer as compared to ≈ 12 hours of the original Attard's model.

Table 10. The employed values for LJ pressure and surface viscoelasticity properties for polystyrene (PS) in the conducted simulations. The tip radius in these simulations is set to be 50 nm.

H (J)	z_0 (nm)	ν	E_0 (GPa)	E_∞ (GPa)	τ (sec)
2×10^{-20}	0.15	0.35	4.25	1.89	1×10^{-7}

Next, an AM-AFM approach/retract curve on a polystyrene (PS) surface with viscoelasticity and adhesive properties as specified in Table 10 is simulated. To do so, we used an energy balance based algorithm[1] employing the amplitude reduction formula:

$$A^{ratio} = \frac{1/Q}{\sqrt{\left(\frac{-2V_{ts}}{kA^2}\right)^2 + \left(\frac{1}{Q} + \frac{E_{ts}}{\pi kA^2}\right)^2}} \tag{76}$$

where, A^{ratio} and A are the amplitude setpoint and tip oscillation amplitude, respectively. We calculated E_{ts}, V_{ts}, and ϕ as a function of A^{ratio} as shown in Figure 34. Elapsed time to complete simulations for the approach curve with $n_b = 25$ which meets the 1% V_{ts} and E_{ts} error threshold, is about a minute using a typical desktop computer as compared to ≈ 15 hours taken by the original Attard's model. The results are checked to be independent of the computational domain selection and temporal discretization.

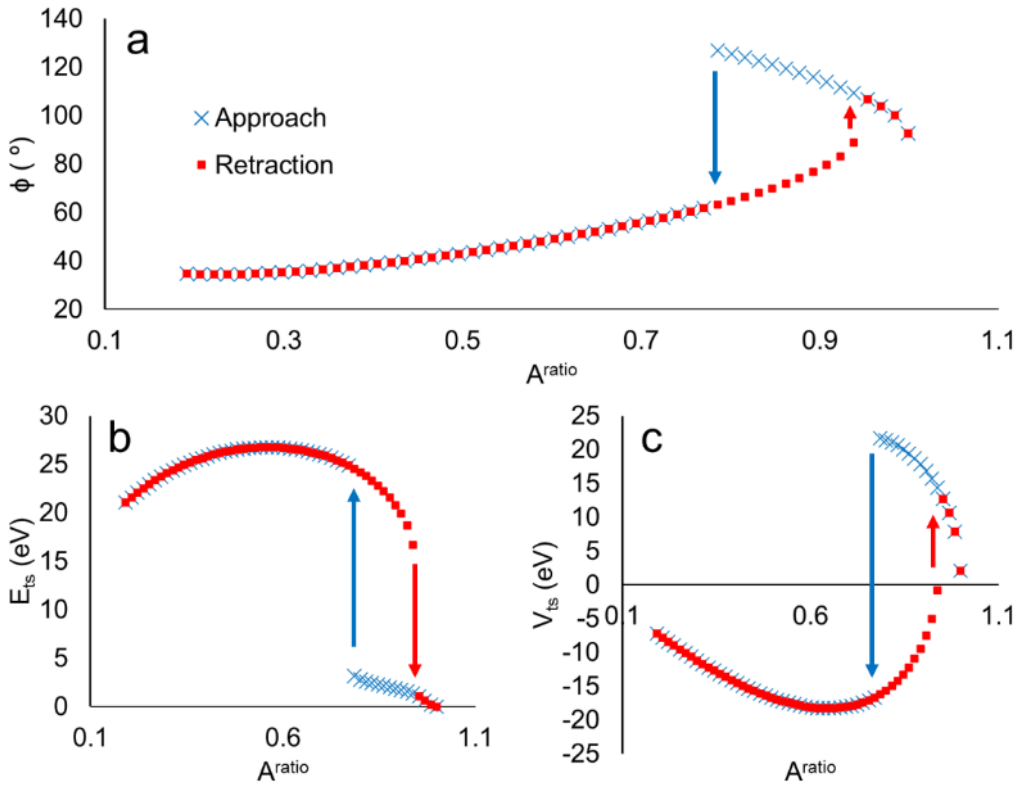

Figure 34. Computed (a): Phase lag (ϕ), (b): Energy dissipation (E_{ts}), and (c): virial (V_{ts}) od AM-AFM dynamic approach/retract curves on an LDPE sample. In these simulations $u(r,t)$ is approximated according to Eqn. (61) with $n_b = 25$. The employed A_0, f, Q, and k are 15 nm, 278 kHz, 429.5, and 28.1 N/m, respectively. The results are in excellent agreement with exact solutions.

The hysteretic approach-retraction branches in Figure 34 demonstrate the co-existence of both repulsive and attractive regimes in a range of A^{ratio}'s. The predicted dissipation in the repulsive regime follows the same trend previously predicted [88]. However, the method is uniquely capable of calculating the viscoelastic and adhesive dissipation in the attractive regime of AM-AFM operation. This can facilitate the visco-nanomechanics of soft, adhesive, and viscoelastic surfaces in an attractive regime using AFM modes. This is particularly helpful for sticky and/or highly delicate samples for which imaging in the repulsive regime is challenging and/or sample is susceptible to damage with forces in the repulsive regime.

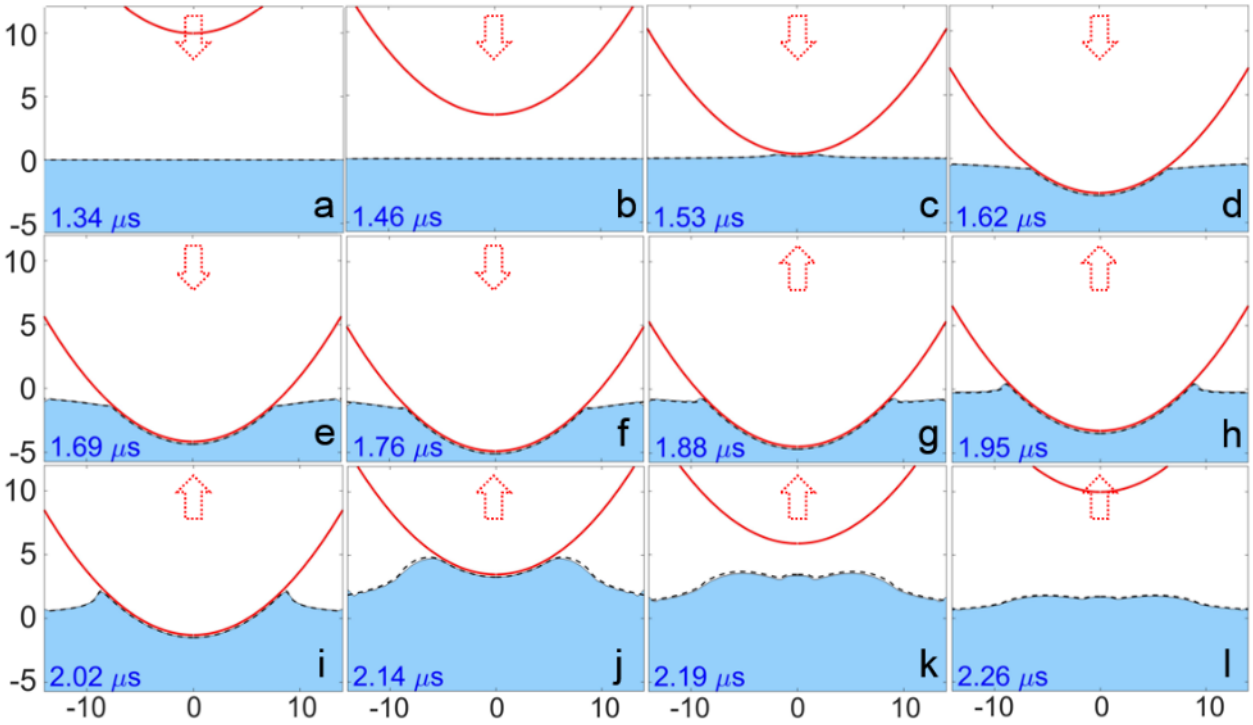

Figure 35. The tip-surface interaction in a single cycle of AM-AFM on the LDPE surface in the time domain as predicted by EAM (blue area) and exact (dashed black line) approaches. The surface characteristic parameters are listed in Table 8. The instant associated with each of the images is noted at the left-down of each picture. a-f and g-l image series illustrate the approach and retraction parts of the cycle, respectively. The arrows are to assist in realizing the tip velocity direction. The frame dimensions are in nm.

Finally, we visualized the tip-surface interaction in a single cycle of AM-AFM on an LDPE sample as characterized in Table 8. A series of figures illustrating the tip position and surface geometry at different time-steps are shown in Figure 35. The full video is provided in the supporting information. The finite-range attractive tip-surface forces cause the surface to deform slightly toward the approaching tip (Figure 35-c). When retracting, the soft, relaxed surface forms a meniscus around the tip profile and progressively detaches until it completely peels off and continues to gradually return to its initial state (Figure 35-g to i). Surface attractive forces cause the contact radius during retraction to become larger than the one during the approach. The unique model predictions of the tip-surface interaction phenomena qualitatively match well with in-situ experimental observations by confocal imaging of polymers during indentation [139].

4.9 Conclusion

This works features an approach to enhance the computational part of Attard's continuum mechanics viscoelasticity contact model. The enhancements implemented in 3 directions: 1) The model's formalism is optimized to enable the explicit solution of the model's governing differential equations, 2) Instead of using radial discretization, the deformed surface is reconstructed using a complete set of basis functions, 3) instead of forward Euler's method, higher-order numerical procedures are employed to solve the model's ordinary differential equations. By implementing the enhancements, EAM is more than three orders of magnitude faster than the originally proposed computational model. Furthermore, the enhancements improve the computational stability of the model to better tolerate the surface nonequilibrium movements. EAM is a fast first-principles viscoelasticity model that is versatile in terms of the inclusion of various tip-surface interaction forces and surface linear viscoelasticity models. EAM was implemented within the AFM framework to predict force spectroscopy observables and dynamic approach/retract curves by AM-AFM. Moreover, we used EAM to calculate the time-resolved surface dynamics during a single tip-surface interaction cycle of AM-AFM. The excellent agreement between EAM simulation results and the ones by exact approaches verifies the accuracy of the developed approach. The achieved excellent accuracy and quick computations by EAM, facilitate making accurate and reliable predictions for AFM operations especially on soft, adhesive, and viscoelastic surfaces.

5. MECHANICAL PROPERTIES CHARACTERIZATION OF SOFT POLYMERS WITH SURFACE FORCES USING PEAKFORCE TAPPING AFM – A MACHINE-LEARNING APPROACH

5.1 Introduction

The atomic force microscopy (AFM) modes that can measure or reconstruct the complete tip-surface interaction force curves are widely used set of techniques to estimate the nanoscale mechanical properties of polymers. The variation of tip-surface interaction force with respect to the instantaneous tip-surface distance can either be represented as F vs. d, F vs. Z, or F vs time (t) curves, where d and Z are demonstrated in Figure 36-a. Classical force volume mapping (FVM) [11], PeakForce Tapping (PFT) [140], quantitative imaging (QI) [141], tapping mode AFM (TM) [9], and Fast Force Mapping (FFM) [142] are examples of various AFM modes that outputs the force curves at each probed point on the surface. These modes differ in terms of the utilized excitation frequency, the acquisition speed, designed control loops, and provided observables[141-143] and can be classified into two main categories: 1- On-resonance modes, at which the excitation frequency coincides or overlaps the bandwidth of usually the first eigenfrequency of the microcantilever, ω. In this category of AFM modes, a force reconstruction process is required to link the mode observables to the associated F-d curve at each image pixel [144]. 2- Sub-resonance modes, at which the excitation frequency is usually well below the fundamental frequency of the microcantilever to avoid complexities associated with the cantilever resonance and its harmonics [145]. In sub-resonance modes, the base of the microcantilever is excited through an oscillatory waveform (triangular, sinusoidal, or other) at ω_Z frequency. The tip deflection, q(t), is monitored and recorded in real-time and transformed to tip-surface interaction force, F_{ts}. The steady-state correlation between q(t) and F_{ts} is established by the quasi-static solution of the force spectroscopy that can be represented as an equivalent mass-spring model as demonstrated in Figure 36-b [146]. At each image pixel, a control loop adjusts Z to maintain the mode setpoint which is usually the maximum interaction force during imaging. This allows the extraction of the topography of the surface as well as acquiring F-d curves at each image pixel. The scanning speed with these modes is generally slower than the resonant modes and is proportional to the resonance frequency of the employed microcantilever, ω_Z, and the time constant of the instrument's lock-in amplifiers.

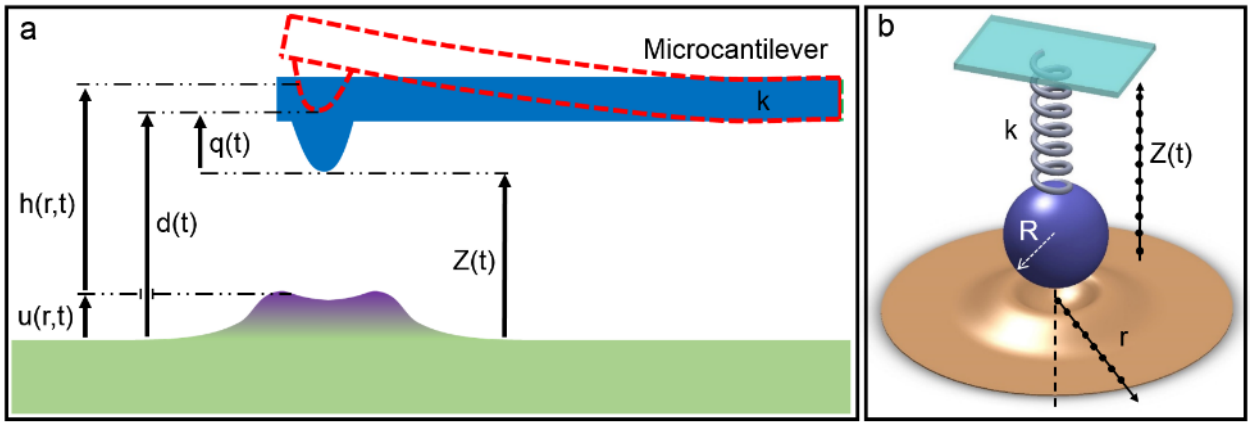

Figure 36. (a) Schematics of an interacting AFM microcantilever tip and a surface. The relevant parameters characterizing the tip-surface distance, tip deflection, and surface deformation are labeled and shown in the image. (b) The equivalent point-mass model representation for the uniform and rectangular microcantilever excited at a sub-resonant frequency.

In Bruker PFT AFM a sinusoidal waveform is used to modulate Z [143]. The prescribed Z(t) in PFT AFM can be expressed as follows:

$$Z(t) = Z + A_Z \cos(\omega_Z t), \tag{77}$$

where, A_Z is the Z oscillation amplitude and $\omega_Z = 2\pi f_Z \ll \omega$. The smooth and continuous sinusoidal Z velocity profile prevents artifacts due to piezoelectric tube oscillation that originates from the velocity profile discontinuity common in triangular Z modulation. Furthermore, this change reduces issues associated with dynamic mechanical coupling between harmonics of the triangular wave and the AFM instrument compartments. The improvements of PFT AFM compared to prior approaches enable the simultaneous topography mapping and force curves acquisition at a higher imaging speed, higher pixel resolution, and with better peak force control. The schematic shown in Figure 37 demonstrates various possible tip deflection and surface deformation during a PFT AFM cycle on a polymeric surface. When the retracting tip becomes fully detached from the surface, the microcantilever starts ringing freely without interacting with the surface. This high-frequency segment of the output signal is filtered out in PFT mode through averaging over a set of force curves at each image pixel and the use of denoising algorithms. However, despite the experimental advances, there is not yet a comprehensive, reliable, and rigorous method to quantitatively link the acquired F-d curves by PFT or other similar AFM modes for each pixel to the nanoscale mechanical properties of soft, viscoelastic, and adhesive polymers.

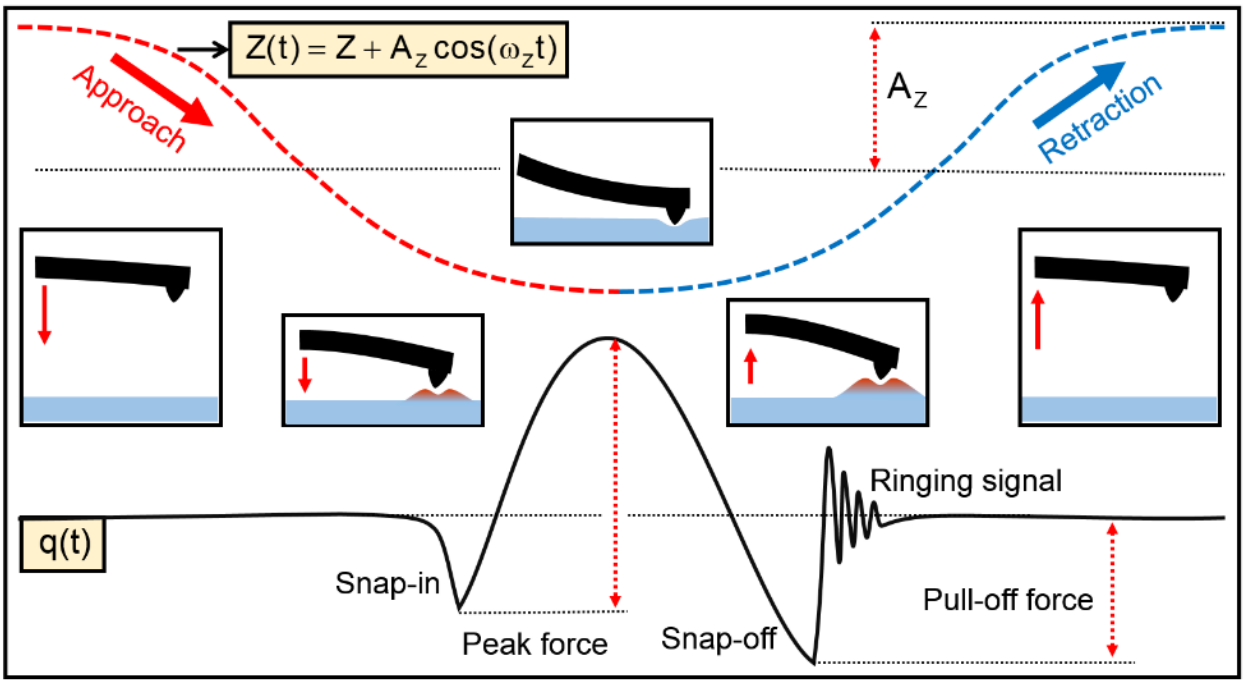

Figure 37. Schematic of PFT AFM on a soft sample. The dashed red-blue curve shows the trajectory of the microcantilever base during a cycle (Eqn. (77)). The black solid curve represents the tip deflection (q) during a cycle. The transient ringing signal of the retracting microcantilever occurs when the tip becomes fully detached from the surface. This part of the force curve is usually filtered out in PFT mode.

In this work, we first develop a forward solution algorithm to predict the PFT force curves based on the material viscoelastic and adhesive properties. The proposed algorithm can be adapted for the similar sub-resonance modes introduced by other AFM manufacturers. The algorithm enables the inclusion of EAM into the forward simulation of the microcantilever and sample responses. We validate the proposed algorithm by comparing it with Attard's original work [2] and with FE simulations. The validated algorithm is employed to conduct a parametric study that varies AFM operational parameters, microcantilever properties, and surface properties. In the second part of the work, we examine using a regression-based machine learning (ML) algorithm to tackle the inverse part of the problem and estimate the viscoelastic and adhesive properties of the sample based on a given force curve. We use the forward solution algorithm on a vast range of known input parameters selected by the Latin hypercube sampling method[120] to generate the required training dataset for the ML algorithm. The adhesive and viscoelastic properties of the studied polymeric surfaces are modeled by Lennard Jones pressure and standard linear solid (SLS) viscoelastic constitutive model, respectively.

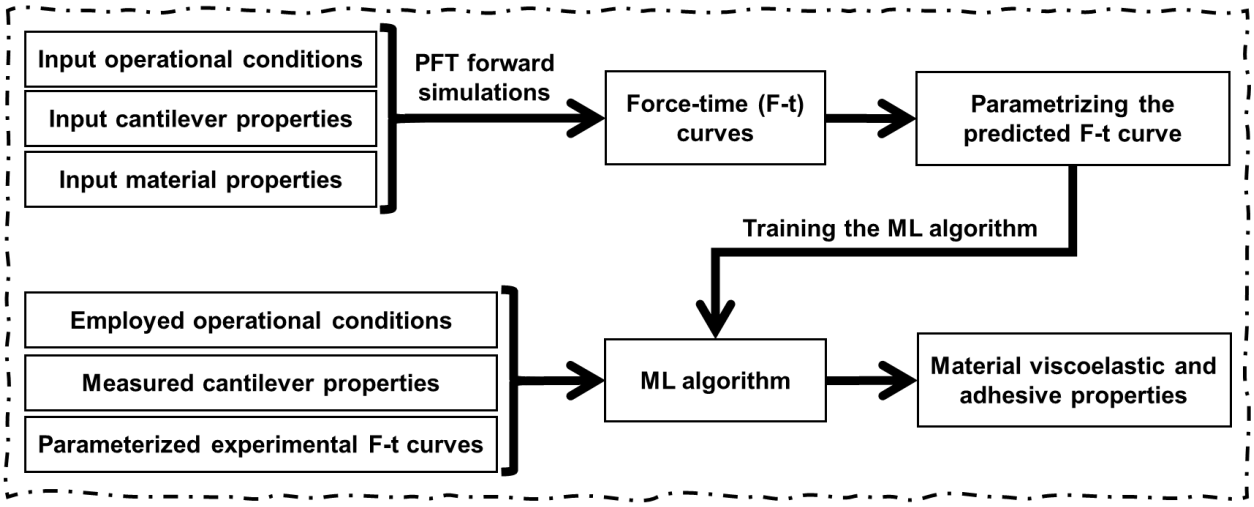

Figure 38. The flowchart illustrates the two-step method used to estimate the material viscoelastic and adhesive properties based on an experimentally acquired PFT F-t curve. The procedure employs a machine learning algorithm that is trained by a dataset of forward simulation results.

5.2 Theory

In PFT AFM, the interaction between the tip of a microcantilever and a surface is monitored and recorded while the Z distance of the microcantilever is modulated by a sinusoidal waveform. The absolute deflection of the microcantilever at distance x from the base of the microcantilever and at time t, $w(x,t)$, is composed of two components: $Z(t)$ which is the prescribed Z-piezo motion, and $u(x,t)$ which is the transverse deflection of the beam in the non-inertial frame attached to the base:

$$w(x,t) = Z(t) + u(x,t). \tag{78}$$

We model the deflection of the microcantilever in PFT AFM with partial differential equations (PDEs) of Euler-Bernoulli beam theory. Since ω_Z, the Z modulation frequency of PFT mode is selected to be much less than ω, the microcantilever's fundamental frequency, ($\varpi = \omega/\omega_Z \gg 1$), the inertial and damping terms of the beam PDEs become negligible and the model can be approximated as follows:

$$k \times q(t) \approx F_{ts}(t), \tag{79}$$

where k is the static spring constant of the microcantilever and $q(t)$ is the generalized coordinate represents the tip deflection at time t. Eqn. (79) can be represented as an equivalent spring-mass

model shown in Figure 36-b. the transient phenomena such as microcantilever ringing during retraction cannot be captured using the steady-state solution.

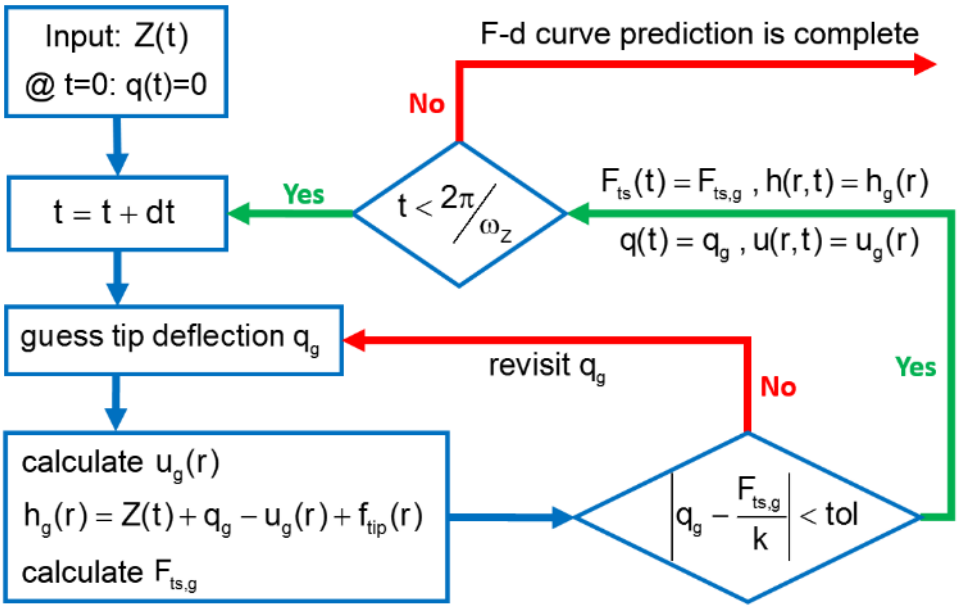

Figure 39. The algorithm proposed in this work for predicting the F-d curve in PFT AFM. the axisymmetric tip profile is defined by $f_{tip}(r)$.

We use EAM to calculate F_{ts} in Eqn. (79). The EAM model allows including different linear viscoelasticity models such as the ones with single relaxation time such as KV, Maxwell, standard linear solid (SLS), or power-law rheology (PLR) models or the ones with multiple relaxation times such as the generalized Maxwell model also known as Prony series. EAM is versatile in terms of including various tip-surface interaction forces such as electrostatic, capillary, or van der Waals forces. In this work, we model the surface viscoelasticity and tip-surface interaction by the SLS model and Lennard-Jones pressure (LJ) equations, respectively. The creep compliance function, $J(t)$, of an SLS viscoelasticity element is:

$$J(t) = \frac{1}{E_\infty} + \frac{E_\infty - E_0}{E_0 E_\infty} e^{-t/\tau} \qquad (80)$$

where, E_∞, E_0, and τ are long term modulus, short term modulus, and retardation (creep) time of the surface, respectively. LJ pressure equation predicts the interaction force per unit area between two parallel and infinite surfaces with distance h as follows:

$$p(h) = \frac{H}{6\pi h^3}\left(\frac{z_0^6}{h^6} - 1\right) \tag{81}$$

where z_0 and H are the intermolecular equilibrium distance and Hamaker constant of interacting surfaces, respectively.

In EAM, a set of n_b radial cosine terms as even biorthogonal functions are used to reconstruct the deformed surface profile, $u(r,t)$, at each time step:

$$u(r,t) = \sum_{i=0}^{n_b} a_i(t)\cos(i\pi\frac{r}{r_d}), \tag{82}$$

where r is the radial distance from the central symmetry axis (Figure 36a) and r_d indicates the computational domain beyond which the tip-sample interaction is considered negligible. The matrix representation of the numerical solution of the model's governing differential equations at each timestep can be demonstrated as the multiplication of inverse of a Jacobean matrix J and a vector b, defined as follows:

$$\dot{a}_i(t) = J_{ij}^{-1}\, b_j, \tag{83}$$

$$J_{ij} = \frac{1}{E_{0,s}}\int_0^{r_d} p'(h(s,t))\cos(i\pi\frac{s}{r_d})\, s\, \rho_j(s)\, ds - \delta_{ij}\times\zeta_j, \tag{84}$$

$$b_j = \frac{a_j(t)}{\tau}\zeta_j + \frac{1}{\tau E_{\infty,s}}\int_0^{r_d} p(h(s,t))\, s\, \rho_j(s)\, ds + \frac{\dot{d}(t)}{E_{0,s}}\int_0^{r_d} p'(h(s,t))\, s\, \rho_j(s)\, ds, \tag{85}$$

where, $h(r,t)$ is the tip-surface distance at radius r and time t (Figure 36a). $p'(h(r,t)) = dp(h(r,t))/d\,h(r,t)$, $\dot{d}(t) = dd(t)/d\,t$, δ_{ij} is the Kronecker delta, and $E_{0,s}$ / $E_{\infty,s}$ are reduced short/ long term modulus of the sample, defined as follows:

$$E_{0,s} = \frac{1-\nu^2}{E_0}, \qquad E_{\infty,s} = \frac{1-\nu^2}{E_\infty}, \tag{86}$$

where, ν is the Poisson's ratio of the surface. The time-independent variables $\rho_j(s)$ and ζ_j are defined as:

$$\rho_j(s) = \int_0^{r_d} \cos(j\pi \frac{s}{r_d})\, k(r,s)\, dr\,, \tag{87}$$

$$\zeta_j = \int_0^{r_d} \cos^2(j\pi \frac{s}{r_d})\, dr\,, \tag{88}$$

where the kernel term of the integral in Eqn. (87), $k(r,s)$, is expressed in terms of the complete elliptic integral of the first kind[81] of the surface, K, as follows:

$$k(r,s) = \begin{cases} \frac{4}{\pi r} K(s^2/r^2) & s < r \\ \frac{4}{\pi s} K(r^2/s^2) & s > r \end{cases}. \tag{89}$$

The EAM parameters and the employed computational methods and enhancements are further elaborated in chapter 4. The tip-surface interaction force, $F_{ts}(t)$, for each time-step is calculated by integrating the tip-surface interaction forces over the whole computational domain:

$$F_{ts}(t) = 2\pi \int_0^{r_d} p(h(r,t)\, r\, dr\,. \tag{90}$$

Then, we propose an algorithm (Figure 19) that predicts PFT force curves when a microcantilever with a prescribed sinusoidal Z motion interacts with a surface with known viscoelastic and adhesive properties. The algorithm has a loop in which the guessed tip deflection for each timestep, q_g, is corrected at each iteration until calculated $F_{ts}(t)$ using EAM becomes equal to $\approx k \times q_g$ as in Eqn. (79). Subsequently, all the predicted parameters including $u(r,t)$, $h(r,t)$, $q(t)$, and $F_{ts}(t)$ for that instance are recorded. This procedure continues for all timesteps of an oscillation cycle and then, the force curve prediction process is complete. The subscript "g" denotes a guessed value for a parameter.

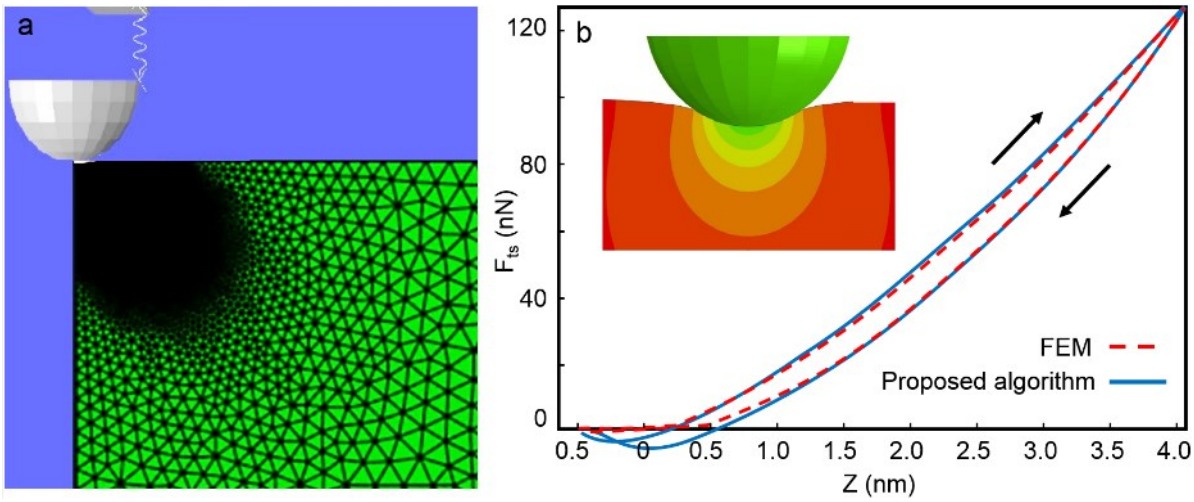

Figure 40. (a) Developed FE model includes a spherical rigid indenter which on one side interacts with a surface and from the other side is connected to an oscillating plate by a linear spring. This ensemble represents the sub-resonant excited cantilever in PFT AFM. (b) The agreement between the F-Z curves predicted by the proposed model and the FE model is presented in this graph. The surface adhesive forces are not included in the FE model. The inset shows the effective von Mises stress distribution during the interaction time.

5.3 Validation of the proposed algorithm

To ensure the validity of the proposed algorithm, we first compare its predictions with the ones by a developed finite element (FE) model with identical input parameters. In the developed axisymmetric FE model, a spring element with constant k connects a rigid spherical indenter to a moving base element (Figure 40a). We constrained the contact between the sample with a fixed bottom surface and the indenter to be frictionless. The results are tested to be grid-independent and a refined adaptive meshing around the indentation zone on the sample is implemented to assure obtaining reliable accuracy. FE simulations were conducted in Abaqus CAE (version 14, Simulia Corp., Providence, RI) environment. The comparison between the resultant F-Z curves for the same input parameters demonstrates excellent consistency (Figure 40b). The difference in the attractive part of the force curve is due to the neglect of surface long-range forces in the developed FE model. The surface properties used in these simulations are: $E_0 = 3.87$ GPa , $E_\infty = 1.94$ GPa , $\tau = 0.1$ s , $H = 1\times10^{-20}$ J , and $z_0 = 0.3$ nm . The base of a cantilever with a spherical tip with R=15 nm oscillates through a triangular waveform with 1 Hz frequency and 100 nm amplitude.

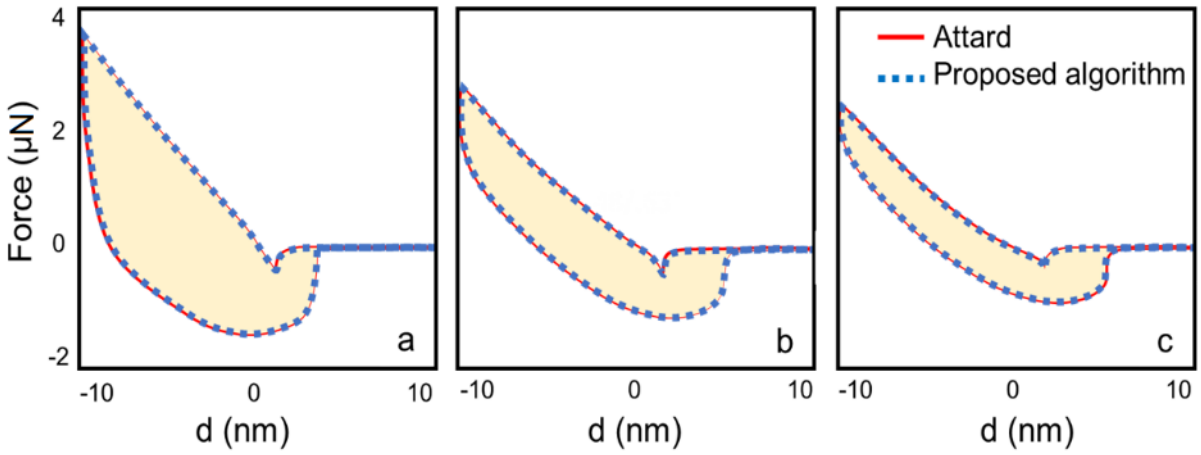

Figure 41. F-Z predictions by the proposed model and the ones provided in Attard's original Work for two different tip velocities. The identical employed surface properties in both models are: $E_0 = 10\,\text{GPa}$, $E_0 = 1\,\text{GPa}$, $\tau = 1\,\text{ms}$, $H = 1\times10^{-19}\,\text{J}$, and $z_0 = 0.5\,\text{nm}$. Tip radius is R = 10 μm. The velocities of Z triangular waveforms are different between graphs: (a) $\pm5\,\mu\text{m/s}$, (b) $\pm2\,\mu\text{m/s}$, (c) $\pm1\,\mu\text{m/s}$.

Next, we assess the agreement between the predictions of the proposed model and the ones presented in Attard's original work for prescribed triangular tip motions with three different velocities (Figure 41). Since the employed model by Attard does not include the cantilever mechanics, we select to use a very large value for the spring constant to minimize the tip deflection during the interaction cycle and facilitate comparison between results. The employed surface and cantilever properties are identical with the ones used in Attard's work and are listed in the caption of Figure 41.

5.4 Computational results

To further visualize the physics of PFT AFM on soft polymers, we employed the proposed algorithm to perform a single cycle PFT AFM simulation on an elastomer sample. The results are illustrated in Figure 42. The elastomer viscoelastic properties, which are represented by an SLS model, as well as the PFT operational parameters for this simulation are listed in column '*' of Table 11. The predicted $q(t)$ and $F_{ts}(t)$ are illustrated in Figure 42a and Figure 42b, respectively.

Table 11. Operational and material characterization used in simulations for visualizing the cantilever-sample interaction in PFT mode of operation and parametric study. The colored cells are the parameters whose effect on the predicted F-d curves are studied and the employed range for each is mentioned in the legends of each of the sub-figures in Figure 43 with the same label.

	*	a	b	c	d	e	f	g	h	i
R (nm)	30	30	30	30	30	30	30		30	30
k (N/m)	5	5	5	5	5	5		5	5	5
f (kHz)	2	2	2	2	2	2	2	2	2	
A_Z (nm)	100	100	100	100	100	100	100	100		100
E_0 (GPa)	1	1	1	1			1	1	1	1
E_∞ (GPa)	0.1	0.1	0.1		0.1		0.1	0.1	0.1	0.1
H (10^{-20} J)	8		8	8	8	8	8	8	8	8
z_0 (nm)	0.31	0.31		0.31	0.31	0.31	0.31	0.31	0.31	0.31

During the tip approach, the long-range attractive forces between the axisymmetric rigid tip and the surface cause the microcantilever to deform downward toward the surface. Simultaneously, on the sample side, as shown in $u(r=0,t)$ graph (shown as the dashed line in Figure 42a), the attractive forces cause the surface to gradually rise upward from its initial flat state. Eventually, when F_{ts} gradient exceeds the microcantilever stiffness, k, the tip of the deflected down microcantilever and the bulged surface meet each other above the undeformed surface level through a rapid non-equilibrium phenomenon so-called "snap-in" (also known as jump into contact). The snap-in instance of the cycle is labeled as I in Figure 42a and its associated surface deformation, $u(r,t)$, and the pressure distribution over the computational domain, $p(r,t)$, are shown in Figure 42c and Figure 42g, respectively. By further approaching, the total interaction force between the tip and the surface gradually switches to repulsive and the microcantilever deflects upward, accordingly.

When $F_{ts}(t)$ reaches the peak force setpoint, the cantilever begins to retract. Instances labeled as II and III in Figure 42a, with associated $u(r,t)$ shown in Figure 42d and Figure 42e, and $p(r,t)$ shown in Figure 42h and Figure 42i, respectively, are meant to represent this part of the cycle. As seen in Figure 42h and Figure 42i, while the total tip-surface interaction is repulsive, the predicted pressure distribution over the contact region by the algorithm includes a central repulsive part surrounded by regions with distributed attractive pressures. During retraction, the central repulsive region progressively shrinks and the tip-surface interaction regime on those areas

convert to attractive. As shown in Figure 42a, when $F_{ts}(t) = 0$ during retraction the surface is still below the undeformed level ($u(r = 0, t) < 0$) and the material needs more time to complete the return process. If there are no attractive forces between tip and sample, the tip detaches the yet indented surface when $F_{ts}(t) = 0$. However, in the simulated example, the long-range attractive forces prevent this. The attractive forces cause the surface to form a meniscus around the retracting tip profile and detachment occurs through a gradual "peeling off" process. In this process, the outermost areas of the contact region on the surface gradually detach the tip until it fully separates through another non-equilibrium phenomenon so-called "snap-off" (labeled as IV in Figure 42a). The associated $u(r, t)$ and $p(r, t)$ for this instance are shown in Figure 42f and Figure 42j, respectively. When the final detachment happens, the surface begins to relax to its original state by its timescale. The situation of the surface when snap-off occurs depends on the material viscoelastic properties and the operational parameters. In this work, we assume the surface will be provided enough chance to return to its original state before being hit by the subsequent tap. The obtained insightful predictions about the cantilever-sample interaction in PFT AFM using the proposed algorithm cannot be fully achieved using any of the classical models such as Hertz, JKR (Johnson, Kendall, and Roberts), DMT, or Ting's model.

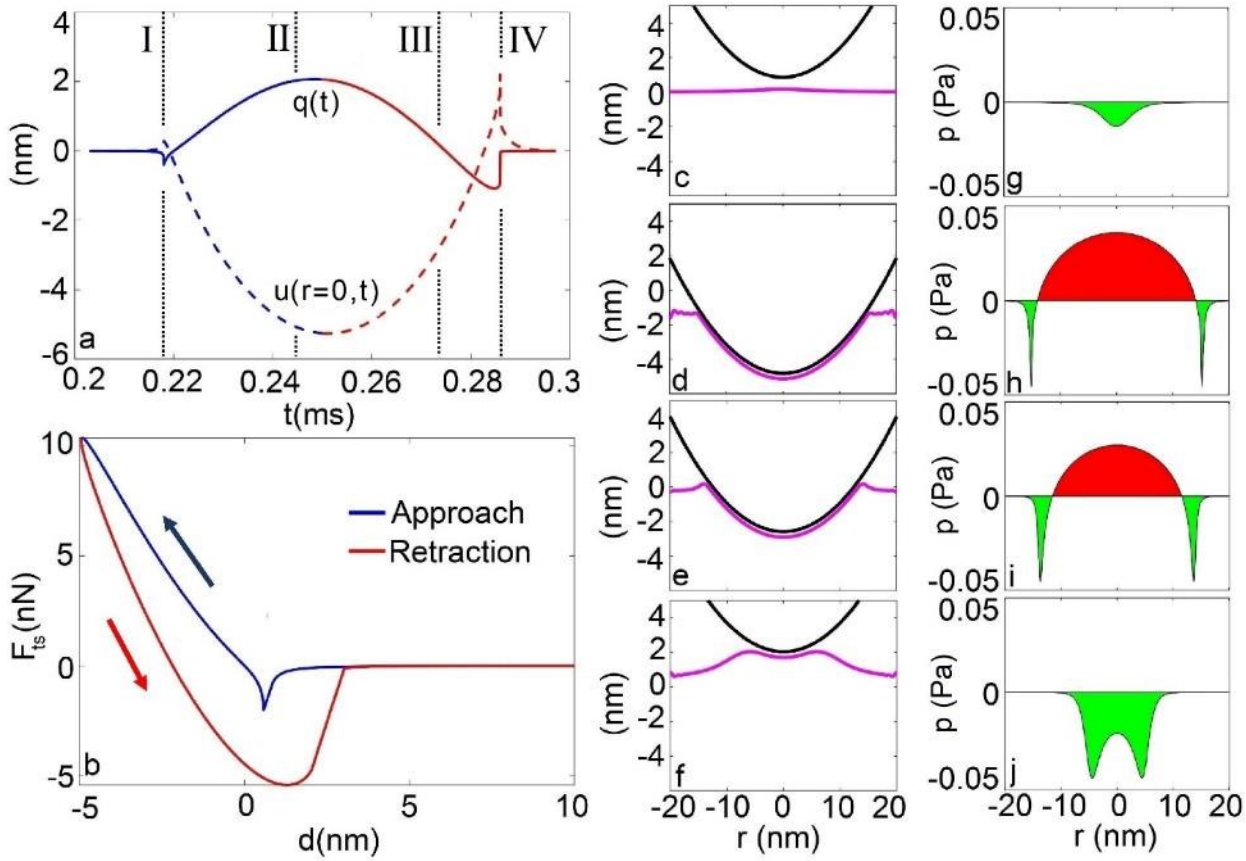

Figure 42. Simulation results for a single cycle of PFT AFM on an elastomer sample. The labels for each sub-figure are specified at its bottom left. The operational parameters and cantilever and surface properties are listed in Table 11 under column "*". Graph (a) illustrates the tip deflection and surface deformation at r=0 (dashed line) during interaction time and graph (b) depicts the predicted F-d curve. The red and blue segments of these graphs represent the approach and retraction phases of the cycle. 4 instances during the interaction time including snap-in and snap-off phenomena are marked with vertical dotted lines and labeled as I, II, III, and IV in the graph (a). The predicted surface deformation as well as the tip position at these instances are shown in (c), (d), (e), and (f) graphs, respectively. The associated pressure distribution over the contact region at these instances are also shown in (g), (h), (i), and (j) graphs, respectively. The green and red areas in (g), (h), (i), and (j) graphs represent attractive and repulsive interaction pressures, respectively.

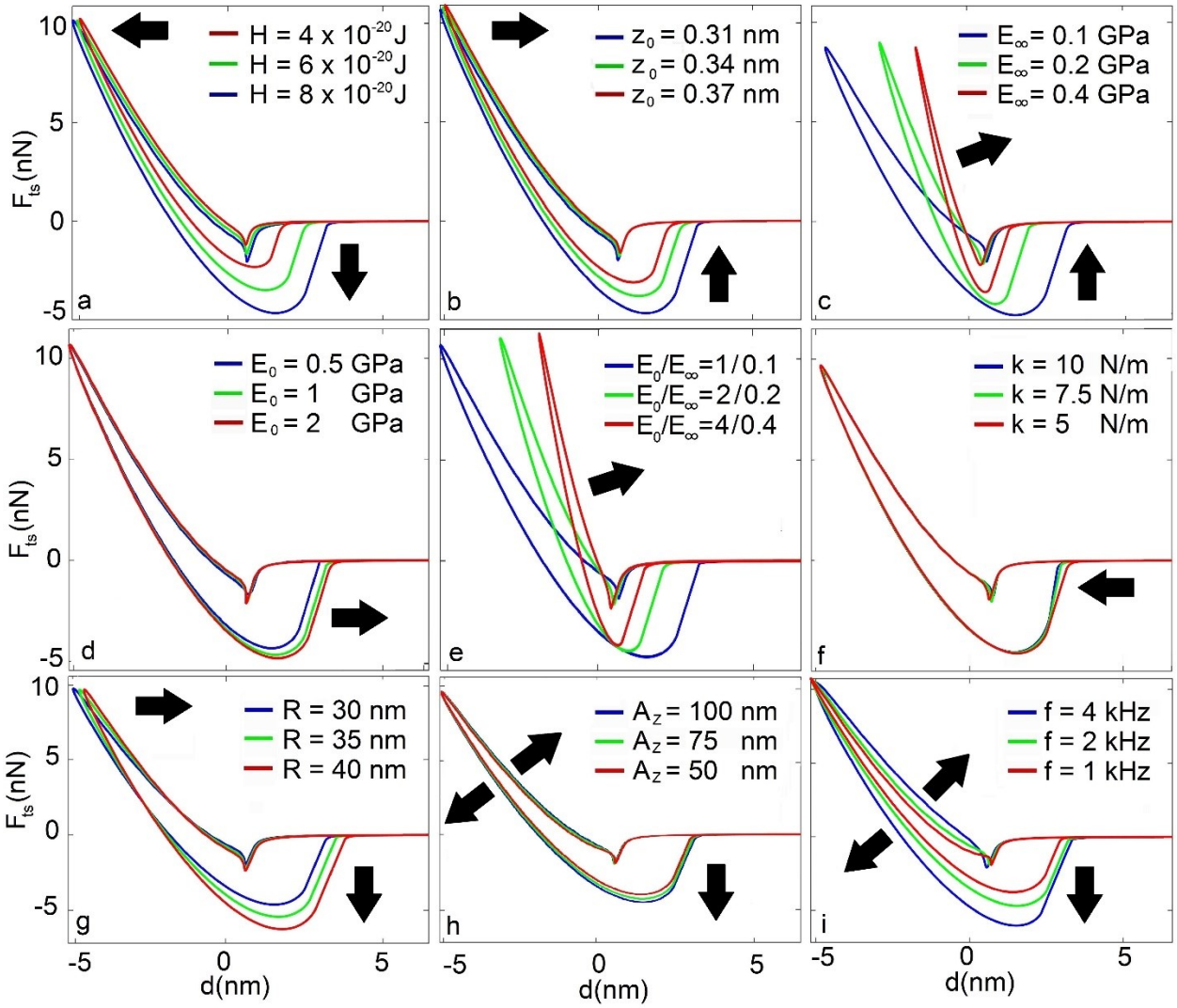

Figure 43. Predicted F-d curves variation when the operational parameters and surface viscoelastic/adhesive properties are systematically changed. The labels for each sub-figure are specified at its bottom left. At each of the graphs except (c), only one of the parameters which are specified in the legend is changed and other surface properties or operational parameters are identical. At (c), both E_0 and E_∞ are changed while the E_∞/E_0 ratio remains constant. Full input parameters used for each set of simulations are listed in Table 11 with the same label specified at each graph. For all these simulations $\tau = 1\,\mu s$. Arrows are intended to visually help to distinguish the predicted changes on the F-d curves by increasing the parameter of interest at each sub-figure.

We conducted a series of parametric studies at which the effect of variation of microcantilever/ surface properties or operational parameters on the predicted PFT force curves are systematically evaluated (Figure 43). The input parameters employed for each of these sets of simulations are listed in Table 11 with the same labeling word as shown in Figure 43 graphs. The

predictions show that the adhesion force variation through H and z_0 has a stronger effect on the retraction segment of the F-d curve and the approach segment and its slope remains almost unchanged (Figure 43a and Figure 43b, respectively). The higher tip-surface adhesion leads to a longer "peeling off" process, i.e., outermost regions of the contact zone become more resistant to detach the tip profile. For soft polymers, the surface follows the tip to a height above its undeformed state, and simultaneously the cantilever deflects further downward before detachment. Changing surface adhesion does not lead to a considerable change in the indentation depth.

Figure 43c, Figure 43d, and Figure 43e depict the F-d curve variation due to change of SLS parameters (Eqn. (80)) with a constant $\tau = 1\,\mu s$ which is much smaller than the interaction time. Either increasing E_0 when E_∞ is constant or decreasing E_∞ when E_0 is constant leads to force loops with greater hysteresis. When $\tau \ll$ the interaction time, the majority of the surface on the contact zone have enough chance to transit its stiffness from E_0 to E_∞ and the increased dissipation due to E_∞ reduction cause the whole force curve reshapes (Figure 43c). However, boosted dissipation due to E_0 increase manifests itself mainly in the attractive part of the retraction segment of the force curve (Figure 43d). Therefore, when $\tau \ll$ the interaction time, E_∞ change will more significantly affect the resultant F-d curve. In Figure 43e, we change both E_0 and E_∞ while their ratio E_∞ / E_0 (Deborah's number) remains constant. The resultant F-d curve variation is a mixture of both effects seen when either E_0 or E_∞ changes.

Then we examine the predicted F-d curve variation due to change of microcantilever properties including microcantilever stiffness, k (Figure 43f) and Tip radius, R (Figure 43g). The microcantilever deflection, q, proportionally changes with its k value variation, but the indentation depth, tip trajectory, and sample deformation during the interaction time do not noticeably change. When all the parameters are identical except microcantilever stiffness, a softer microcantilever spends more time interacting with the surface than a stiffer microcantilever. That is since the snap-in/off with the surface for the softer microcantilever occurs earlier/later than a stiffer one. As described earlier, the snap-in/off phenomenon are results of the mutual contribution of the surface and the microcantilever to minimize the interaction energy between the approaching/retracting tip and the surface. The amount of contribution of the surface or the microcantilever in these processes depend on the surface/microcantilever properties and adhesion force between them. When we

employ a softer microcantilever, its more flexibility leads to its more contribution during the snap-in/off instances. Variation of the microcantilever's tip radius, R, does not noticeably influence the length of the interaction time and its effect on the predicted F-d curves is mainly due to an increase of the contact radius (Figure 43g). This leads to a decrease in indentation depth and an increase in pull-off force as tip radius increases. When τ to interaction time ratio is smaller than 1, A_Z (Figure 43h) and f (Figure 43i) reduction leads to less dissipative F-d loops. This trend is inverse when τ to interaction time ratio is greater than 1.

5.5 Regression-based machine-learned predictive models

Using data analytics strategies in material science to predict the material's characteristics, response, or behavior emerges as an efficient and accurate alternative for computationally solving the fundamental governing equations or conducting a comprehensive set of experiments [147]. The resultant surrogate machine learning models provide predictive capabilities based on recognizing the underlying patterns in the past data. When there is not an established theoretical model to connect the observables to the material characteristics or it is hard to perform measurements or computations using traditional techniques, data-centric informatics methods are favorable. These methods typically involve a "descriptor" selection phase in which the proper number of observables as input parameters of the model are carefully chosen. The descriptors may have different units and scales and therefore, implementing a scaling process to assimilate their scales is recommended. Then, a learning algorithm maps between the descriptors and the material properties of interest using a linear [148] or nonlinear regression-based technique such as support vector regression (SVR)[149], random forest regression (RFR)[150], or multilayer neural networks (MLP)[151]. We need to have an inclusive set of material characteristics with known associated descriptors to train the learning predictive algorithm. Usually, different combinations of selected descriptors and various learning algorithms are examined to determine the configuration that delivers the optimized predictive performance.

As illustrated earlier, the forward EAM-based algorithm predicts PFT force curves based on known material/cantilever properties and PFT operational parameters. However, there is not a straightforward way to tackle the inverse problem i.e., estimating the material properties according to a given force curve and its associated cantilever properties and PFT operational parameters. The complexity of the inverse problem of the proposed algorithm is partly due to the way the tip-

surface interaction force is calculated by EAM. As shown earlier, for each instance during the interaction cycle with known tip position/velocity with respect to the undeformed surface, EAM first predicts the deformed surface velocity/position profile and then, calculates F_{ts} by integrating over all interacting tip-surface radial elements. This indirect established link between tip position/velocity and the associated F_{ts} complicates the pathway for the inverse solution of the problem. Therefore, we utilize the predictions of the proposed forward algorithm as the training data for a data analytics-based inverse solution. This model is expected to map the problem descriptors which are the given F-t curve, the utilized microcantilever properties, and PFT operational parameters to the material viscoelastic and adhesive properties. The training dataset with known descriptors and associated material properties are split into two portions: a training set and a test set. We use these sets to train and evaluate the performance of the ML algorithm, respectively.

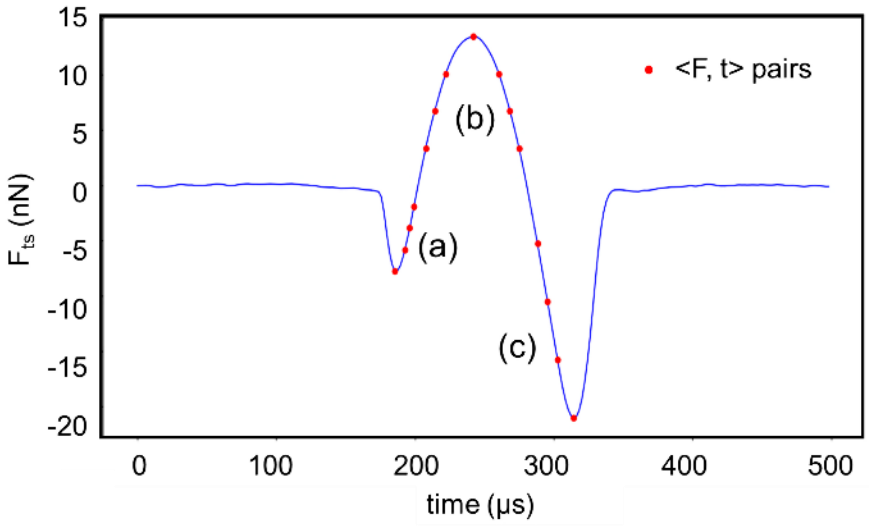

Figure 44. The used F-t curve parametrization method. The red dots shown on the curve are the 15 representative <F, t> pairs for the stable regions of an F-t curve acquired on a polyolefin-based elastomer (Engage 8003, The Dow Chemical Company).

Simulated F-t curves need to be parametrized to a set of representative values acting as ML model descriptors. To do so, we split the F-t curve into three segments as illustrated in Figure 44 on an F-t curve acquired on a polyolefin-based elastomer (Engage 8003, The Dow Chemical Company): (a): Approach/ attractive, (b): repulsive, and (c): retraction/ attractive. To parametrize the F-t curve, we first determine and record the maximum retraction or attractive tip-surface

interaction force for each of these segments as well as their associated nondimensionalized time instance (3 points): $\left\langle \left|F\right|_{max,\gamma}, t_{max,\gamma} \times f \right\rangle$ where γ: a, b, and c. Then, the following 12 <F, t> pairs on the stable parts of the given F-t curve, as marked in Figure 44, are recorded: $\left\langle \theta_i \times \left|F\right|_{max,\gamma}, t_i \times f \right\rangle$ where: $i = 1, 2, 3$ and $\theta_i = 0.75, 0.5, \text{and } 0.25$. Each θ_i when $\gamma = b$ has two associated nondimensionalized time instances. Using this method, the stable parts of a given F-t curve can be represented by total of (12+3=15) <F, t> pairs with 18 independent values. These values along with the tip radius, R, and cantilever stiffness, k, constitute the problem descriptors (total 20 values).

The forward solution algorithm generates a set of predicted F-t curves for an associated known operational and microcantilever parameters and sample viscoelastic properties. For these set of simulations, we assume $A_Z = 50 \text{ nm}$, $f_Z = 2 \text{ kHz}$, $z_0 = 0.3 \text{ nm}$, $\nu = 0.5$, and $\tau = 5 \mu\text{s}$. The defined ranges for Z and other material/ microcantilever parameters for the training set simulations are shown in Table 12. These ranges are defined based on the expected properties for elastomer samples and Bruker RTESPA-150-30 probes. The input parameters for the training set simulation are randomly selected over these defined ranges using the Latin hypercube sampling (LHS) method [120]. We use two different predictive regression algorithms, support vector regression (SVR) [149] and multi-layer neural network (MLP) [151], to connect the model descriptors to the output parameters: E_∞, E_0, H, and Z. For each of these algorithms, we use a grid-based search to optimize the regression parameters such as kernel type for SVR or size of the hidden layers for MLP. We use a k-fold cross-validation technique to avoid overfitting the employed regression algorithms to the training data [152]. In the k-fold cross-validation technique, first, the training dataset is divided into k portions with an almost identical number of samples and then, the predictive performance of the algorithm is k times evaluated (we use k=5 for this work). At each of these k times, one of the k portions of the dataset is considered as the test set and the remaining k-1 portions are used to train the algorithm. The optimal parameters for the algorithms are the ones that deliver the minimum cross-validation error comparing with others. Since the descriptors and output parameters are in various scales/ units and also to reduce the impact of outliers, we independently scaled each of these training data parameters using a robust non-linear preprocessing technique so that each follows a normal distribution. Due to various scale of the

output material properties, we calculate the error of the model predictions based on the "mean absolute percentage error" (MAPE) which is defined as:

$$\mathrm{MAPE} = \frac{100\%}{n}\sum_{t=1}^{n}\left|\frac{A_t - P_t}{A_t}\right|, \tag{91}$$

where, n is the number of the predictions and A_t and P_t are the actual and the ML prediction values, respectively.

Table 12. The ranges for Z and other material/ microcantilever parameters for the training set simulations. These ranges are defined based on the expected properties for elastomer samples and Bruker RTESPA-150-30 probes. The input parameters for the training set simulation are randomly selected over these defined ranges using the Latin hypercube sampling (LHS) method [120].

R (nm)	k (N / m)	Z (nm)	E_0(GPa)	E_∞(GPa)	H ($\times 10^{-20}$ J)
30 ± 10	5 ± 2	42 ± 4	4.5 ± 4	0.11 ± 0.09	20 ± 15

A typical set of predictive accuracy evaluation charts for SVR and MLP models is illustrated in Figure 45. In each of these charts, the actual and predicted values, which are ideally supposed to be equal (represented by the dashed red lines), for one output parameter are compared for the employed ML models. The calculated MAPE for each of the output parameters are listed in Table 13, based on 10 times using the predictive models on the training data. For each of these times, 20% of the training dataset is randomly selected as the test set and the model is trained with the rest of the data.

Table 13. the evaluation results for the ML models' predictive accuracy. The employed test percentage used in these evaluations is 20%.

model	E_∞	E_0	H	Z
MLP	$4.3 \pm 0.4\%$	$28.4 \pm 6.5\%$	$5.2 \pm 0.6\%$	$0.3 \pm 0.1\%$
SVR	$3.8 \pm 0.8\%$	$26.9 \pm 9.5\%$	$5.0 \pm 1.1\%$	$0.3 \pm 0.1\%$

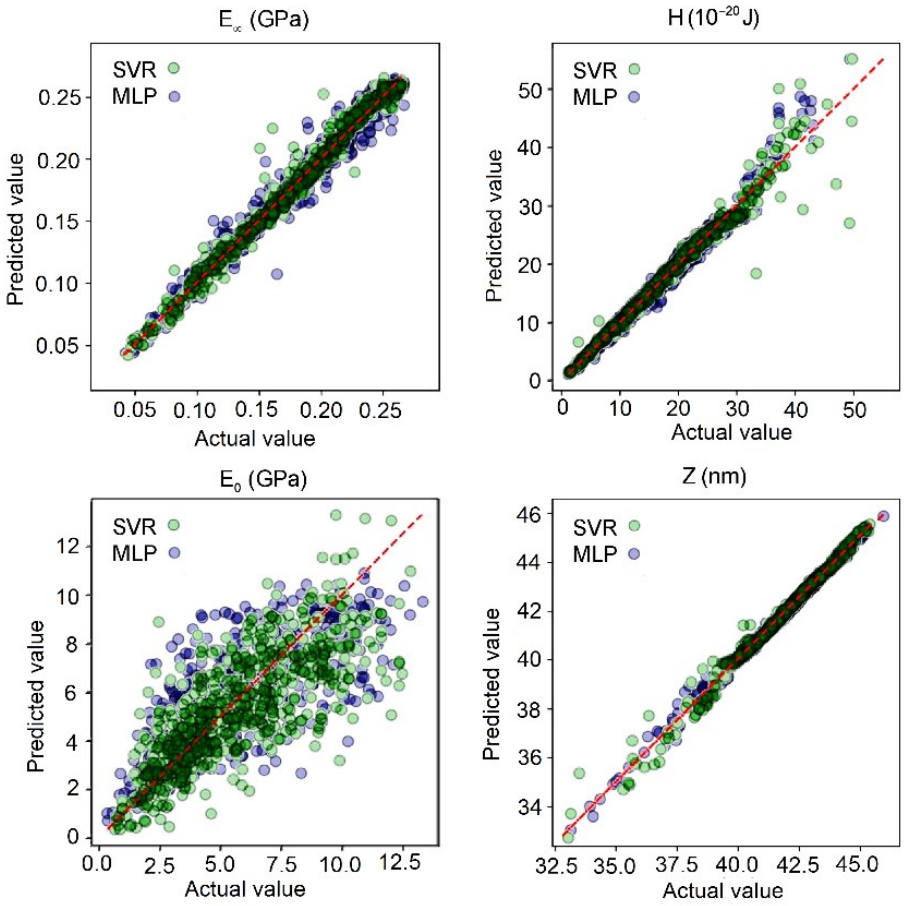

Figure 45. A typical set of the models' predictive accuracy evaluation charts when 20% of the training data is considered as test data. In these charts, the actual and predicted values, which ideally supposed to be equal (represented as dashed red lines), for E_∞, E_0, H, and Z using each of the employed ML models are illustrated and compared.

Except for E_0, both SVR and MLP models provide almost equally acceptable predictive accuracy. MLP predictions undergo less accuracy variation comparing with SVR and lead to a smaller number of outliers. We hypothesize that the weaker predictive performance for E_0 by both regression models is due to the reduced sensitivity of the simulation F-t curves to their associated E_0 values in the training dataset. The low E_0 sensitivity is a consequence of the selected τ for the material which is $\ll$ the interaction time. This causes the creep compliance function of the material, Eqn. (80), converges to its associated E_∞ at early stages of the interaction and in the following instances $J(t) \approx 1/E_\infty$. This limits the effect of E_0 on the resultant F-t curve and consequently, a range of E_0 values may lead to almost the same simulated F-t curves. This causes

the pattern recognition process by the ML model to become challenging. Furthermore, it shows that when using the SLS viscoelasticity element to represent the viscoelasticity behavior of the sample, the selection for τ to interaction time ratio regulates the influence level of E_0 and E_∞ values on the resultant F-t curves. With the analogous reasoning, a similar issue with E_∞ when $\tau \gg$ the interaction time is expected. Nonetheless, the acceptable accuracy of the models' predictions for Z, E_∞, and H shows the regression-based models' ability to tackle the inverse problem.

5.6 Conclusions

We demonstrate the utilization of EAM as an advanced 3-dimensional viscoelastic model in the context of PFT. Analysis of the results enables a better understanding of the mutual interaction between the microcantilever and the sample during a PFT cycle. The results highlight the effects of viscoelasticity and long-range surface forces and can accurately capture complex dynamics such as sample necking and energy loss due to peeling away of the surface from the retracting tip. The computational parametric study depicts the role of sample properties, microcantilever properties, and PFT operational parameters on the predicted force curves. Finally, we presented a data-analytics approach to estimate the material viscoelastic and adhesive properties based on an observed force curve. We compared using two regressive based algorithms to tackle the inverse problem and concluded the multilayer neural network model leads to fewer outliers on the test data. The demonstrated algorithm enables rigorous, first principles viscoelastic contact mechanics models to be applied to PFT AFM simulations and experiments.

6. CONCLUSIONS AND FUTURE WORK

6.1 Contributions of This Thesis

The research works reported in this thesis contribute to the active scientific efforts toward characterizing the soft viscoelastic materials, such as polymers and biological samples at the nanoscale. The proposed methodologies/ algorithms and obtained results in this thesis provide considerable advancement and insight to better understanding the complexities associated with using AFM to characterize soft-viscoelastic-adhesive samples. Specifically, the main contributions of this thesis are a) to present a fast, rigorous, and 3-dimensional viscoelastic model (EAM), b) to embed this model into selected AFM modalities' framework through proposing algorithms, and c) to employ the proposed algorithms to predict/ interpret AFM modes observables/ acquired images. These contributions are briefly reviewed in the next paragraphs.

In this thesis, we introduce EAM which is a computationally enhanced continuum mechanics viscoelasticity contact model based on the model proposed by Attard et al. [2]. The achieved excellent accuracy and quick computations by EAM addresses an important gap in using the existing AFM-based nanoscale viscoelastic/adhesive properties measurement techniques for the soft-adhesive-viscoelastic surfaces. To understand the tip-surface interaction on such samples, we need a physical model that accurately and comprehensively accounts for the effects of the surface viscoelasticity/ dynamics as well as the long-range surface forces. The existing AFM-based nanoscale mechanical properties measurement techniques often use simplistic *ad hoc* contact models that do not rigorously account for these effective tip-surface interaction parameters. The shortcomings of *ad hoc* viscoelasticity contact models can result in inaccurate predictions for the material properties, especially when used on soft-adhesive-viscoelastic samples. They also may lead to artifacts in the predictions such as the ones elaborated in this thesis.

Despite the advantages of EAM in comparison with common *ad hoc* viscoelasticity models, its implementation to model AFM modes is challenging. Like other continuum mechanics-based viscoelasticity contact models, EAM does not lead to a closed-form solution connecting the indentation depth to the tip-surface interaction force and its understanding/ implementation is complex. Furthermore, its complexity leads to more time-consuming and expensive computational needs. In this thesis, we propose algorithms to tackle the forward problem in which the tip-surface

interaction is predicted by EAM for selected AFM modes: AM-AFM, bimodal AFM, and PFT AFM. These algorithms enable making reliable predictions for the tip-surface interaction phenomena on such samples when the effective parameters are rigorously and comprehensively accounted for. They establish a link between the material/ microcantilever/ operational parameters to the associated AFM mode observables. Furthermore, they enable visualizing the various phenomena that occur during an interaction cycle either on the sample or microcantilever side.

The inverse problem i.e., linking the AFM modes observables and the material viscoelastic and adhesive properties using EAM is not straightforward. The lack of having a closed-form solution connecting the relative position of tip-surface to the interaction force necessitates using data-analytics-based approaches to tackle the inverse problem. In this thesis, we examine and present using linear regression and machine learning algorithms to connect bimodal AFM and PFT AFM observables to the material viscoelastic and adhesive properties. These multivariate data-analytics approaches are first trained on a set of data generated using the forward solution simulations. These simulations are performed based on randomly but systematically selected input parameters on an appropriate range for sample properties and microcantilever/ operational parameters.

6.2 Future Research Directions

1- Despite the improvements offered by introducing EAM (chapter 4), the complexity of the continuum mechanics-based viscoelasticity contact models, both from understanding and implementation perspectives, limits their common utilization. So, simplifying these models, either for predicting AFM observables or interpreting AFM images to estimate the samples' mechanical properties, is highly encouraging. The data-centric Physics-informed learning algorithms assist in the identification of closed-form governing equations that can characterize the physical behavior of a system [153]. The learned correlations through these algorithms can be considered as a surrogate model that relies on the recognized underlying dynamics of the system instead of a large number of fitting parameters. These types of models enjoy an enhanced extrapolation and generalization capability which is not usually possible for common machine learning algorithms. These types of models can specifically of interest to the complex dynamic phenomena for which acquiring a direct solution is not achievable. The size of the required training data depends on the system's complexity and stochasticity. The training dataset can be either from the experimentally

measured or simulation results. As an example of such models, the "symbolic regression" algorithm leads to an explicit solution form of $f(y,\theta)$ for the system in which θ are coefficients of a selected complete set of basis functions, $\Gamma(y)$, such as polynomials: $f(y,\theta)=\theta\times\Gamma(y)$. The θ coefficients are determined through training the algorithm with a proper set of experimental or simulation data [154]. The "sparse identification of nonlinear dynamics (SINDY)", another example of such algorithms, uses an extra term in the loss (error) function to minimize the number of terms in $\Gamma(y)$ to accurately characterize the behavior of the system [155]. These type of techniques which has immense potential for application across various fields may assist in discovering an accurate governing equation that solves the forward problem and paves the path for a more straightforward EAM-based inverse solution. Furthermore, using these data-fueled techniques helps the computational robustness of EAM.

2- Acquiring PFT AFM experimental data on a set of soft-viscoelastic-adhesive polymeric samples and apply the proposed ML regressive model to experimental F-t curves, complements the work done in chapter 5. It is specifically of interest due to the vast utilization of PFT AFM to characterize polymeric samples which are mainly accomplished by using *ad hoc* viscoelasticity contact models. As described in the thesis, since the common *ad hoc* viscoelastic models do not comprehensively account for the physical phenomena that occur during tip-surface interaction on soft-viscoelastic-adhesive samples, their utilization may lead to non-reliable predictions. Therefore, illustrating the proposed regressive-based ML model's ability to tackle the inverse problem of a rigorous viscoelastic model that can be used on acquired experimental F-t data is highly favorable. furthermore, the proposed model enables characterizing the surface both in terms of the viscoelastic properties and surface adhesions, rather than the limitations of the common models to characterizing the surface adhesion.

3- Deployment of the proposed algorithms in this thesis on VEDA, the online AFM simulation platform of the group which is freely available to researchers/ industries. The provided accessibility through implementing these algorithms as a new set of tools on VEDA will assisting obtaining reliable predictions based on a rigorous viscoelastic contact model without dealing with its inherent complexities.

REFERENCES

1. Rajabifar, B., et al., *Dynamic AFM on Viscoelastic Polymer Samples with Surface Forces.* Macromolecules, 2018. **51**(23): p. 9649-9661.
2. Attard, P., *Interaction and deformation of viscoelastic particles. 2. Adhesive particles.* Langmuir, 2001. **17**(14): p. 4322-4328.
3. Binnig, G., et al., *Tunneling through a controllable vacuum gap.* Applied Physics Letters, 1982. **40**(2): p. 178-180.
4. Celotta, R.J., et al., *Invited Article: Autonomous assembly of atomically perfect nanostructures using a scanning tunneling microscope.* Review of Scientific Instruments, 2014. **85**(12): p. 121301.
5. Chiang, S., *Imaging atoms and molecules on surfaces by scanning tunnelling microscopy.* Journal of Physics D: Applied Physics, 2011. **44**(46): p. 464001.
6. Binnig, G., C.F. Quate, and C. Gerber, *Atomic Force Microscope.* Physical Review Letters, 1986. **56**(9): p. 930-933.
7. Müller, D.J. and Y.F. Dufrene, *Atomic force microscopy as a multifunctional molecular toolbox in nanobiotechnology*, in *Nanoscience And Technology: A Collection of Reviews from Nature Journals*. 2010, World Scientific. p. 269-277.
8. Majumdar, A., J. Carrejo, and J. Lai, *Thermal imaging using the atomic force microscope.* Applied Physics Letters, 1993. **62**(20): p. 2501-2503.
9. Garcıa, R. and R. Perez, *Dynamic atomic force microscopy methods.* Surface science reports, 2002. **47**(6): p. 197-301.
10. Sahin, O., et al., *An atomic force microscope tip designed to measure time-varying nanomechanical forces.* Nature Nanotechnology, 2007. **2**: p. 507.
11. Butt, H.-J., B. Cappella, and M. Kappl, *Force measurements with the atomic force microscope: Technique, interpretation and applications.* Surface science reports, 2005. **59**(1-6): p. 1-152.
12. Giessibl, F.J., *AFM's path to atomic resolution.* Materials Today, 2005. **8**(5): p. 32-41.
13. Steiner, P., et al., *Atomic-scale friction on stepped surfaces of ionic crystals.* Physical review letters, 2011. **106**(18): p. 186104.
14. Moy, V.T., E.-L. Florin, and H.E. Gaub, *Intermolecular forces and energies between ligands and receptors.* Science, 1994. **266**(5183): p. 257-259.
15. Mate, C.M., et al., *Atomic-scale friction of a tungsten tip on a graphite surface*, in *Scanning Tunneling Microscopy*. 1987, Springer. p. 226-229.
16. Shao, Z., et al., *Biological atomic force microscopy: what is achieved and what is needed.* Advances in Physics, 1996. **45**(1): p. 1-86.
17. Bustamante, C. and D. Keller, *Scanning force microscopy in biology.* Physics today, 1995. **48**(12).
18. Kienberger, F., et al., *Visualization of single receptor molecules bound to human rhinovirus under physiological conditions.* Structure, 2005. **13**(9): p. 1247-1253.
19. Moreno-Herrero, F., et al., *Atomic force microscopy contact, tapping, and jumping modes for imaging biological samples in liquids.* Physical Review E, 2004. **69**(3): p. 031915.
20. García, R. and R. Pérez, *Dynamic atomic force microscopy methods.* Surface Science Reports, 2002. **47**(6): p. 197-301.

21. Hansma, H.G., *Atomic force microscopy of biomolecules.* Journal of Vacuum Science & Technology B: Microelectronics and Nanometer Structures Processing, Measurement, and Phenomena, 1996. **14**(2): p. 1390-1394.
22. Schitter, G. and M.J. Rost, *Scanning probe microscopy at video-rate.* Materials Today, 2008. **11**: p. 40-48.
23. García, R., *Amplitude modulation atomic force microscopy*. 2011: John Wiley & Sons.
24. Albrecht, T., et al., *Frequency modulation detection using high-Q cantilevers for enhanced force microscope sensitivity.* Journal of Applied Physics, 1991. **69**(2): p. 668-673.
25. Sader, J.E., et al., *Quantitative force measurements using frequency modulation atomic force microscopy?theoretical foundations.* Nanotechnology, 2005. **16**(3): p. S94-S101.
26. Hölscher, H., et al., *Measurement of conservative and dissipative tip-sample interaction forces with a dynamic force microscope using the frequency modulation technique.* Physical Review B, 2001. **64**(7): p. 075402.
27. Gotsmann, B., et al., *Conservative and dissipative tip-sample interaction forces probed with dynamic AFM.* Physical Review B, 1999. **60**(15): p. 11051-11061.
28. Giessibl, F.J., *Atomic resolution of the silicon (111)-(7x7) surface by atomic force microscopy.* Science, 1995. **267**(5194): p. 68-71.
29. Raman, A., J. Melcher, and R. Tung, *Cantilever dynamics in atomic force microscopy.* Nano Today, 2008. **3**(1): p. 20-27.
30. Rodrıguez, T.R. and R. García, *Compositional mapping of surfaces in atomic force microscopy by excitation of the second normal mode of the microcantilever.* Applied Physics Letters, 2004. **84**(3): p. 449-451.
31. Garcia, R. and E.T. Herruzo, *The emergence of multifrequency force microscopy.* Nature nanotechnology, 2012. **7**(4): p. 217.
32. Legleiter, J., et al., *Scanning probe acceleration microscopy (SPAM) in fluids: mapping mechanical properties of surfaces at the nanoscale.* Proceedings of the National Academy of Sciences, 2006. **103**(13): p. 4813-4818.
33. Stark, R.W. and W.M. Heckl, *Higher harmonics imaging in tapping-mode atomic-force microscopy.* Review of Scientific Instruments, 2003. **74**(12): p. 5111-5114.
34. Schiener, J., et al., *Stabilized atomic force microscopy imaging in liquids using second harmonic of cantilever motion for setpoint control.* Review of scientific instruments, 2004. **75**(8): p. 2564-2568.
35. Martinez, N., et al., *Bimodal atomic force microscopy imaging of isolated antibodies in air and liquids.* Nanotechnology, 2008. **19**(38): p. 384011.
36. Dietz, C., et al., *Nanotomography with enhanced resolution using bimodal atomic force microscopy.* Applied Physics Letters, 2008. **92**(14): p. 143107.
37. Li, J.W., J.P. Cleveland, and R. Proksch, *Bimodal magnetic force microscopy: Separation of short and long range forces.* Applied Physics Letters, 2009. **94**(16): p. 163118.
38. Labuda, A., et al., *Generalized Hertz model for bimodal nanomechanical mapping.* Beilstein journal of nanotechnology, 2016. **7**: p. 970.
39. Herruzo, E.T., A.P. Perrino, and R. Garcia, *Fast nanomechanical spectroscopy of soft matter.* Nature communications, 2014. **5**: p. 3126.
40. Xu, X., et al., *Compositional contrast of biological materials in liquids using the momentary excitation of higher eigenmodes in dynamic atomic force microscopy.* Physical review letters, 2009. **102**(6): p. 060801.

41. Proksch, R., *Multifrequency, repulsive-mode amplitude-modulated atomic force microscopy.* Applied Physics Letters, 2006. **89**(11): p. 113121.
42. Lozano, J.R. and R. Garcia, *Theory of Multifrequency Atomic Force Microscopy.* Physical Review Letters, 2008. **100**(7): p. 076102.
43. Garcia, R. and R. Proksch, *Nanomechanical mapping of soft matter by bimodal force microscopy.* European Polymer Journal, 2013. **49**(8): p. 1897-1906.
44. Kocun, M., et al., *Fast, High Resolution, and Wide Modulus Range Nanomechanical Mapping with Bimodal Tapping Mode.* ACS Nano, 2017. **11**(10): p. 10097-10105.
45. Rajabifar, B., Bajaj, A., Reifenberger, R., Proksch, R., Raman, A, *Discrimination of Adhesion and Viscoelasticity from Nanoscale Maps of Polymer Surfaces using Bimodal Atomic Force Microscopy.* Under review, 2020.
46. Herruzo, E.T., et al., *Three-dimensional quantitative force maps in liquid with 10 piconewton, angstrom and sub-minute resolutions.* Nanoscale, 2013. **5**(7): p. 2678-2685.
47. Martinez, N., et al., *Enhanced compositional sensitivity in atomic force microscopy by the excitation of the first two flexural modes.* Applied Physics Letters, 2006. **89**(15): p. 153115.
48. Gigler, A.M., et al., *Repulsive bimodal atomic force microscopy on polymers.* Beilstein journal of nanotechnology, 2012. **3**: p. 456.
49. Stark, R.W., *Dynamics of repulsive dual-frequency atomic force microscopy.* Applied Physics Letters, 2009. **94**(6): p. 063109.
50. Kiracofe, D., A. Raman, and D. Yablon, *Multiple regimes of operation in bimodal AFM: understanding the energy of cantilever eigenmodes.* Beilstein journal of nanotechnology, 2013. **4**: p. 385.
51. Meyer, E., et al., *Comparative study of lithium fluoride and graphite by atomic force microscopy (AFM).* Journal of Microscopy, 1988. **152**(1): p. 269-280.
52. Hertz, H., *Über die Berührung fester elastischer Körper.* Journal für die reine und angewandte Mathematik, 1882. **92**: p. 156-171.
53. Derjaguin, B.V., V.M. Muller, and Y.P. Toporov, *Effect of contact deformations on the adhesion of particles.* Journal of Colloid and interface science, 1975. **53**(2): p. 314-326.
54. Johnson, K., K. Kendall, and A. Roberts. *Surface energy and the contact of elastic solids*. in *Proceedings of the Royal Society of London A: Mathematical, Physical and Engineering Sciences*. 1971. The Royal Society.
55. Maugis, D., *Extension of the Johnson-Kendall-Roberts theory of the elastic contact of spheres to large contact radii.* Langmuir, 1995. **11**(2): p. 679-682.
56. Ting, T., *The contact stresses between a rigid indenter and a viscoelastic half-space.* Journal of Applied Mechanics, 1966. **33**(4): p. 845-854.
57. Sneddon, I.N., *The relation between load and penetration in the axisymmetric Boussinesq problem for a punch of arbitrary profile.* International journal of engineering science, 1965. **3**(1): p. 47-57.
58. Rico, F., et al., *Probing mechanical properties of living cells by atomic force microscopy with blunted pyramidal cantilever tips.* Physical Review E, 2005. **72**(2): p. 021914.
59. Akhremitchev, B.B. and G.C. Walker, *Finite sample thickness effects on elasticity determination using atomic force microscopy.* Langmuir, 1999. **15**(17): p. 5630-5634.
60. Tabor, D., *Surface forces and surface interactions*, in *Plenary and Invited Lectures*. 1977, Elsevier. p. 3-14.
61. Magonov, S.N. and D.H. Reneker, *Characterization of polymer surfaces with atomic force microscopy.* Annual Review of Materials Science, 1997. **27**(1): p. 175-222.

62. Liu, Y., et al., *Aggregation and morphology control enables multiple cases of high-efficiency polymer solar cells.* Nat Commun, 2014. **5**.
63. Wang, D., et al., *Characterization of morphology and mechanical properties of block copolymers using atomic force microscopy: Effects of processing conditions.* Polymer, 2012. **53**(9): p. 1960-1965.
64. Nguyen, H.K., S. Fujinami, and K. Nakajima, *Elastic modulus of ultrathin polymer films characterized by atomic force microscopy: The role of probe radius.* Polymer, 2016. **87**: p. 114-122.
65. Nizamoglu, S., et al., *Bioabsorbable polymer optical waveguides for deep-tissue photomedicine.* Nature Communications, 2016. **7**: p. 10374.
66. Calleja, M., et al., *Highly sensitive polymer-based cantilever-sensors for DNA detection.* Ultramicroscopy, 2005. **105**(1): p. 215-222.
67. Tamayo, J. and R. García, *Effects of elastic and inelastic interactions on phase contrast images in tapping-mode scanning force microscopy.* Applied Physics Letters, 1997. **71**(16): p. 2394-2396.
68. Melcher, J., et al., *Origins of phase contrast in the atomic force microscope in liquids.* Proceedings of the National Academy of Sciences, 2009. **106**(33): p. 13655-13660.
69. Chyasnavichyus, M., S.L. Young, and V.V. Tsukruk, *Recent advances in micromechanical characterization of polymer, biomaterial, and cell surfaces with atomic force microscopy.* Japanese Journal of Applied Physics, 2015. **54**(8S2): p. 08LA02.
70. James, P., et al., *Interpretation of contrast in tapping mode AFM and shear force microscopy. A study of nafion.* Langmuir, 2001. **17**(2): p. 349-360.
71. Cartagena-Rivera, A.X., et al., *Fast, multi-frequency, and quantitative nanomechanical mapping of live cells using the atomic force microscope.* Scientific reports, 2015. **5**: p. 11692.
72. Cheng, D., G. Yang, and Z. Xi, *Nonlinear systems possessing linear symmetry.* International Journal of Robust and Nonlinear Control, 2007. **17**(1): p. 51-81.
73. Garcia, R., et al., *Identification of nanoscale dissipation processes by dynamic atomic force microscopy.* Physical review letters, 2006. **97**(1): p. 016103.
74. Melcher, J., S. Hu, and A. Raman, *Invited Article: VEDA: A web-based virtual environment for dynamic atomic force microscopy.* Review of Scientific Instruments, 2008. **79**(6): p. 061301.
75. Haviland, D.B., et al., *Probing viscoelastic response of soft material surfaces at the nanoscale.* Soft matter, 2016. **12**(2): p. 619-624.
76. Solares, S.D., *A simple and efficient quasi 3-dimensional viscoelastic model and software for simulation of tapping-mode atomic force microscopy.* Beilstein journal of nanotechnology, 2015. **6**(1): p. 2233-2241.
77. Kiracofe, D., J. Melcher, and A. Raman, *Gaining insight into the physics of dynamic atomic force microscopy in complex environments using the VEDA simulator.* Review of Scientific Instruments, 2012. **83**(1): p. 013702.
78. Attard, P., *Measurement and interpretation of elastic and viscoelastic properties with the atomic force microscope.* Journal of Physics: Condensed Matter, 2007. **19**(47): p. 473201.
79. Attard, P., *Interaction and deformation of viscoelastic particles: Nonadhesive particles.* Physical Review E, 2001. **63**(6): p. 061604.
80. Attard, P., *Interaction and deformation of elastic bodies: origin of adhesion hysteresis.* The Journal of Physical Chemistry B, 2000. **104**(45): p. 10635-10641.

81. Attard, P. and J.L. Parker, *Deformation and adhesion of elastic bodies in contact.* Physical Review A, 1992. **46**(12): p. 7959.
82. Boussinesq, J., *Application des potentiels à l'étude de l'équilibre et du mouvement des solides élastiques: principalement au calcul des déformations et des pressions que produisent, dans ces solides, des efforts quelconques exercés sur une petite partie de leur surface ou de leur intérieur: mémoire suivi de notes étendues sur divers points de physique, mathematique et d'analyse*. Vol. 4. 1885: Gauthier-Villars.
83. Raghavan, D., et al., *Mapping polymer heterogeneity using atomic force microscopy phase imaging and nanoscale indentation.* Macromolecules, 2000. **33**(7): p. 2573-2583.
84. Tamayo, J. and R. Garcia, *Deformation, contact time, and phase contrast in tapping mode scanning force microscopy.* Langmuir, 1996. **12**(18): p. 4430-4435.
85. Winkler, R., et al., *Imaging material properties by resonant tapping-force microscopy: a model investigation.* Physical Review B, 1996. **54**(12): p. 8908.
86. Anczykowski, B., et al., *Basic properties of dynamic force spectroscopy with the scanning force microscope in experiment and simulation.* Ultramicroscopy, 1996. **66**(3): p. 251-259.
87. Rodrıguez, T.R. and R. García, *Tip motion in amplitude modulation (tapping-mode) atomic-force microscopy: Comparison between continuous and point-mass models.* Applied Physics Letters, 2002. **80**(9): p. 1646-1648.
88. Garcia, R., et al., *Identification of nanoscale dissipation processes by dynamic atomic force microscopy.* Physical review letters, 2006. **97**(1): p. 016103.
89. Anczykowski, B., et al., *How to measure energy dissipation in dynamic mode atomic force microscopy.* Applied Surface Science, 1999. **140**(3): p. 376-382.
90. Lozano, J.R. and R. Garcia, *Theory of phase spectroscopy in bimodal atomic force microscopy.* Physical Review B, 2009. **79**(1): p. 014110.
91. Melcher, J., S. Hu, and A. Raman, *Equivalent point-mass models of continuous atomic force microscope probes.* Applied Physics Letters, 2007. **91**(5): p. 053101.
92. Brinson, H.F. and L.C. Brinson, *Polymer engineering science and viscoelasticity*. 2008: Springer.
93. Pethica, J. and A. Sutton, *On the stability of a tip and flat at very small separations.* Journal of Vacuum Science & Technology A: Vacuum, Surfaces, and Films, 1988. **6**(4): p. 2490-2494.
94. Smith, J.R., et al., *Avalanche in adhesion.* Physical review letters, 1989. **63**(12): p. 1269.
95. Martínez, N.F. and R. García, *Measuring phase shifts and energy dissipation with amplitude modulation atomic force microscopy.* Nanotechnology, 2006. **17**(7): p. S167.
96. Israelachvili, J.N., *Intermolecular and surface forces: revised third edition*. 2011: Academic press.
97. Hurley, D., et al., *Measurement of Viscoelastic Loss Tangent with Contact Resonance Modes of Atomic Force Microscopy.* Macromolecules, 2013. **46**(23): p. 9396-9402.
98. Yablon, D.G., et al., *Quantitative Viscoelastic Mapping of Polyolefin Blends with Contact Resonance Atomic Force Microscopy.* Macromolecules, 2012. **45**(10): p. 4363-4370.
99. Keddie, J.L., R.A. Jones, and R.A. Cory, *Size-dependent depression of the glass transition temperature in polymer films.* EPL (Europhysics Letters), 1994. **27**(1): p. 59.
100. Zhang, Y.-F., et al., *Study on the viscoelastic properties of the epoxy surface by means of nanodynamic mechanical analysis.* Journal of Polymer Science Part B: Polymer Physics, 2008. **46**(3): p. 281-288.

101. Torres, J.M., C.M. Stafford, and B.D. Vogt, *Elastic Modulus of Amorphous Polymer Thin Films: Relationship to the Glass Transition Temperature.* ACS Nano, 2009. **3**(9): p. 2677-2685.
102. Belikov, S., et al., *Parametrization of atomic force microscopy tip shape models for quantitative nanomechanical measurements.* Journal of Vacuum Science & Technology B: Microelectronics and Nanometer Structures Processing, Measurement, and Phenomena, 2009. **27**(2): p. 984-992.
103. Giró-Paloma, J., et al., *Depth-sensing indentation applied to polymers: A comparison between standard methods of analysis in relation to the nature of the materials.* European polymer journal, 2013. **49**(12): p. 4047-4053.
104. Lakrout, H. and G. Meyers, *Contact mechanics of a viscoelastoplastic film bonded to a rigid substrate.* Proc. Annu. Meet. Adhes. Soc., 2010. **33st** p. 304-306
105. Lakrout, H., et al., *Quantitative AFM-based nanoindentation of poly(dimethylsiloxane) films* Proc. Annu. Meet. Adhes. Soc., 2008. **31st** p. 392-394
106. Wagner, R., et al., *Uncertainty quantification in nanomechanical measurements using the atomic force microscope.* Nanotechnology, 2011. **22**(45): p. 455703.
107. Lagakos, N., et al., *Frequency and temperature dependence of elastic moduli of polymers.* Journal of applied physics, 1986. **59**(12): p. 4017-4031.
108. Koblar, D. and M. Boltežar, *Evaluation of the Frequency-Dependent Young's Modulus and Damping Factor of Rubber from Experiment and Their Implementation in a Finite-Element Analysis.* Experimental Techniques, 2013.
109. Sahagún, E., et al., *Energy dissipation due to capillary interactions: hydrophobicity maps in force microscopy.* Physical review letters, 2007. **98**(17): p. 176106.
110. Zitzler, L., S. Herminghaus, and F. Mugele, *Capillary forces in tapping mode atomic force microscopy.* Physical Review B, 2002. **66**(15): p. 155436.
111. Cleveland, J., et al., *Energy dissipation in tapping-mode atomic force microscopy.* Applied Physics Letters, 1998. **72**(20): p. 2613-2615.
112. Lee, S., et al., *Nonlinear dynamic perspectives on dynamic force microscopy.* Ultramicroscopy, 2003. **97**(1-4): p. 185-198.
113. Garcia, R. and A. San Paulo, *Dynamics of a vibrating tip near or in intermittent contact with a surface.* Physical Review B, 2000. **61**(20): p. R13381.
114. Benaglia, S., C.A. Amo, and R. Garcia, *Fast, quantitative and high resolution mapping of viscoelastic properties with bimodal AFM.* Nanoscale, 2019. **11**(32): p. 15289-15297.
115. García, R., R. Magerle, and R. Perez, *Nanoscale compositional mapping with gentle forces.* Nature Materials, 2007. **6**: p. 405.
116. Forchheimer, D., R. Forchheimer, and D.B. Haviland, *Improving image contrast and material discrimination with nonlinear response in bimodal atomic force microscopy.* Nature communications, 2015. **6**: p. 6270.
117. Stark, R.W., N. Naujoks, and A. Stemmer, *Multifrequency electrostatic force microscopy in the repulsive regime.* Nanotechnology, 2007. **18**(6): p. 065502.
118. Santos, S., et al., *Multifrequency AFM: from origins to convergence.* Nanoscale, 2017. **9**(16): p. 5038-5043.
119. Oliver, W.C. and G.M. Pharr, *An improved technique for determining hardness and elastic modulus using load and displacement sensing indentation experiments.* Journal of materials research, 1992. **7**(6): p. 1564-1583.

120. McKay, M.D., R.J. Beckman, and W.J. Conover, *A comparison of three methods for selecting values of input variables in the analysis of output from a computer code.* Technometrics, 2000. **42**(1): p. 55-61.
121. Sarioglu, A.F., S. Magonov, and O. Solgaard, *Tapping-mode force spectroscopy using cantilevers with interferometric high-bandwidth force sensors.* Applied Physics Letters, 2012. **100**(5): p. 053109.
122. Santos, S., *Enhanced sensitivity and contrast with bimodal atomic force microscopy with small and ultra-small amplitudes in ambient conditions.* Applied Physics Letters, 2013. **103**(23): p. 231603.
123. Sader, J.E., *Frequency response of cantilever beams immersed in viscous fluids with applications to the atomic force microscope.* Journal of Applied Physics, 1998. **84**(1): p. 64-76.
124. Xu, X., M. Koslowski, and A. Raman, *Dynamics of surface-coupled microcantilevers in force modulation atomic force microscopy – magnetic vs. dither piezo excitation.* Journal of Applied Physics, 2012. **111**(5): p. 054303.
125. Basak, S. and A. Raman, *Dynamics of tapping mode atomic force microscopy in liquids: Theory and experiments.* Applied Physics Letters, 2007. **91**(6): p. 064107.
126. Sahin, O., et al., *Resonant harmonic response in tapping-mode atomic force microscopy.* Physical Review B, 2004. **69**(16): p. 165416.
127. Lai, C.-Y., et al., *Periodicity in bimodal atomic force microscopy.* Journal of Applied Physics, 2015. **118**(4): p. 044905.
128. Sader, J.E., J.W.M. Chon, and P. Mulvaney, *Calibration of rectangular atomic force microscope cantilevers.* Review of Scientific Instruments, 1999. **70**(10): p. 3967-3969.
129. Hutter, J.L. and J. Bechhoefer, *Calibration of atomic-force microscope tips.* Review of Scientific Instruments, 1993. **64**(7): p. 1868-1873.
130. Benaglia, S., et al., *Fast and high-resolution mapping of elastic properties of biomolecules and polymers with bimodal AFM.* Nature Protocols, 2018. **13**(12): p. 2890-2907.
131. Labuda, A., et al., *Calibration of higher eigenmodes of cantilevers.* Review of Scientific Instruments, 2016. **87**(7): p. 073705.
132. Meng, X., et al., *Broad modulus range nanomechanical mapping by magnetic-drive soft probes.* Nature Communications, 2017. **8**(1): p. 1944.
133. Landau, L.D., et al., *Theory of Elasticity, 3rd ed.* 1986: Elsevier Science.
134. Greenwood, J., *Adhesion of elastic spheres.* Proceedings of the Royal Society of London. Series A: Mathematical, Physical and Engineering Sciences, 1997. **453**(1961): p. 1277-1297.
135. Derjaguin, B.V., *Untersuchungen über die Reibung und Adhäsion, IV.* Kolloid-Zeitschrift, 1934. **69**(2): p. 155-164.
136. Alessandrini, A. and P. Facci, *AFM: a versatile tool in biophysics.* Measurement science and technology, 2005. **16**(6): p. R65.
137. Hugel, T. and M. Seitz, *The study of molecular interactions by AFM force spectroscopy.* Macromolecular rapid communications, 2001. **22**(13): p. 989-1016.
138. Janshoff, A., et al., *Force spectroscopy of molecular systems—single molecule spectroscopy of polymers and biomolecules.* Angewandte Chemie International Edition, 2000. **39**(18): p. 3212-3237.
139. Pham, J.T., et al., *From elasticity to capillarity in soft materials indentation.* Physical Review Materials, 2017. **1**(1): p. 015602.

140. Pittenger, B., N. Erina, and C. Su, *Quantitative mechanical property mapping at the nanoscale with Peak Force QNM.* Veeco Appl. Note A 128:1–12, 2010.
141. Chopinet, L., et al., *Imaging living cells surface and quantifying its properties at high resolution using AFM in QI™ mode.* Micron, 2013. **48**: p. 26-33.
142. Efremov, Y.M., et al., *Viscoelastic mapping of cells based on fast force volume and PeakForce Tapping.* Soft matter, 2019. **15**(27): p. 5455-5463.
143. Pittenger, B., N. Erina, and C. Su, *Quantitative mechanical property mapping at the nanoscale with PeakForce QNM.* Application Note Veeco Instruments Inc, 2010. **1**.
144. Sahin, O., et al., *An atomic force microscope tip designed to measure time-varying nanomechanical forces.* Nature nanotechnology, 2007. **2**(8): p. 507-514.
145. Kékicheff, P. and C. Contal, *Cationic-Surfactant-Coated Mica Surfaces below the Critical Micellar Concentration: 1. Patchy Structures As Revealed by Peak Force Tapping AFM Mode.* Langmuir, 2019. **35**(8): p. 3087-3107.
146. Amo, C.A. and R. Garcia, *Fundamental high-speed limits in single-molecule, single-cell, and nanoscale force spectroscopies.* ACS nano, 2016. **10**(7): p. 7117-7124.
147. Ramprasad, R., et al., *Machine learning in materials informatics: recent applications and prospects.* npj Computational Materials, 2017. **3**(1): p. 1-13.
148. Kim, C., G. Pilania, and R. Ramprasad, *From organized high-throughput data to phenomenological theory using machine learning: the example of dielectric breakdown.* Chemistry of Materials, 2016. **28**(5): p. 1304-1311.
149. Smola, A.J. and B. Schölkopf, *A tutorial on support vector regression.* Statistics and computing, 2004. **14**(3): p. 199-222.
150. Liaw, A. and M. Wiener, *Classification and regression by randomForest.* R news, 2002. **2**(3): p. 18-22.
151. Sarle, W.S., *Neural networks and statistical models.* 1994.
152. James, G., et al., *An introduction to statistical learning*. Vol. 112. 2013: Springer.
153. Kaiser, E., J.N. Kutz, and S.L. Brunton, *Sparse identification of nonlinear dynamics for model predictive control in the low-data limit.* Proceedings of the Royal Society A, 2018. **474**(2219): p. 20180335.
154. Yang, W., et al., *When machine learning meets multiscale modeling in chemical reactions.* The Journal of Chemical Physics, 2020. **153**(9): p. 094117.
155. Brunton, S.L., J.L. Proctor, and J.N. Kutz, *Discovering governing equations from data by sparse identification of nonlinear dynamical systems.* Proceedings of the national academy of sciences, 2016. **113**(15): p. 3932-3937.